NUCLEAR STRUCTURE STUDIES AT HIGH ANGULAR MOMENTUM IN MASS $\sim$ 100 REGION

By

Biswarup Das

PHYS05201304013

Saha Institute of Nuclear Physics, Kolkata

A thesis submitted to the
Board of Studies in Physical Sciences

In partial fulfillment of requirements

for the Degree of

DOCTOR OF PHILOSOPHY

of

HOMI BHABHA NATIONAL INSTITUTE

November, 2018

Homi Bhabha National Institute

Recommendations of the Viva Voce Board

As members of the Viva Voce Board, we recommend that the dissertation prepared by **Biswarup Das** entitled **"Nuclear structure studies at high angular momentum in mass ~ 100 region"** may be accepted as fulfilling the dissertation requirement for the Degree of Doctor of Philosophy.

Pradip Kr. Roy

Date : 26.11.2018

Chairman : Prof. Pradip Kumar Roy

Date : 26/11/2018

Guide : Prof. Sukalyan Chattopadhyay

Gautam Gangopadhyay

Date : 26.11.2018

Examiner : Prof. Gautam Gangopadhyay

Asimananda Goswami

Date : 26.11.2018

Member 1: Prof. Asimananda Goswami

Date : 26/11/2018

Member 2: Dr. Gopal Mukherjee

Final approval and acceptance of this dissertation is contingent upon the candidate's submission of the final copies of the dissertation to HBNI.

I hereby certify that I have read this dissertation prepared under my direction and recommend that it may be accepted as fulfilling the dissertation requirement.
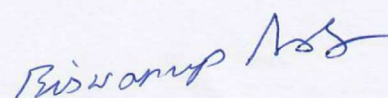
Date : 26/11/2018

Place : KOLKATA

26/11/2018

Guide : Prof. Sukalyan Chattopadhyay

STATEMENT BY AUTHOR

This dissertation has been submitted in partial fulfillment of requirements for an advanced degree at Homi Bhabha National Institute (HBNI) and is deposited in the library to be made available to borrowers under rules of the HBNI.

Brief quotations from this dissertation are allowable without special permission, provided that accurate acknowledgement of source is made. Requests for permission for extended quotation from or reproduction of this manuscript in whole or in part may be granted by the Competent Authority of HBNI when in his or her judgment the proposed use of the material is in the interests of scholarship. In all other instances, however, permission must be obtained from the author.

Biswarup Das

DECLARATION

I, hereby declare that the investigation presented in the thesis has been carried out by me. The work is original and the work has not been submitted earlier as a whole or in part for a degree/diploma at this or any other Institution or University.
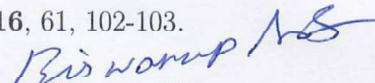
Biswarup Das

List of Publications arising from the thesis

Journal :

1. "The three proton hole structure in ^{106}Ag", **B. Das**, N. Rather, S. Chattopadhyay, S. Rajbanshi, A. Goswami, P. Datta, S. Roy, R. Palit, S. Pal, S. Saha, J. Sethi, S. Biswas, P. Singh, and H. C. Jain,
   Physical Review C , **2016**, 93, 064322.

2. "Novel evolution of the positive parity shears band in ^{106}Ag", **B. Das**, N. Rather, P. Datta, S. Chattopadhyay, S. Rajbanshi, A. Goswami, S. Roy, S. Pal, R. Palit, S. Saha, J. Sethi, S. Biswas, P. Singh, and H. C. Jain,
   Physical Review C, **2017**, 95, 051301(R).

3. "Coexistence of principal and tilted axis rotation in ^{110} Ag", **B. Das**, P. Datta, S. Chattopadhyay, S. Roy, R. Raut, R. K. Bhowmik, A. Goswami, H. C. Jain, R. Kumar, S. Muralithar, D. Negi, S. Pal, R. Palit, and R. P. Singh,
   Physical Review C, **2018**, 98, 014326.

Conferences :

1. "Staircase bands in ^{105,107,109}Ag: Fingerprint of interplay between Shears Mechanism and Collective Rotation", **B. Das**, Niyaz Rather, P. Datta, S. Chattopadhyay, A. Goswami, S. Rajbanshi, G. H. Bhat, J. A. Sheikh, S. Roy, R. Palit, S. Pal, S. Saha, J. Sethi, S. Biswas, P. Singh, and H. C. Jain,
   Proceedings of the DAE-BRNS Symp. on Nucl. Phys. **2015**, 60, 82-83.

2. "Continuous evolution from quasi particle excitation mode to collective excitation: study of +ve parity band in ^{106}Ag nucleus", **B. Das**, N. Rather, P. Datta, S. Chattopadhyay, S. Rajbanshi, A. Goswami, S. Roy, R. Palit, S. Pal, S. Saha, J. Sethi, S. Biswas, P. Singh, and H. C. Jain,
   Proceedings of the DAE-BRNS Symp. on Nucl. Phys. **2016**, 61, 102-103.

Biswarup Das

To
Dada

ACKNOWLEDGEMENTS

Contents

Contents

SYNOPSIS

Our world is essentially composed of finite fermionic systems i.e. the electron cloud of the atoms and the atomic nucleus. The electrons are the degrees of freedom for the electronic cloud while neutrons and protons play that role for the nucleus. However, this degree of freedom for a finite fermionic system may change depending on the energy scale. For example, at the relativistic energies, the degrees of freedom for nuclear matter becomes quarks and gluons. In the quest of studying finite fermionic systems, a wide variety of such systems have also been synthesized, e.g. droplets of ^{3}He atoms, quantum dots, electron traps, confined fermi gas clouds etc. They have opened up the exciting possibilities to study many-body quantum phenomena [1]. The finite fermionic systems are broadly classified in two categories, the self-bound systems and thoese bound by external force, e.g. ^{3}He droplet is a self bound system but a quantum dot is bound by an external force field.

The most intriguing self bound finite fermionic system is provided by the nature, which is the atomic nucleus. At the Indian accelerator centers the nucleus is probed at MeV scale which restricts the degree of freedom to nucleons. In a nucleus, the binding force between the nucleons originated due to the strong interaction. This force is attractive in nature when the mutual distance is $\gtrsim$fm, but becomes repulsive at shorter distances. The repulsive nature implies the asymptotic freedom and leads to the formation of Quark Gluon Plasma (QGP) at energy densities of 1 GeV/fm^3. This energy domain is being investigated at the Large Hadron Collider at CERN. However, at lower energies this force is purely attractive and the direct consequence is the pairing of protons and neutrons in time reversed orbits with a pair gap energy of about 1 MeV. This large pair gap allows a description of the

nuclear many body problem. The earliest success was the 'shell model' [2], where only the valance nucleons are assumed to move in a mean-field which is modeled as a harmonic oscillator with spin-orbit coupling term. In this connection it may be noted that the shell effect is a characteristic feature of finite fermionic systems and is also observed in the electron clouds of atoms, metal clusters and quantum dots.

Another intriguing feature of finite fermionic systems is the existence of collectivity. An ultra-cold cloud of $\sim 4 \times 10^5$ ^{6}Li atoms shows collective angular oscillations about the principal axis of the elliptic trap when the trap is suddenly rotated by $\sim 5°$ [3]. Another evidence of collectivity is the strong dipole and quadrupole resonances observed in ultra small two dimensional systems of ~ 20 electrons per quantum dot [4]. The collective excitation in a spherical nucleus leads to the surface vibrations while a deformed nucleus exhibit rotational spectrum which obey the E(I) = I(I+1) behaviour, where I and E are the total angular momentum and the energy, respectively. The vibration of nucleus leads to the generation of few $\hbar$ units of angular momentum while collective rotational spectra can extend up to 50$\hbar$. However, unlike the other finite systems, a change in the configuration of only one or two nucleons can have a significant effect on collective spectra of the whole nucleus [5]. This property makes the study of the generation of angular momentum in atomic nucleus an interesting and a diverse field of research. In the present thesis, the different angular momentum generation mechanisms in nuclei of A∼100 region have been explored. The various available mechanisms will be discussed in Chapter 2 and the different experimental techniques used to study these mechanisms will be presented in the Chapter 3 of this thesis.

The interest in the A∼100 region is due to the fact that proton holes occupy the

$g_{9/2}$ orbital followed by a large shell gap (p = 50), which restricts the phase space for protons. On the other hand, few unpaired neutrons are distributed among the positive parity $g_{7/2}/d_{5/2}$ orbitals or negative parity $h_{11/2}$ orbital. By virtue of the parity conservation rule of strong interaction, the $h_{11/2}$ orbital never overlaps with the other two and thus, the single particle configurations can be uniquely determined for the positive and the negative parity states.

In the present thesis, the high-spin states of ^{106}Ag was populated through the fusion-evaporation reaction ^{96}Zr(^{14}N,4n) using a 68 MeV ^{14}N beam from the Pelletron-LINAC facility at TIFR, Mumbai. An enriched ^{96}Zr of thickness 1 mg/cm^2 with 9 mg/cm^2 thick ^{206}Pb backing was used as the target. In the present work, the origin of the non-yrast positive and the negative parity bands has been studied. The negative parity non-yrast band was reported in recent times by Lieder *et. al.* [6] and a single particle configuration of $\pi g_{9/2}^{-1} \otimes \nu[h_{11/2}^1(g_{7/2}, d_{5/2})^2]$ was proposed by them. In the present thesis magnetic dipole (B(M1)) and electric quadrupole (B(E2)) transition rates were deduced using the measured level lifetimes. The level lifetime measurement was carried out using 'Doppler shift attenuation method'. A falling trend in both the B(M1) and B(E2) values was observed which could not be reproduced by the configuration proposed by Lieder *et. al.* [7].

The falling trend in both the transition rates seems to indicate that this negative parity band originates due to the shears mechanism [8]. However, this band extends up to I= 21$\hbar$ which is 6$\hbar$ higher than the maximum angular momentum that can be generated by the shears structure. This contribution has been assumed to arise due to the core rotation and a model of *Shears with Principal Axis Cranking* (SPAC) [9] has been employed. In order to reproduce the measured transition rates, the

numerical calculations indicated a single particle configuration of $\pi g_{9/2}^{-3} \otimes \nu h_{11/2}^{1}$ upto I=17$\hbar$ and $\pi g_{9/2}^{-3} \otimes \nu[h_{11/2}^{1}(d_{5/2}/g_{7/2})^{2}]$ configuration afterwards. It may be noted that this is the first report of a three proton hole structure in Ag isotopes [7]. The details of the data analysis and the numerical calculations will be described in Chapter 4.

The non-yrast positive parity band in ^{106}Ag is built on $\pi g_{9/2}^{-1} \otimes \nu[h_{11/2}^{2}(d_{5/2}/g_{7/2})]$ single particle configuration. In the present work, this band has been extended up to $I = 25\hbar$ and the sub-picosecond level lifetime measurement was carried out using DSAM technique. The calculated transition rates (B(M1) and B(E2)) showed a falling trend up to $I = 21\hbar$ and remain nearly constant afterwards. This is a unique phenomena and has been observed for the first time [10, 11]. While the falling trend of the transition rates is a signature of shears band, the near constant transition rates is a signature of principal axis rotation. In order to investigate the theoretical origin, the model of SPAC was employed. It was found that the states up to 21$\hbar$ originates due to an interplay of shears mechanism and core rotation while the higher angular momentum states originate due to non-collective rotation [10]. The Chapter 4 of this thesis will cover this work in detail.

In a separate experiment the high spin levels of ^{110}Ag were populated using $^{96}Zr(^{18}O, p3n)$ reaction. It may be noted that ^{110}Ag is the heaviest Ag isotope which had been populated through fusion evaporation reaction [12]. Previously, only the yrast band was established which was found to originate purely due to collective rotation. This observation is unique for Ag isotopes and thus it was interesting to explore the origin of the non-yrast states.

During the course of this thesis the non-yrast positive and negative parity

states have been established for the first time. The spins and parities of the newly placed energy levels were established by measuring the DCO and the PDCO ratios of the decaying γ-rays. Level-lifetime measurement of the positive parity band was carried out using the DSAM technique [13]. The complete γ-spectroscopy of ^{110}Ag and the numerical calculations employed to reproduce the experimental results will be presented in the Chapter 5 of this thesis.

The yrast positive parity bands in odd mass Ag isotopes (^{105,107,109}Ag) originate due to one proton hole in the high-Ω $g_{9/2}$ orbital and two aligned neutrons in the low-Ω $h_{11/2}$ orbital. This single particle configuration indicates that these bands may originate due to shears mechanism. In the previous reports on ^{107,109}Ag [14, 15], the measured transition rates show a falling trend but the level energies do not increase smoothly with increasing spin. In reality, the energy difference (E(I) -E(I-1)) shows a staircase like structure when plotted as a function of spin [16].

In the present thesis work, the level lifetime measurements for the yrast levels have been carried out for ^{105}Ag which was populated through the ^{96}Zr(^{14}N,5n) reaction. The measured transition rates also show a falling trend with increasing spin as was observed in ^{109}Ag [14]. In order to describe the observed features of these 'staircase' bands, the SPAC model has been modified to incorporate a decoupling term for the core rotation. These calculations seems to indicate that the 'staircase' band may originate due to shears mechanism in a triaxial nucleus. The complete systematic study will be discussed in the Chapter 6 of this thesis.

The summary of the present thesis work will be discussed in Chapter 7 of this thesis.

List of Figures

List of Tables

1

Introduction

The elementary particles are the basic constituents of our universe. They are primarily catagorised into fermions or bosons depending on their half-integer or integer spins, respectively. The elementary fermions tend to group together and form bound states and by the repetitive arrangement of which, the finite dimensionality of our world is realised. In a bound state, the fermions are confined by a potential which arises due to the exchange of mediator bosons between them. The experimental investigations of these fermionic bound states are carried out by using probes of sufficient energy to penetrate the confining potential. With different probe energies, different groupings can be observed with changed fermionic degrees of freedom and the exchange bosons also changes accordingly. Thus, depending on the energy scale of observation, different physical mechanisms come into play to govern the system behavior. In the atomic nucleus, which is our system of interest, at least MeV energy probe is needed, as the confining potential is of this order. In this energy regime, the nucleons (neutrons and protons) act as the degrees of freedom where the confinement potential is generated by the exchange of π-mesons

between them. On the other hand, when probed at a larger energy density, i.e. ≥ 1 MeV/fm^3, the quarks acts as the fermionic degree of freedom with the gluons as the exchange bosons.

The finite fermionic systems have been of interest of study to physicists for a long time because of the symmetries and complexities associated with it. Although the motion of the fermions can be successfully described in the framework of quantum mechanics, an exact solution can be obtained only for few of them. In contrast, the use of 'quantum statistical mechanics' helps us to understand the behaviour of systems composed of large ($\geq 10^4$) number of fermions. The theoretical domain for finite number is still out of reach. Yet, many important properties of finite fermionic systems have been determined from the experimental observations. For these studies, droplets of ^{3}He atoms, quantum dots etc. have been synthesized artificially [1]. However, nature has provided us with the atomic nucleus which is a unique finite fermionic system where the nucleon number varies from one to a few hundred. Moreover, the confining potential of the nucleons arises due to the strong interaction, which is not fully understood. Thus, the nucleus is the most studied finite fermionic system at its ground state as well as at its excited states. The elementary processes like elastic, inelastic and transfer reactions and nuclear fission have been explored in great detail. These observations have led to the development of a number of semi-classical models. On the other hand, ab initio models based on effective interactions like, 'no core shell model' or 'density functional theory' still have limited applicability. Thus, the structure study of the nucleus relies mostly on experimental observations. These observations indicate the existence of a number of symmetries in atomic nuclei.

The existence of symmetries is intrinsic to nature and every symmetry related

to an observable leads to a conservation law. For example the homogeneity of space leads to the momentum conservation law, which is also the Newton's first law of motion. In a similar way, the conserved quantity accounting for the isotropy of space is the angular momentum which leads to one of the Kepler's law governing the motion of planets. The total energy of a system is conserved if the system remains invariant under time translation. Using these symmetries, Niels Bohr proposed the energy and angular momentum quantisation rules to describe motion of the electrons inside an atom. On the other hand, the permutation symmetry helps to group the fundamental particles into Fermions or Bosons. The standard model of physics is built on the CPT symmetry consideration. Thus, the fundamental laws of nature invoke different symmetries. In this chapter, I shall qualitatively discuss how the symmetry principles help us to model the different aspects of the nuclear structure.

The first symmetry observed in a nucleus, is the charge symmetry of the nuclear force, i.e. the strong attraction between proton-proton, neutron-neutron and proton-neutron is nearly same. In addition, the near mass degeneracy of the proton and the neutron led us to define an observable called Isospin (I^s). The I^s takes a value of 1/2 and is rotationally invariant in the isopin space [17]. In this space, the projections $I_z^s = \pm\ 1/2$ refer to the proton and the neutron, respectively. For a two nucleon system, the resultant isospin takes the form

$$|I^s = 1\rangle = \begin{cases} |I_z^s = 1\rangle = pp \\[2mm] |I_z^s = 0\rangle = \sqrt{\tfrac{1}{2}}[pn + np] \\[2mm] |I_z^s = -1\rangle = nn \end{cases} \tag{1.1}$$

17

Chapter 1. Introduction

$$|I^s = 0\rangle = \sqrt{\frac{1}{2}}[pn - np]$$

The charge invariance of the nuclear force is implied only for the $|I^s = 1\rangle$ state, as the $p-p$, $p-n$ and $n-n$ systems are all equally probable. However, the first bound state found in the deuteron nucleus is a $p-n$ bound state, which automatically suggest that the deuteron nucleus is in a isospin $|I^s = 0\rangle$ state. Thus, the charge symmetry is broken here. This broken symmetry led to the fact that a $p-n$ state is more strongly bound if in the $|I^s = 0\rangle$ state rather than the $|I^s = 1\rangle$ state.

Secondly, the symmetry of the nuclear shape has a direct consequence on the motion of the nucleons inside a nucleus. For a spherical shape, the motion of the nucleons can be successfully described within the framework of 'independent particle shell model' [18]. The term independent stands for the exclusion of all mutual interactions between the nucleons. In this model, the potential in which the independent nucleons move is assumed to be a spherically symmetric harmonic oscillator potential of the form $\frac{m}{2}\omega^2(r^2 - R_0^2)$, where R_0 is the nuclear radius and ω is the oscillator frequency. Under these assumptions, the energy of the nucleon states are given by

$$E_{N,l} = [2(N - 1) + l]\hbar\omega \tag{1.2}$$

where, N is the principle quantum number and l is the orbital angular momentum. By the virtue of the spherical symmetry of the potential, the orbital angular momentum becomes a conserved quantity and the energy levels are characterized by the orbital angular momentum quantum number, l. A $(2l + 1)$ fold degeneracy is also evident from the azimuthual symmetry [19]. These $(2l+1)$ magnetic substates of l are filled by 4 nucleons, subjected to 2-fold isospin degeneracy and 2-fold spin degeneracy. In this way, the calculated energy levels could reproduce the magic

numbers up to n/p = 20 but fails for higher masses. This 2-fold spin degeneracy can further be lifted by taking into account the spin-orbit interaction of the type $\vec{l}.\vec{s}$. Under this interaction, the alignment of $\vec{l}$ and $\vec{s}$ are no longer independent, but they revolve around the resultant vector $\vec{j}(= \vec{l} + \vec{s})$. The single particle angular momentum, $\vec{j}$, thus becomes a good quantum number and the nuclear states gets characterized by $[E, j]$. However, the $(2j + 1)$ substates of $\vec{j}$ still remains degenerate due to the azimuthual symmetry. The spin-orbit interaction reshuffles the nuclear energy levels in a major way and the magic numbers up to p = 82 and n = 126 could be reproduced. Thus, the 'shell model' with spin-orbit interaction, gives a good description of the spherical nuclei.

In the next step of generalisation, the $(2j + 1)$ fold degeneracy can be lifted if the spherical symmetry of the nucleus is lost. This is dictated by the observation of the large quadrupole moments in the transitional nuclei across the periodic table [20]. The electric quadrupole moment in these nuclei arises from a non spherical distribution of charged protons. The idea of elongated nucleus was first proposed by Bohr and Wheeler [21] to describe the process of fission. However, the shape was only considered to exist in the intermediate stages of fission and was transient in nature . A stable deformation on the other hand, may exist in nuclei further from shell closure region [22]. The nonspherical field generated by the valance nucleons can be held responsible to distort the spherical core into a deformed shape. This shape driving effect is different for the proton and the neutron orbits, and an 'effective charge' [23] can be assigned to the protons and the neutrons, separately.

For an axially deformed shape, the angular momentum is no longer a good quantum number, due to the space anisotropy. However, the projection of angular momentum along the symmetry axis remains a good quantum number. This pro-

jection is denoted by Ω, which takes $(2j+1)$ values for the angular momentum, j. Among $(2j+1)$ states, the $\pm\Omega$ states are degenerate due to the reflection symmetry of the nucleus [20]. Thus, the two nucleons of same I_z^s fill these $\pm\Omega$ orbits to form a time reversed pair. For a prolate nucleus, the lowest Ω orbital has the maximum wave function overlap with the core and hence lowest in energy, whereas for an oblate nucleus the case is reversed.

The axial symmetry can further be lifted in the presence of two opposite shape driving orbitals, which leads to a triaxial shape of the nuclear core. In this case, Ω will not be a good quantum number. However, the π-rotational invariance leads to a new quantum number called 'signature' [24]. In addition, the single particle energy levels conserve its parity by the virtue of the strong interaction and it remains a good quantum number.

In the preceding discussions, we have seen how different symmetries govern the behaviour of the nucleus in its ground state. An excited nucleus, however, acts differently and new symmetries may also appear accordingly, as the dynamical state of the nucleus changes under excitation. The experimental conditions can be chosen to impose specific dynamical properties for a nucleus, such as rotation and vibration. We shall confine our discussion on the rotational excitation of the nucleus.

A spherical nucleus cannot rotate, as all the possible orientations results in the same configuration. On the other hand, the space isotropy is broken in a deformed nucleus, and as a result it can rotate. The rotational modes were first identified with the stable quadrupole deformed shape. A cylindrical symmetric shape is responsible to sustain the quadrupole deformation and the rotational excitation becomes responsible for the generation of high angular momentum.

The Coulomb excitation and the fusion evaporation reactions are mostly used to excite a nucleus to high angular momentum. The stable nuclear isotopes are studied through the process of Coulomb excitation. However, it is also important to study the excitation modes in nuclear isotopes away from the β stability line to increase the domain of research. The fusion evaporation reactions using heavy ion beams are suitable for this purpose.

As the nucleus is a quantum system, the observable associated with rotation is the angular momentum. During the process of excitation, either the energy is transferred to few nucleons, or the energy is shared by all the nucleons. The latter case is known as the collective mode of excitation. These two excitation modes are not entirely independent but competes with each other to generate the angular momentum. The spin, parity, energy and transition rates of the high spin levels can be obtained from the experimental data. The experimental observations are then compared with a suitable semi-classical model to obtain the nuclear structure information from the rotational spectra. A short description of these models has been presented in the next chapter.

An even-even axially deformed nucleus is the simplest system to observe the collective rotation as the independent nucleon excitations do not compete with the collective motion [22]. The rotation about the symmetry axis is forbidden by the same argument as why a spherical nuclei cannot rotate. On the other hand, if the nucleus is rotated perpendicular to the symmetry axis, the axial deformation ensures that only the quadrupole modes are excited. Thus, the rotational energy levels in these nuclei decay via a sequence of $E2$ transitions, where the level energy follows a $E(I) = \frac{\hbar^2}{2\mathcal{J}}I(I+1)$ rule for a nucleus with moment of inertia, $\mathcal{J}$. An additional restriction to the rotational degree of freedom arises due to the π-rotational

symmetry of the axial shape. The rotational bands are therefore, characterised by the eigen values of π rotation operator $(R_2(\pi))$, i.e. $r = \pm 1$, and a band consists only odd or even values of spin [23]. So the rotational spectrum, takes the form

$$I = \begin{cases} 0, \ 2, \ 4, ... \ r = +1 \\[1em] 1, \ 3, \ 5, ... \ r = -1 \end{cases} \tag{1.3}$$

For all even-even nuclei, the ground state spin is zero and thus, the first sequence of Eq. 1.3 is observed for the ground state band. The odd-even and the odd-odd nuclei on the other hand, exhibit a more complex ground state bands. The existence of the strong pairing force allows us to superimpose the single particle motion on the collective rotation of the core. If the particle-rotor coupling is strong, the particle motion follows the motion of the core adiabetically and the rotational band develops on the ground state spin K, which is the particle spin projection along the symmetry axis. The presence of the unpaired nucleon orbit also ensures a non-zero current distribution, hence the rotational band consists of $M1$ transitions, i.e.

$$I = K, \ K + 1, \ K + 2, ... \tag{1.4}$$

In addition, the cross-over $E2$ transitions are present due to the quadrupole deformation of the rotating core. The π rotational symmetry of the particle orbit is characterised by the 'signature quantum number' , which takes the values $\sigma = (-1)^{I+K}$ [23]. The $M1$ transitions connect the two signature bands, while the cross-over $E2$ transitions connect the same signature levels. A smooth increase of $M1$ transitions energies with increasing spin is observed. However, a different scenario emerges when an unpaired nucleon occupies the $\Omega = \frac{1}{2}$ orbital. In this

case, the band shows staggering in $M1$ transition energies and the effect is known as the 'signature staggering' [25].

Apart from the strong coupling limit, a somewhat different rotational spectra arise when the particle is decoupled from the core. A decoupled nucleon orbit aligns its spin, $\vec{j}$, along the rotation axis. The $M1$ transitions are not present as the current distribution in the aligned orbit is symmetric with respect to the rotation and the rotational spectrum becomes [26]

$$I = j, \ j + 2, \ j + 4, ... \tag{1.5}$$

The same situation can also be observed in even-even nuclei when two paired nucleons from the time-reversed orbits get aligned due to the Coriolis force. In this case, crossing between the ground state and the two particles aligned band is observed and the phenomenon is known as the backbending [27].

In an axially deformed nucleus, the rotational degrees of freedom are small as the rotation is possible only in the direction perpendicular to the symmetry axis. On the other hand, for a triaxial shape the space isotropy is broken due to rotation with respect to all the three principal axes. Although, the nucleus prefers to rotate about the axis with maximum moment of inertia, the presence of the rotational contributions from the other two axes drive the rotation axis off the principle plane. A fairly high spin states can be generated from this interplay and the mode of rotation is known as the 'wobbling motion' [28]. In addition, the phenomena of 'anomalous signature splitting', 'signature inversion' etc. are observed in the rotational spectrum of an odd-odd triaxial nucleus [28]. The presence of a particle-hole configuration in a triaxial rotor may give rise to a geometry which breaks the chiral symmetry of the system. The rotation of such systems generate

'chiral partner bands' [29]. The field of spin-chirality is currently an active field of research.

The observation of rotational band structure is generally linked to the deformed nuclei and thus, its presence in the near spherical Pb isotopes [30] was a surprise. The phenomena of 'shears mechanism' [31] was proposed to generate the high spin states in these nuclei. The shears mechanism is observed in nuclei where high-Ω proton holes exist along with neutrons in low-Ω orbitals or vice-versa. The spins of the particles and the holes align perpendicularly at the band head and resemble the blades of a shear. The higher spin states are then generated by a simultaneous closing of these two shear blades. The repulsive particle-hole interaction ensures an increase in energy with spin. The orbital currents give rise to a magnetic moment ($\mu_\perp$) perpendicular to the total spin which enhances the magnetic dipole transition rates ($B(M1)$). This moment rotates about the spin direction, hence the name 'magnetic rotation'. Moreover, the magnitude of $\mu_\perp$ decreases with the closing of the shears blades, as a result $B(M1)$ decreases with increasing spin. For the near spherical Pb isotopes, the cross-over $E2$ transitions are either absent or weakly present in these bands. However, an increase in $E2$ intensity is evident for the shears bands observed in transitional nuclei. The $E2$ transition strength i.e. the $B(E2)$ values, also decreases with increasing spin for shears bands [32]. So, in these nuclei the high spin states are generated by an interplay between the shears mechanism and the core rotation [33]. The existence of shears structure also opens up the possibility of a double shears structure in nuclei, which have a pair of holes in time reversed orbits. The high spin states are then generated by closing the two shears simultaneously. For this geometry the magnetic moment becomes zero and thus, only a pure $E2$ band structure is observed. The mechanism is commonly

known as the 'antimagnetic rotation' [34] and the electric quadrupole transition rates show a falling trend with increasing spin.

The path a nucleus follows to achieve high spin states is revealed in its footsteps. Thus, the spectroscopic study of the high-spin states reveals the mechanism for the generation of high angular momentum. In this context, I have studied the Ag isotopes of A $\sim$ 100 region. During the course of this thesis work, I have :

$i\rangle$ used a model which helps us to understand the high spin states generated from the interplay between the shears mode of excitation and the core rotation in the nuclei of A $\sim$ 100 region,

$ii\rangle$ established a three proton hole structure for the first time in ^{106}Ag isotope [7],

$iii\rangle$ found a novel explanation for the generation of higher spin states after the complete closure of a shears structure in the positive parity band of ^{106}Ag [10],

$iv\rangle$ reported the positive parity levels in ^{110}Ag for the first time and established that the structure of this band arises due to the shears mechanism [13],

$v\rangle$ identified four quasiparticle partner bands for the first time in ^{110}Ag - these bands may originate due to the spin chirality,

$vi\rangle$ explained the 'staircase' band found in the yrast cascades of $^{105,\ 107,\ 109}$Ag isotopes [16].

The γ-spectroscopic studies are carried out to explore the high spin structures of ^{106}Ag, ^{110}Ag and ^{105}Ag nuclei and will be described in detail in the chapters 4, 5 and 6 of this thesis.

2

Structure of the nucleus and its high spin behaviour

2.1 Introduction

The nucleus is a finite fermionic bound state where the binding energy is provided by the strong interaction between all the nucleons. Thus, an ab initio model for a nucleus is difficult to develop. However, different mean field or semi-classical calculations can be carried out to describe the observed properties of an atomic nucleus. In this chapter, I shall briefly discuss some of the models which are routinely used to describe the high spin behaviour of different nuclei across the periodic table.

2.2 The mean field models

The two-body interaction is the most dominant component of the nuclear force which bind the protons and neutrons inside the nucleus. This two body interaction is strongest at the inter nucleon distance of ~ 0.4 fm while, the Pauli exclusion principle restricts the close packing of nucleons and on the average nucleon mean free path is ~ 1.4 fm [24]. This opens up the possibility to consider the motion of the nucleons in a mean-field created by all the other nucleons inside a nucleus.

2.2.1 Spherical mean field : Shell model

For a spherical nucleus, the choice of mean-field potential is based on three facts [24] :

1. The attractive force on a nucleon close to the center of the nucleus is isotropic, thus the net force on it is zero, i.e.

$$\left(\frac{\partial V(r)}{\partial r}\right)_{r=0} = 0$$

2. The short range of the strong interaction ensures that the nuclear force vanishes outside the nuclear surface

$$V(r) \simeq 0, \ r > R_0$$

3. The binding force increases from the surface towards the center of the nucleus

$$\left(\frac{\partial V(r)}{\partial r}\right)_{r<R_0} > 0$$

A close agreement of these conditions could be found by approximating the mean field as the $Woods - Saxon$ potential:

$$V^{W.S.} = -V_0 \left[1 + exp\left(\frac{r - R_0}{a} \right) \right]^{-1}.$$ (2.1)

With this potential, solving the Schroedinger equation becomes exceedingly dif-
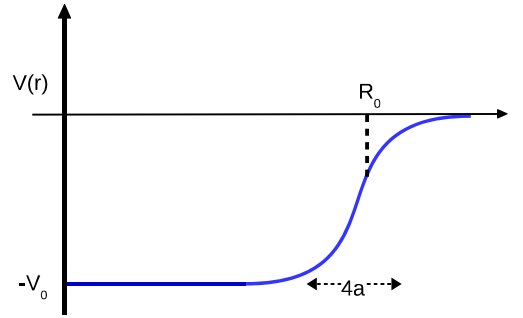
Figure 2.1: The shape of the Woods-Saxon potential, where, $R_0 = r_0 A^{1/3}$, $V_0 \simeq 50$ MeV, $a \simeq 0.5$ fm, $r_0 \simeq 1.2$ fm [24].

ficult to obtain a closed form of the eigenfunctions. A simplification can be done by approximating this potential with a spherically symmetric harmonic oscillator potential of the form

$$\begin{aligned} V(r) &= -V_0 \left[1 - \left(\frac{r}{R_0} \right)^2 \right] \\ &= \frac{m}{2} \omega_0^2 (r^2 - R_0^2) \end{aligned}.$$ (2.2)

This gives the equidistant discrete levels of energy

$$\epsilon_N = \hbar \omega_0 (N + 3/2) - V_0.$$

with $N = 2(n-1) + l$, where $n = 0,\ 1,\ 2,...$ and $l = 0,\ 1,\ 2,..,\ n-1$.
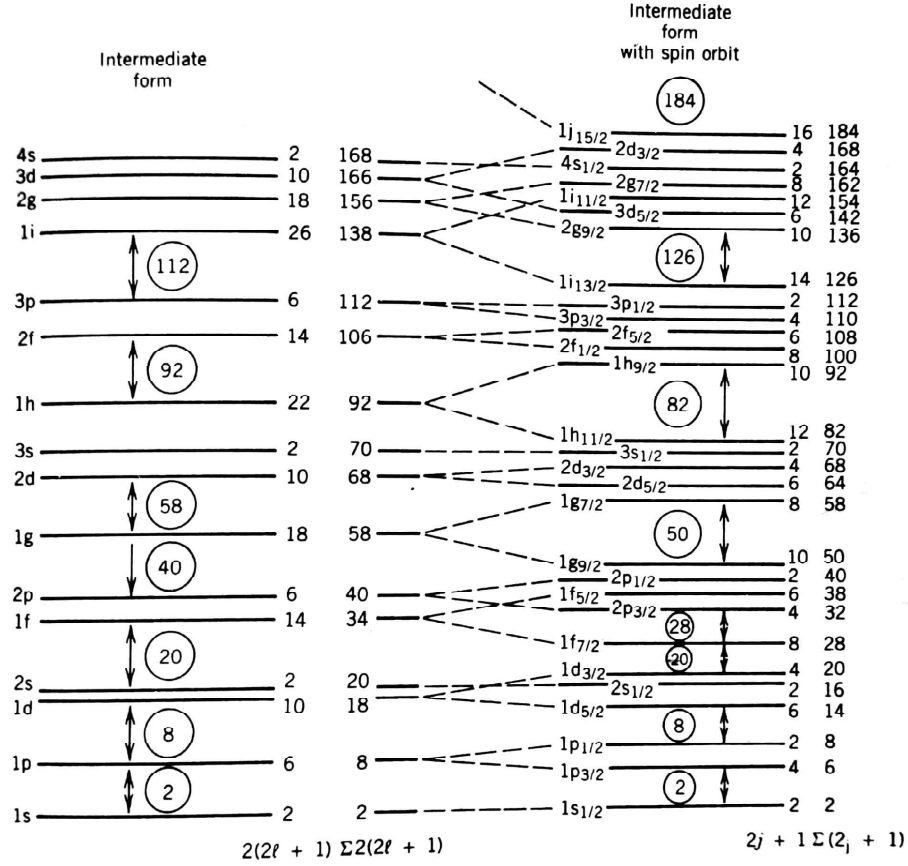
Figure 2.2: The shell model energy levels of a spherical nucleus. The levels with and without the spin-orbit coupling are shown in the left side and the right side of the figures, respectively. Figure taken from Ref. [20].

Every oscillator shell is defined by the oscillator quantum number, N, and in a shell every orbit is characterised by the 'orbital angular momentum quantum number', l, which is $(2l+1)$ fold degenerate. Moreover, an extra 2-fold degeneracy arises from the two projections of the 'spin quantum number', s. However, the nuclear levels arising this way were inconsistent with the experimental observations of the 'magic numbers'.

This inconsistency is removed by the inclusion of a spin-orbit coupling term of the form $-f(r)\vec{l}.\vec{s}$, as a perturbation. With this, the total angular momentum, $\vec{j}(= \vec{l} + \vec{s})$, becomes a good quantum number and the $(2j + 1)$ substates of j becomes degenerate. A schematic representation of the nuclear levels calculated in this method is shown in Fig. 2.2. The protons and the neutrons fill up these levels independently according to their energies.

The spherical shell model is quite successful in describing nuclear properties near the shell closure region. However, for the nuclei around the mid-shell region, the spherical shell-model fails. The properties like existence of rotational bands, large quadrupole moments, enhanced $B(E2)$ rates exhibited by these nuclei suggest a quadrupole deformed density distribution for the nucleons.

2.2.2   Deformed mean field : Nilsson model

The range of the nuclear force (~ 1 fm) is smaller compared to the nuclear diameter. Thus, the shape of the confining potential can be assumed to be the same as the density distribution of the nucleons [24]. For a defomed shape, the $Woods-Saxon$ potential takes the form

$$V^{W.S.}(r, \theta, \phi) = -V_0\left[1 + exp\left(\frac{r - R(\theta, \phi)}{a(\theta, \phi)}\right)\right]^{-1} \tag{2.3}$$

where,

$$R(\theta, \phi) = R_{av}[1 + \beta Y_{20}(\theta, \phi)] \tag{2.4}$$

for an axially symmetric deformation and the deviation from sphericity is measured by the deformation parameter, $\beta\left(= \frac{4}{3}\sqrt{\frac{\pi}{5}}\frac{\Delta R}{R_{av}}\right)$. In the harmonic oscillator approximation, the potential can be written as

$$V = \frac{m}{2}(\omega_x^2 + \omega_y^2 + \omega_z^2) \qquad (2.5)$$

For a quadrupole deformed shape with symmetry axis z, the oscillator frequencies are redefined as

$$\omega_\perp^2 = \omega_x^2 = \omega_y^2 = \omega_0^2(1 + \frac{2}{3}\delta)$$
$$\omega_z^2 = \omega_0^2(1 - \frac{4}{3}\delta) \qquad (2.6)$$

where, δ is related to the deformation parameter $\beta(= 1.057\delta)$. This gives the Nilsson Hamiltonian for a deformed nucleus

$$H = -\frac{\hbar^2}{2m}\Delta + \frac{m}{2}\omega_0^2 r^2 - m\omega_0^2 r^2 \delta \frac{4}{3}\sqrt{\frac{\pi}{5}}Y_{20}(\theta, \phi) + C\vec{l}.\vec{s} + Dl^2 \qquad (2.7)$$

where, C and D represents the strengths of the spin-orbit force and the centrifugal force respectively. The energy of the Nilsson orbits are obtained by solving the above equation. These orbits are labeled as

$$\Omega^\pi[Nn_zm_l] \qquad (2.8)$$

where, Ω is the spin projection along symmetry axis, π is the parity, N is the principle quantum number denoting a major shell, n_z is the number of nodes (along z direction) in the wave function and m_l is the component of the orbital angular momentum in the z direction.

Without a rigorous mathematics we can understand various properties of the Nilsson orbits by invoking symmetries of the deformed shape. A comparison with the spherical shell model simplifies the discussion. First of all, the total angular
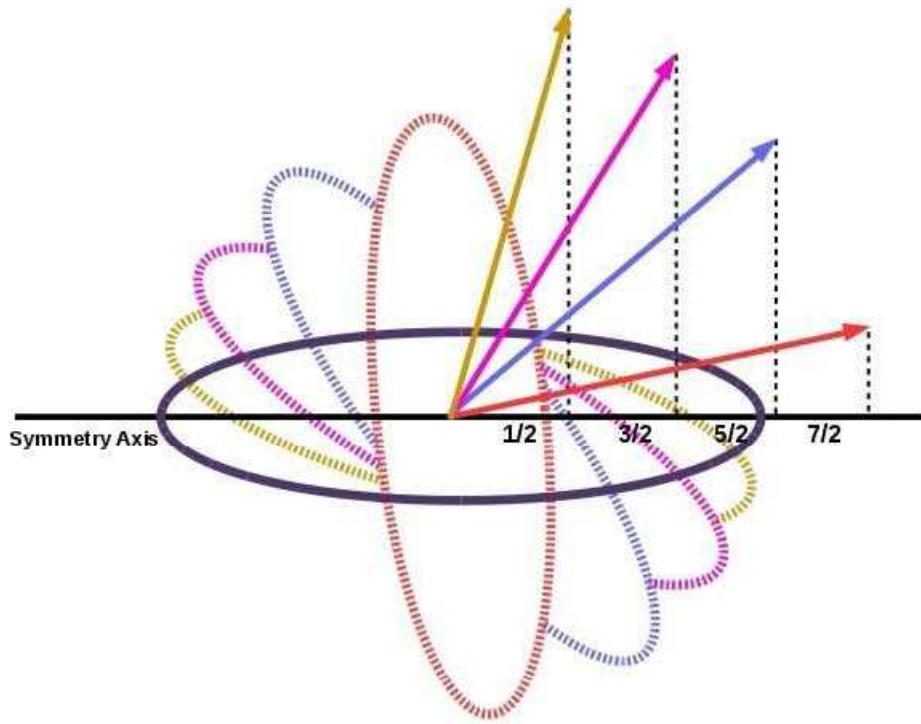
Figure 2.3: The splitting of $j = 7/2$ in four Ω orbitals for a prolate nucleus.

momentum, j, was a constant of motion in the spherical shell model and the orbits were $(2j+1)$ fold degenerate. The loss of rotational symmetry for a deformed shape breaks this degeneracy. However, the symmetry axis of the potential provides a direction along which the projection of j can be quantised. These projections are denoted by Ω and are good quantum numbers for the Nilsson orbits. In addition, $\pm\Omega$ states are degenerate. Thus, $(j + 1/2)$ non-degenerate quantum states are obtained for a given j. The energy ordering of these states explicitly depends on the nuclear shape. For example, the nucleon in the lowest (highest) Ω orbit has a maximum wave-function overlap with the prolate (oblate) core, thus the binding energy is the strongest. With increasing Ω values the binding energy decreases (increases) for a prolate (oblate) nucleus. This scheme is pictorially depicted in Fig. 2.3 and Fig. 2.4. In a major oscillator shell, a given Ω state can
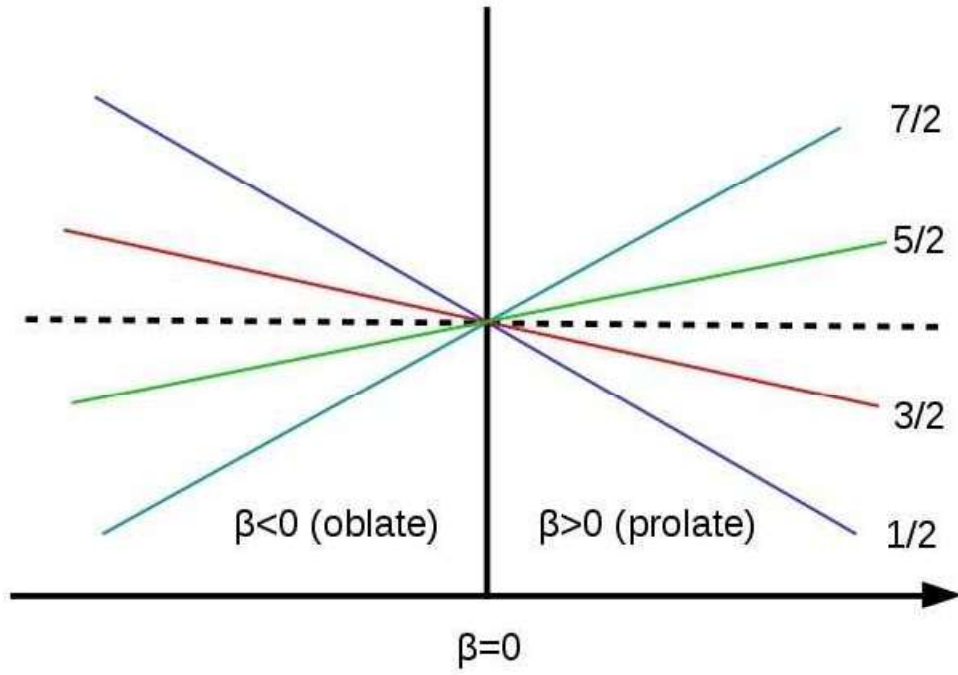
Figure 2.4: A schematic diagram for the single particle levels of the $j = 7/2$ orbital as a function of the quadrupole deformation (β).

have contributions from different j states due to the presence of the Y_{20} term in the Hamiltonian, provided their parity is the same. Thus,

$$\psi^{'}(\Omega) = \sum_{lj} a(Nlj)\psi_{Nlj}$$

These mixing amplitudes '$a(Nlj)$' are calculated by solving the Nilsson Hamiltonian [35]. A Nilsson diagram of single particle energy levels with deformation has been shown in Fig. 2.5.

Triaxial deformation: The nuclear shape has been associated with the shell occupancy of nucleons in the mid-shell region, where the occupancy of the nucleons in low (high) Ω orbital drives the nucleus towards a prolate (oblate) shape. Thus,
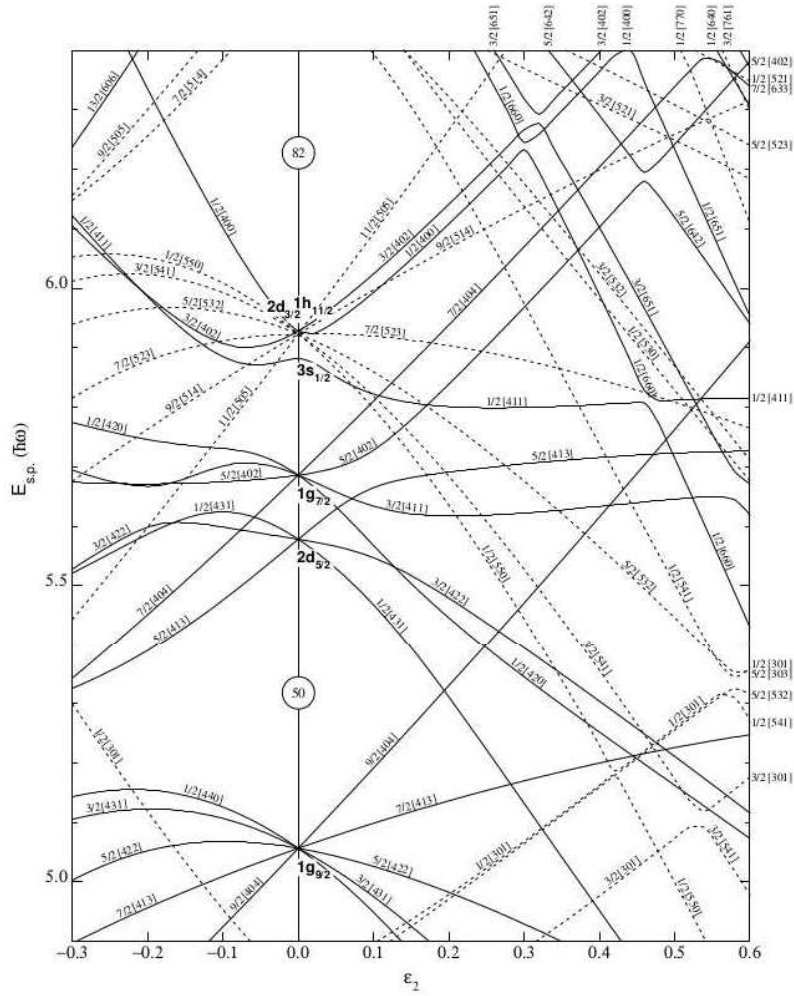
Figure 2.5: The Nilsson diagram for protons in the $50 \leq N \geq 82$ region.

when the protons and the neutrons exist in different shape driving orbitals, the nucleus on the average can acquire a triaxially deformed shape. In these nuclei, the axial symmetry is lost, so the good quantum number Ω loses its significance. The π-rotational symmetry still remains along with the parity.

2.3　High spin states in nuclei

The mean field models discussed above, quite successfully describe the behaviour of the nucleus in its body-fixed frame. However, the nuclear structure studies are carried out in the lab frame. These frames are the same for a spherical nucleus. But for a deformed nucleus, a suitable transformation from the body-fixed frame to the lab frame has to be done for the comparison with the experimental results.

2.3.1　Collective rotation: Axially deformed nuclei

An excited nucleus exhibits collective modes if the collective motion is slow compared to its intrinsic nucleon motion [36]. A collective band then develops on each of these intrinsic states. The even-even nuclei are best suited to observe the collective states, as the particle excitation modes are energetically unfavoured because of the strong pairing force.

To describe the rotation of a nucleus, the total Hamiltonian can be separated into two parts

$$H = H_{\text{rot}} + H_{\text{intr}} \tag{2.9}$$

where, H_{rot} and H_{intr} are the rotational and the intrinsic part of the rotor, respectively. This allows us to describe the wavefunction in a product form;

$$\Psi^I_{MK}(\vec{w}, \vec{r}) = D^I_{MK}(\vec{w})\chi_\omega(\vec{r}) \tag{2.10}$$

where, D^I_{MK} is the rotation matrix for Euler angle variable $\vec{\omega}(= \theta_1, \theta_2, \theta_3)$ and χ is the wave function for the intrinsic states of the even-even nucleus. K and M are depicted in Fig. 2.6.

For a even-even nucleus, $K = 0$:

$$\Psi^I_{K=0,M} = \sqrt{\frac{1}{2\pi}} \Phi_{K=0} Y_{I,M}(\theta, \phi) \tag{2.11}$$

In the limit of 'adiabatic approximation' [23], the rotational motion does not influence the intrinsic states and H_{rot} acts on $Y_{I,M}(\theta, \phi)$ to give energy eigen values

$$E_{\text{rot}}(I) = \frac{\hbar^2}{2\mathcal{J}} I(I+1) \tag{2.12}$$

where, $\mathcal{J}$ is the moment of inertia for rotation.

A different subgroup of symmetry appears as a result of the nuclear shape; the π-rotational symmetry around the rotation axis (x):

$$R_x(\pi) Y_{I,M} = (-1)^I Y_{I,M} = r Y_{I,M} \tag{2.13}$$

where, 'r' is the eigenvalue of $R_x(\pi)$. By two consecutive π rotation eventually the original situation is restored, i.e. $R_x^2(\pi) = 1$. This implies $r^2 = 1 => r = \pm 1$. Thus depending on the eigenvalues of r only odd or even values of I exist in a rotational band, i. e.

$$I = \begin{cases} 0, \ 2, \ 4, \ 6, \ .. \ r = +1 \\ 1, \ 3, \ 5, \ 7, \ .. \ r = -1 \end{cases} \tag{2.14}$$

In presence of valance nucleons, there is an interplay between the single particle excitation and the collective rotation. This leads to a wide variety of rotational bands. To describe the rotation of an odd mass or odd-odd mass nucleus, different models were developed. Few important models will be discussed here which

describe the high spin states of an axially deformed nucleus. These calculations are performed either in the laboratory frame or in the body fixed frame. In the first case, energy eigenvalues are calculated as a function of the total angular momentum, I, and thus, the calculations can be directly compared with experimental values. On the other hand, the calculations in the body fixed frame needs a convolution for the comparison, with the experimental values.

Particle rotor model
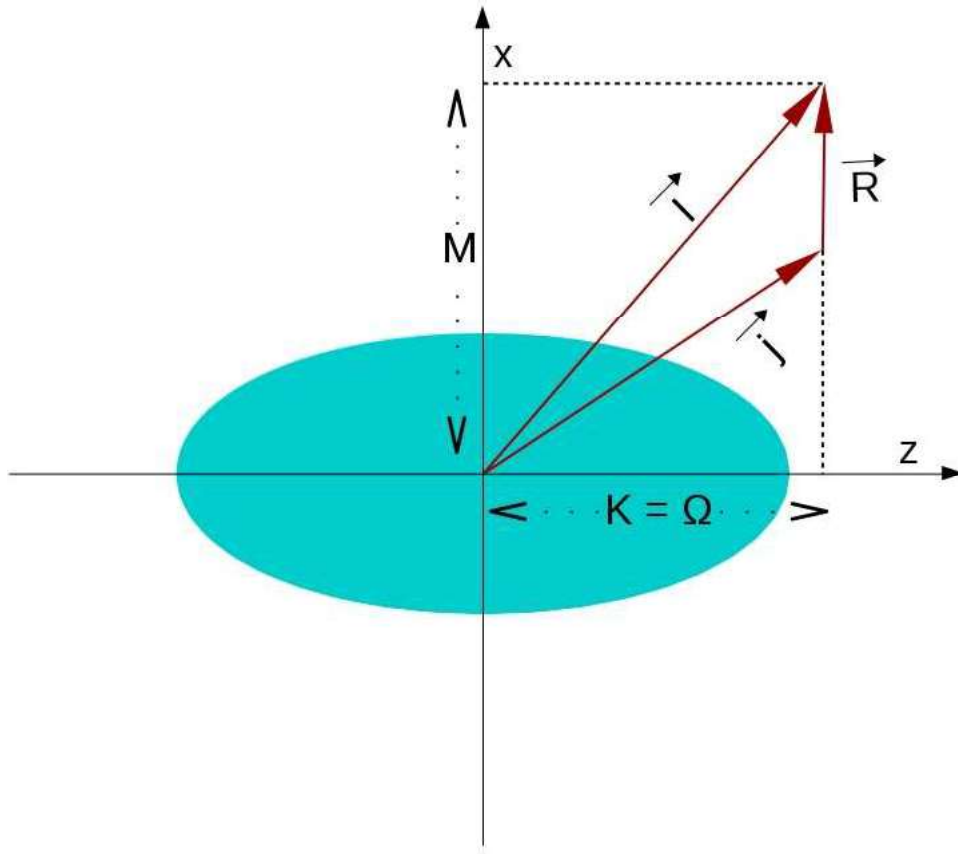
Figure 2.6: The schematic vector diagram for the particle rotor model. K and M are the angular momentum projections along the z (body-fixed) and the x (space-fixed) axes, respectively.

The particle rotor model (PRM) deals with the rotation of odd-mass and odd-

odd mass nuclei in the laboratory frame. In this model a core of the nucleus is assumed, where all the nucleons are arranged in time-reversed pairs. So the nucleus is treated as one or two valance particles and a even-even deformed core.

The single particle states in a deformed nucleus are described within the framework of Nilsson model. In PRM, the particle spin (j) is not a good quantum number but the total spin (I) of the nucleus is a good quantum number [18].

1. **Strong coupling limit**

   In the limit of strong coupling, we can construct the total spin, I, by the vector sum of the core angular momentum (R) and the particle angular momentum (j), i.e.

   $$\vec{I} = \vec{R} + \vec{j}$$

   (a) **The Hamiltonian**

   Let us consider z as the symmetry axis of the deformation, thus the rotation takes place about a perpendicular axis (x). Rotation part of the Hamiltonian can be written as

   $$
   \begin{aligned}
   H_{rot} &= \frac{\hbar^2}{2\mathcal{J}}[R_z^2 + R_y^2] \\
   &= \frac{\hbar^2}{2\mathcal{J}}[|\vec{I} - \vec{j}|^2 - (I_x - j_x)^2] \\
   &= \frac{\hbar^2}{2\mathcal{J}}[I^2 - I_z^2 - 2(I_x j_y + I_y j_x) + j^2 - j_x^2)]
   \end{aligned}
   \tag{2.15}
   $$

   By inclusion of ladder operators $I_\pm = I_z \pm i I_y$ and $j_\pm = j_z \pm i j_y$, the above equation becomes

   $$
   \begin{aligned}
   H_{rot} &= \frac{\hbar^2}{2\mathcal{J}}[I^2 - I_x^2 - (I_+ j_- + I_- j_+) + j^2 - j_x^2] \\
   &= H_0 + H_c + H_{sp}
   \end{aligned}
   \tag{2.16}
   $$

where $H_0 = \frac{\hbar^2}{2\mathcal{J}}[I^2 - I_x^2]$, $H_c = -\frac{\hbar^2}{2\mathcal{J}}[(I_+ j_- + I_- j_+)]$ is the rotor particle coupling term and $H_{sp} = \frac{\hbar^2}{2\mathcal{J}}(j^2 - j_x^2)$ is the single particle term.

(b) **The wave function**

Using Eq. 2.10 and Eq. 2.13

$$R_x(\pi) D_{MK}^I(\vec{w}) = e^{-i\pi I_x} D_{MK}^I(\vec{w}) = (-1)^{I+K} D_{M-K}^I(\vec{w}) \qquad (2.17)$$

The phase factor $(-1)^{I+K}$ is known as the 'signature quantum number', σ [23]. Taking the signature symmetry into account, the wave function of the particle plus rotor can be constructed as

$$\Psi_{MK}^I(\vec{w}, \vec{r}) = \frac{2I+1}{16\pi^2}[D_{MK}^I(\vec{w})\chi_K(\vec{r}) + (-1)^{I-j} D_{M,-K}^I(\vec{w})\chi_{-K}(\vec{r})]$$

$$(2.18)$$

(c) **The eigen values**

The energy of the system is found by solving the eigenvalue equation

$$H_{\text{rot}}\Psi_{MK}^I(\vec{w}, \vec{r}) = E(I; K)\Psi_{MK}^I(\vec{w}, \vec{r})$$

The rotor-particle coupling term, H_c, is zero except for $K = 1/2$, H_{sp} is constant in strong coupling limit, so the rotational energy for $K \neq 1/2$ can be written as

$$E(I : K) = \frac{\hbar^2}{2\mathcal{J}}[I(I+1) - K^2] + E_0(K)$$

The rotational band is developed on the ground state energy, $E_0(K)$,

and we obtain the rotational spectrum

$$I = K, \ K + 1, \ K + 2, \ K + 3 \ ... \qquad (2.19)$$

(d) **The signature staggering**

For $K = 1/2$, the particle rotor coupling term, $H_c \neq 0$, and can be calculated as [25]

$$
\begin{aligned}
\Delta E(I; K) = &- \delta_{K,1/2} \frac{\hbar^2}{\mathcal{J}} \langle D^I_{M,1/2} \chi_{1/2} | I_- j_+ | D^I_{M,-1/2} \chi_{-1/2} \rangle (-1)^{I-j} \\
=& \delta_{K,1/2} (-1)^{(I+1/2)} (I + 1/2) a
\end{aligned} \qquad (2.20)
$$

where, 'a' is the decoupling parameter, and is given by

$$a = \frac{\hbar^2}{\mathcal{J}} \sum_{nlj} (-1)^{j-1/2} (j + 1/2) |C_{nlj1/2}|^2$$

The total energy for $K = 1/2$ band becomes

$$E(I; K) = E_0(K) + \frac{\hbar^2}{2\mathcal{J}} [I(I+1) - K^2] + \delta_{K,1/2} a (-1)^{I+1/2} (I+1/2) \quad (2.21)$$

Thus, one of the signature partners becomes more favoured in energy than the other. This leads to an staggering of energy and intensity in the $M1$ transitions between the two signature partners. For an axially symmetric nucleus, the proximity of the Fermi levels to the $\Omega = 1/2$ orbital is essential to observe this interference effect, while in a triaxial nucleus this condition is not essential as in this case, Ω is not a good quantum number.

2. **Decoupling limit**

The limit of strong coupling holds true if the nucleus is strongly deformed. However, for weak deformation, the rotational part of the Hamiltonian (H_{rot}) is no longer separable from the intrinsic part (H_{int}), which means, the motion of the core effects the particle currents (mainly in large j orbits). In the decoupling limit, the particle orbit orients itself to align its angular momenta along the axis of rotation. The projection of j along the rotation axis is denoted by α and the energy spectrum of the rotor takes the form [24]

$$
\begin{aligned}
E(I;\alpha) &= \text{const.} + \frac{\hbar^2}{2\mathcal{J}}(I-\alpha)(I-\alpha+1) \\
&= \text{const.} + \frac{\hbar^2}{2\mathcal{J}}R(R+1)
\end{aligned}
\tag{2.22}
$$

Thus, we have

$$
I = \alpha,\ \alpha+2,\ \alpha+4\ ...
\tag{2.23}
$$

The difference between two extreme limits of particle rotor coupling has been depicted schematically in Fig. 2.7.
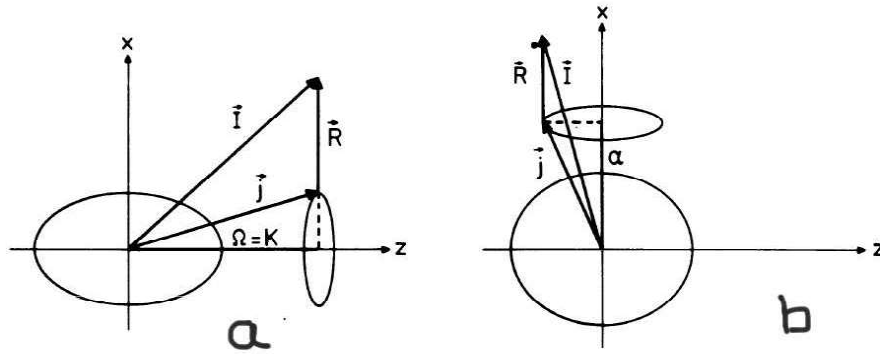
Figure 2.7: The vector diagrams of (a) the strong coupling scheme and (b) the decoupling scheme (right). Figure taken from Ref. [26].

Cranking model

The Cranking model provides a microscopic description of the nuclear rotation in the body fixed frame.

To describe the rotation in axially deformed nucleus, the nuclear field is externally rotated with a frequency ω about the principle axis (x). The Hamiltonian in the body fixed frame can be written as

$$H_\omega = \sum_i [h_0(i) - \hbar\omega j_x(i)] + H_{\text{pair}}$$

$$= H_0 - \hbar\omega J_x + H_{\text{pair}}$$

(2.24)

where, h_0 is the non-rotating single particle Nilsson Hamiltonian, j_x is the angular momentum projection of the i-th nucleon on the rotation axis . The total Hamiltonian is written as a sum of all single particle Hamiltonian $h_\omega = h_0 - \hbar\omega j_x$. The Nilsson wavefunctions are not eigenfunctions of j_x and thus, these states are mixed by the rotation. However, the signature (σ) and parity (π) remain good quantum numbers, from which we can construct a basis state $|\mu\rangle = |\pi\sigma\rangle$. In this basis the expectation value of the single particle Hamiltonian is

$$e^\omega = \langle\mu|h_\omega|\mu\rangle = \langle\mu|h_0|\mu\rangle - \omega\langle\mu|j_x|\mu\rangle$$

(2.25)

This implies

$$\frac{de^\omega}{d\omega} = -\langle\mu|j_x|\mu\rangle$$

(2.26)

Thus, the slope of the single particle energies as a function with rotational frequency is a measure of the single particle aligned angular momentum.

The cranking Hamiltonian is expressed in terms of single particle creation and

anihilation operator to include the effect of pairing correlation, i.e.

$$H = \sum_{ij} \left[H_0 a_i^+ a_j - \omega J_x a_i^+ a_j \right] - \sum_{i>j>} G a_i^+ a_{\bar{i}}^+ a_{\bar{j}} a_j \qquad (2.27)$$

where, G is the pairing strength. The pair term is linearised as

$$H_{pair} = -G\langle P\rangle \sum_{i>} (a_i^+ a_{\bar{i}}^+)/2 \qquad (2.28)$$

where,

$$a_i^+ a_{\bar{i}}^+ = \langle P\rangle = a_j^+ a_{\bar{j}}^+$$

The parameter $\Delta = G\langle P\rangle/2$ is extracted from the experimental odd even mass differences.

It is to be noted that the pairing term does not conserve the particle number. So the Fermi energy (λ) is introduced in the Hamiltonian as a Lagrangian multiplier to the particle number operator, N, and is so chosen to give the right vacuum configuration for the nucleus of interest. The complete Hamiltonian thus becomes

$$H_\omega = H_0 - \Delta(P^+ + P) - \omega J_x - \lambda N \qquad (2.29)$$

Once the Hamiltonian is defined, the eigen value problem in the quasi-particle basis can be written as

$$H'_{\sigma\omega}|\sigma\mu\rangle = E_{\sigma\mu}^\omega|\sigma\mu\rangle \qquad (2.30)$$

where,

$$|\sigma\mu\rangle = \begin{pmatrix} U_{\sigma i}^{\sigma\mu} \\ V_{\sigma-i}^{\sigma\mu} \end{pmatrix} \qquad (2.31)$$

and

$$H'_{\sigma\omega} = \begin{pmatrix} (\epsilon_i - \omega J_x - \lambda)_{\alpha_i \alpha'_i} & \Delta \\ \Delta & -(\epsilon_i - \omega J_x - \lambda)_{-\alpha_i -\alpha'_i} \end{pmatrix} \qquad (2.32)$$

Here, μ stands for the quantum number other than signature.

Comparison with experiment: The predictions of this model cannot be directly compared with the experimentally obtained data, as the energy of each state is obtained as a function of spin (I) in experiment, but in this model the quasi-particle energy is calculated as a function of rotational frequency (ω). For the comparison, an experimental Routhian is constructed as

$$E_\omega = \frac{1}{2}[E_{I+1} + E_{I-1}] - \omega I_x \qquad (2.33)$$

where, the ω and I_x for a spin state (I) in a given signature band can be calculated as

$$\hbar\omega = \frac{E_{I+1} - E_{I-1}}{I_x(I+1) - I_x(I-1)}$$
$$I_x = \sqrt{(I + 1/2)^2 - K^2} \qquad (2.34)$$

where, K is the angular momentum projection along the symmetry axis. From this, the relative energy is calculated as

$$e_\omega = E_\omega - E_\omega^{\text{ref}} \qquad (2.35)$$

where, E_ω^{ref} is the energy of the ground state band of the nearest even-even nucleus. Similarly, the relative aligned angular momentum is calculated from this neighbor

nucleus as

$$i_x = I_x - I_x^{\text{ref}} \tag{2.36}$$

The parameters of the reference nucleus are obtained by using the Harri's parameters (J_0, J_1) in the relations

$$
\begin{aligned}
I_x^{\text{ref}} &= (J_0 + \omega^2 J_1)\omega \\
E_\omega^{\text{ref}} &= -\frac{\omega^2}{2}J_0 - \frac{\omega^4}{4}J_1 + \frac{1}{8J_0}
\end{aligned}
\tag{2.37}
$$

These relations are used to compare the predictions of the cranking model with the experimentally obtained rotational level-scheme of nuclei.

Although the cranking model proves to be fruitful in describing experimental results, it has an important shortcoming. The resulting wave functions from cranking model are not the eigenstates of the angular momentum operator. Thus, the expectation values of the electromagnetic transition operators cannot be calculated [24]. This problem can be circumvented by employing the angular momentum projection technique.

Method of angular momentum projection

In the Nilsson basis, the nuclear wave function $|\Phi\rangle$ can be decomposed into the eigenstates of the operator J_z, i.e.

$$|\Phi\rangle = \sum_{K'} |\Phi'_K\rangle \; ; \; J_z|\Phi_K\rangle = K|\Phi_K\rangle \tag{2.38}$$

Angular momentum is not a conserved quantity in this basis. So a projection operator, P_{MK}^I, is used to project the good angular momentum states. The operator

is defined as

$$P^I_{MK} = \frac{2I+1}{8\pi^2} \int D^I_{MK}(\Omega) R(\Omega) d\Omega$$
$$R(\Omega) = e^{i\alpha j_z} e^{i\beta j_y} e^{i\gamma j_x}$$

(2.39)

where, $\Omega(=\alpha, \beta, \gamma)$ is the set of Euler angles. P^I_{MK} acts on the component $|\Phi_K\rangle$ and transforms it into the eigenfunctions of J^2 and j_x with quantum numbers I and M respectively. All the other components with $K' \neq K$ are canceled out [24]. In this projected basis, the total wavefuntion is written as

$$|\Psi^I_{MK}\rangle = \sum_{K,k} g_K P^I_{MK} |\Phi_{K,k}\rangle$$
$$= \sum_{K,k} g_K \frac{2I+1}{8\pi^2} \int d\Omega D^I_{MK}(\Omega) R(\Omega) |\Phi_{K,k}\rangle$$

(2.40)

The Hamiltonian is then minimized with respect to the coefficients, g_K, to obtain the energy. The projected energy is given by

$$E^I_{\text{proj}} = \frac{\langle \Psi^I_{MK} | H | \Psi^I_{MK} \rangle}{\langle \Psi^I_{MK} | \Psi^I_{MK} \rangle}$$

(2.41)

For an odd or odd-odd nucleus, a quasiparticle basis state is chosen from the desired model. Then using the projection technique good angular momentum states are projected in the lab frame. Each of these states gives a band structure. However, only the states near the Fermi level are relevant. Thus, the set of quasi-particle levels close to the Fermi level are taken as the principal contributors. A band-mixing calculation involving the projected bands is then performed to obtain the rotational band structures.

In the recent times, the Triaxial Projected Shell Model (TPSM) calculations

were applied successfully to describe multiple band structures in odd-odd triaxial nuclei [37, 38]. Thus, the angular momentum projection techniques allows us to construct the 'good angular momentum' states from the body fixed single particle models. However, in this case the band mixing calculations are performed within a fixed energy window (typically 2.5 MeV above the minimum energy quasi-particle level) and the other quasi-particle configurations are ignored.

2.3.2 Shears mechanism

A new angular momentum generation mechanism was proposed to describe the observed band structures in near spherical Pb isotopes [30].

A systematic study shows, these bands in Pb nuclei begin at moderately high spins ($I \sim 17\hbar$). The g-factor measurements [39] were carried out to establish the quasi particle configurations at the band-head. It was observed that, all these $M1$-bands in Pb nuclei are developed on a quasiparticle configuration with protons in high-Ω orbitals and neutrons in low-Ω orbitals, e.g. $[\pi(h_{9/2}i_{13/2}) \otimes \nu i_{13/2}^{-1}]$ in ^{193}Pb [31]. This quasi particle arrangement suggests that the protons (particles) and the neutrons (holes) spins are aligned perpendicularly at the band-head, where the band-head spin, I_b, could be found by the vector addition of the particle spin (j_p) and the hole spin (j_h), i.e.

$$I_b = \sqrt{|\vec{j_p}|^2 + |\vec{j_h}|^2} \qquad (2.42)$$

The total spin is thus tilted with respect to either of the principle axes. A $M1$ band structure is evident if the nucleus is cranked along the direction of this total spin. It is to be mentioned here that, the currents in the quasiparticle orbits create an asymmetry about the spin axis and thus rotation about this axis is possible. Frauendorf modelled this phenomena in a framework called the 'Tilted

Axis Cranking' (TAC) model [40].

These $M1$ bands in Pb isotopes possess some unique properties [32]:

1. The energy of the states follow a relation $E(I) - E_b \sim (I - I_b)^2$; where E_b is the energy at the band-head.

2. Cross-over $E2$ transitions are either absent or very weak, this results in a large $B(M1)/B(E2)$ ratios ($\geq 20\ \mu_N^2(eb)^{-2}$).

3. The $M1$ transition intensities are enhanced and at the band-head the $B(M1)$ rates are very high, which falls steadily with increasing spin.

4. At a given spin, the ratio of the dynamic moment of inertia and the $E2$ transition rate is very large, i.e. $\mathcal{J}^{(2)}/B(E2) \geq 100\ Mev^{-1}(eb)^{-2}$ compared to the value of $\sim 10\ Mev^{-1}(eb)^{-2}$ in deformed nuclei.

These properties could be described successfully in the framework of TAC. The solutions of TAC model indicate that the high-spin states are formed when the particle and the hole spins align themselves simultaneously along the direction of the total spin and are completely aligned at the maximum spin of the band. Thus, a shears like structure can be visualised where the two blades are associated with the angular momentum vectors of the particles and the holes, respectively. At the band-head, the shears is opened maximally with the shears angle at 90^0, and at the maximum spin the shears is closed with the shears angle close to 0^0. This geometrical picture (Fig. 2.8) of angular momentum generation mechanism is known as the 'shears mechanism' [41].

In this picture, the increase in band energy with the shears closing can be associated with the rise in the potential energy due to the compression of a spring

attached between the shears blades. In reality, the elasticity of the spring symbol-
izes the repulsive nature of the particle-hole coupling. A close resemblance to this
particle-hole interaction can be obtained by taking a potential of the form $V_2 P_2(\theta)$.
Thus, the level energy of the shears band can be written as a function of the shears
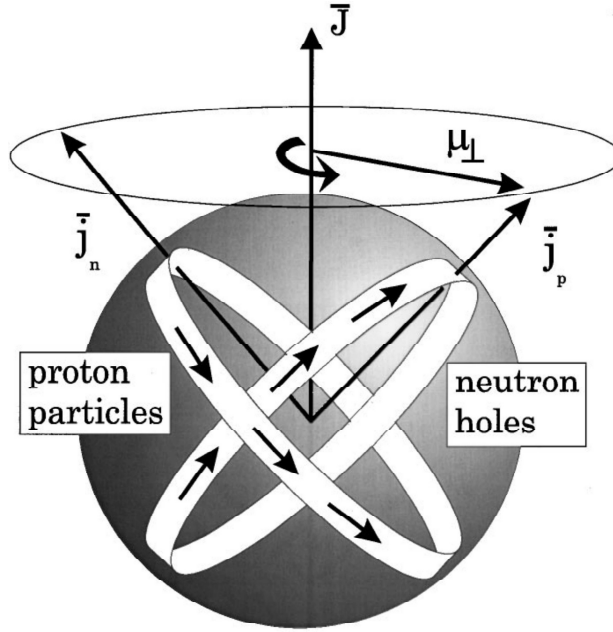
Figure 2.8: The schematic representation of the shears structure. Figure taken
from Ref. [34]

angle (θ):

$$E(\theta) = E_0 + V_2 \frac{3cos^2(\theta) - 1}{2} \tag{2.43}$$

where, the shears angle for a given spin state (I) is obtained as:

$$\vec{I} = \vec{j}_\pi + \vec{j}_\nu$$

$$=> |\vec{I^2}| = |\vec{j_\pi^2}| + |\vec{j_\nu^2}| + 2|\vec{j_\pi}||\vec{j_\nu}|cos(\theta) \tag{2.44}$$

$$=> cos(\theta) = \frac{|\vec{I^2}| - |\vec{j_\pi^2}| - |\vec{j_\nu^2}|}{2|\vec{j_\pi}||\vec{j_\nu}|}$$

The currents in the quasi-particle orbits give rise to a magnetic moment, $\mu_\perp$, perpendicular to the total spin. The direction of this $\mu_\perp$, rotates with increasing spin, thus the mode of excitation is also known as the 'magnetic rotation'. On the other hand, a decreasing amplitude of $\mu_\perp$ with closing of the shears blades results in a falling trend of $B(M1)$ rates with increasing spin, as $B(M1) \propto \mu_\perp^2$. In this semi classical picture, the $M1$ transition rates can be calculated as [41]

$$B(M1; I \rightarrow I-1) = \frac{3}{4\pi}(g_\pi - g_\nu)^2 \frac{1}{2} sin^2(\theta_\pi) \qquad (2.45)$$

where, g_ν and g_π are the g-factors for the neutrons and the protons, respectively and θ_π is the angle between the proton spin and the total spin. θ_π can be calculated as

$$tan(\theta_\pi) = \frac{j_\nu sin(\theta)}{j_\pi + j_\nu cos(\theta)} \qquad (2.46)$$

In a microscopic picture, the transition rates can be calculated using the shell-model basis states [42], which is given by

$$B(M1; I \rightarrow I-1) = \frac{3}{4\pi}(g_\nu - g_\pi)^2 \frac{(2j_\nu + 1)^2(2j_\pi + 1)^2}{16I(2I+1)} sin^2(\theta) \qquad (2.47)$$

Apart from the $B(M1)$ rates, the $B(E2)$ rates also show a falling trend with increasing spin. This observation relies on the fact that, the nucleus attains a more symmetric charge distribution as the shears is closed. Semi classically, the $B(E2)$ values are estimated as [32]

$$B(E2; I \rightarrow I-2) = \frac{5}{16\pi}(eQ_{\text{eff}})^2 \frac{3}{8} sin^4(\theta_\pi) \qquad (2.48)$$

where, Q_{eff} is the effective quadrupole moment of the nucleus. This effective mo-

ment includes, the contributions from both the protons and the neutrons orbitals, i.e.

$$(eQ)_{\text{eff}} = e_\pi Q_\pi + \left(\frac{j_\pi}{j_\nu}\right)^2 e_\nu Q_\nu \tag{2.49}$$

where, e_π and e_ν are related with the polarisation charge e_{pol} by the formula

$$e_{\text{eff}} = e(\frac{1}{2} - t_z) + e_{\text{pol}} \tag{2.50}$$

where, $e_{\text{eff}} = e_\pi(e_\nu)$ for $t_z = +\frac{1}{2}(-\frac{1}{2})$. The value of polarisation charge is a measure for the number of protons involved in shears mechanism. For example, the polarisation charge estimation shows $e_{pol} \sim 3e$ for a two protons hole structure [33], while $e_{pol} \sim 5e$ for a three protons hole structure [7].

Competition between the shears mode and the core rotation

The Pb nuclei are very weakly deformed ($\epsilon \leq 0.1$) [32]. Thus, the core rotation cannot interfere with the shears mechanism in these nuclei. However, in a moderately deformed nucleus, the core rotation co-exist with the shears mechanism. Clark and Machiavelli described this interplay in the framework of a semi-classical particle rotor model [32]. In this model the total angular momentum (I) is divided into two parts, the core rotation (R) and the shears angular momentum (I_{sh}), i.e.

$$\vec{I} = \vec{R} + \vec{I_{\text{sh}}}$$

and the energy of the band is given by

$$
\begin{aligned}
E(I) &= \frac{\vec{R}^2}{2\mathcal{J}} + V_2\frac{3cos^2(\theta)-1}{2} \\
&= \frac{(\vec{I} - \vec{j_\pi} - \vec{j_\nu})^2}{2\mathcal{J}} + V_2\frac{3cos^2(\theta)-1}{2}
\end{aligned}
\tag{2.51}
$$

where, $\mathcal{J}$ is the collective moment of inertia. Since the total angular momentum is generated due to an interplay between the collective rotation and the shears mechanism, the collective moment of inertia is expected to have a lower value compared to those used in the PRM calculations.

This interplay has been modeled in two ways:

1. **Fixed tilt angle :**

   If the rotational contribution is small ($\sim 4\hbar$), then the shears structure is
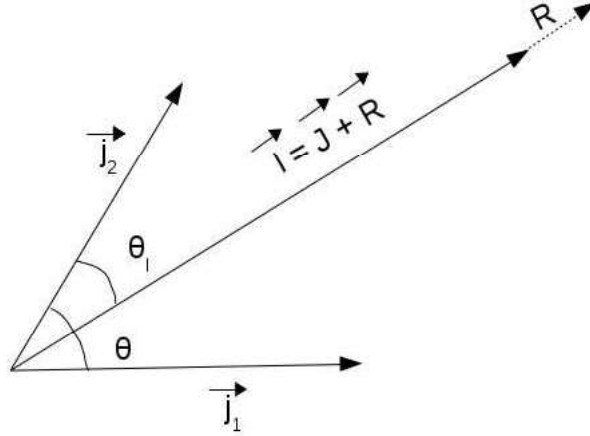
Figure 2.9: The vector diagram of the fixed tilt angle scheme.

not modified by it and the high spin states are generated by keeping the tilt angle, θ_I, fixed.

For the two shear blades with angular momenta j_1 and j_2, the maximum spin that can be achieved by shears closing is $I_{\text{sh}}^{\text{max}} = j_1 + j_2$. But due to the

presence of core rotation, the band extends up to I_{max}. So, the contribution from core rotation can be calculated as:

$$\Delta R = (I_{\text{max}} - I_{\text{sh}}^{\text{max}})$$

ΔR is then distributed uniformly over the whole spin range, $\Delta I = (I_{\text{max}} - I_b)$. Under this non-perturbative approximation, for every spin state I

$$R_{\text{core}} = \left(\frac{\Delta R}{\Delta I}\right)(I - I_b) \qquad (2.52)$$

As a result of this additive collective contribution to every level, the shears closing process slows down by a small amount. It is to be mentioned that this approximation holds true only if the core contribution is small, such that $\frac{\Delta R}{\Delta I} \lesssim 10\%$ [43].

2. **Variable tilt angle: SPAC**

For many shears bands observed in the nuclei of mass-100 and mass-140 regions, the shears configuration is associated with a moderately deformed core. For these nuclei, the collective contribution is around 30%. This large core contribution can be accounted in the formalism of the 'shears with principle axis cranking' (SPAC) model [9]. In this model, the core rotation is assumed to be strong enough to keep $\vec{j_2}$ aligned along the rotation axis and hence, the tilt angle of $\vec{I}$ changes continuously as a function of spin. The corresponding vector diagram has been shown in Fig. 2.10. From the vector diagram,

$$\left|\vec{R}(I,\theta)\right| = \sqrt{I^2 - (j_1 sin\theta)^2} - j_1 cos\theta - j_2 \qquad (2.53)$$
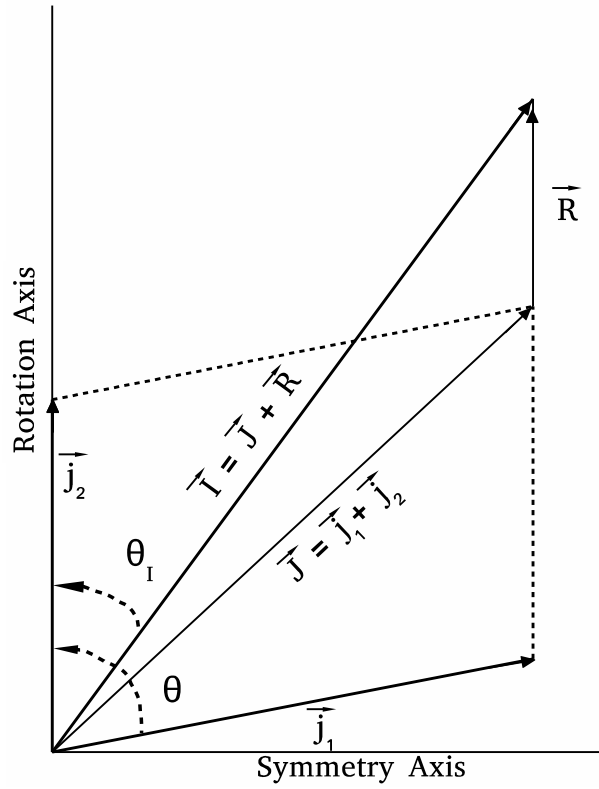
Figure 2.10: The vector diagram of the variable tilt angle scheme.

The value of θ for each spin state is then obtained from the energy minimization condition

$$\left(\frac{dE}{d\theta}\right)_I = 0$$

These θ values are then used to calculate the Routhian, $E(I)$, and the transition rates. In this framework, the $B(M1)$ rates are obtained using the formula

$$B(M1)(I \rightarrow I - 1) = \frac{3}{8\pi}[j_1 g_1^* sin(\theta - \theta_I) - j_2 g_2^* sin(\theta_I)]^2 \qquad (2.54)$$

where $g_1^* = g_1 - g_R$, $g_2^* = g_2 - g_R$ and $g_R = (Z/A)$; Z and A are atomic

number and mass number of the nucleus respectively. The $B(E2)$ rates are given by

$$B(E_2)(I \rightarrow I - 2) = \frac{15}{128\pi}[Q_{\text{eff}}sin^2\theta_{1j} + Q_{\text{coll}}cos^2\theta_I]^2 \qquad (2.55)$$

where Q_{eff} and Q_{coll} are the quasi particle and the collective quadrupole moments respectively.

The Q_{eff} can, in turn, be correlated to e_{pol} using equations 2.49 and 2.50.

Anti magnetic rotation

The existence of a shears structure opens up the possibility to observe a double shears structure. A double shears structure (Fig. 2.11) results when two deformation aligned high-j holes in time reversed orbits co-exist with rotation aligned particles. Here, the two oppositely aligned holes independently couple with the particles to create a double shears structure. As a consequence of this single particle configuration, the rotational symmetry is broken along the total angular momentum direction. To generate higher spin states, these two shears closes simultaneously. In this case, the magnetic moments of the two anti-parallel holes cancel out and hence, the mode is called 'anti magnetic rotation' (AMR). On the other hand, the π-rotational symmetry about the total spin direction is broken spontaneously to result in a band structure composed of $E2$ transitions. With increasing spin, the nuclear shape changes to a more symmetric shape, because of the hole alignments. This fact is reflected in the decreasing $B(E2)$ rates with
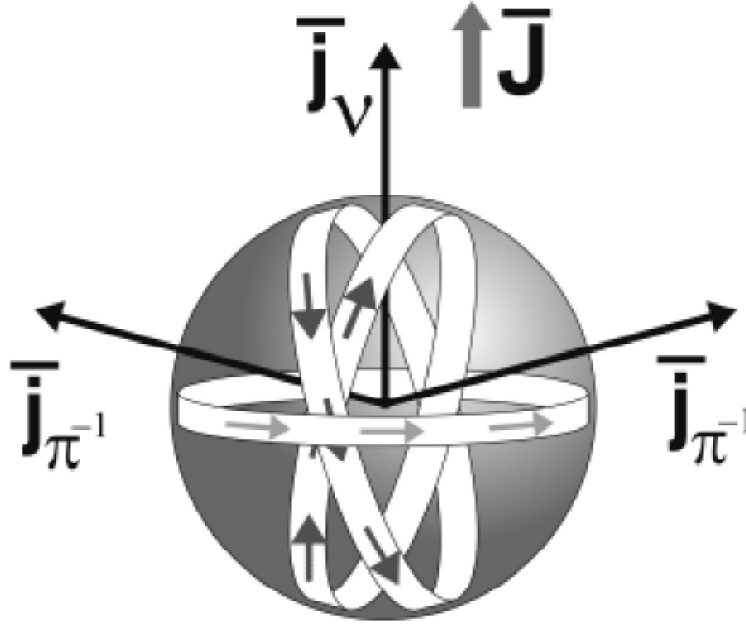
Figure 2.11: The schematic representation of AMR. Figure taken from Ref.[44].

increasing spin. The $B(E2)$ rates can be calculated using the formula [44]

$$B(E2) = \frac{15}{32\pi}(eQ_{\text{eff}})^2 \left[1 - \left(\frac{I - j_\nu}{2j_\pi}\right)^2\right] \qquad (2.56)$$

Moreover, a large $\mathcal{J}^2/B(E2)$ value (> 100 MeV$^{-1}\hbar^2(eb)^{-2}$) is obtained for the AMR bands, which is characteristically different from the rotational bands obtained for conventional nuclear rotation, where $\mathcal{J}^2/B(E2)$ value is ~ 10 MeV$^{-1}\hbar^2(eb)^{-2}$ [45]. In some nuclei the coexistence of anti magnetic rotation and collective rotation has also been found [46].

We have seen that a shears structure is formed when the single particle configuration supports a particle-hole structure. However, a similar configuration in a triaxial nucleus, may lead to an interesting phenomenon.

2.3.3 Spin chirality

In a triaxial nucleus, the particles and the holes may couple in such a way that the particle's spin ($\vec{j}_p$) is aligned along the short axis and the hole's spin ($\vec{j}_h$) is aligned along the long axis [47]. The nuclear core, on the other hand, prefers to rotate around the intermediate axis (y) of deformation, as the moment of inertia is the largest about this axis. For a large enough core spin ($\vec{R}$), three mutually perpendicular angular momenta give rise to a chiral geometry. As can be seen in Fig. 2.12, the chiral geometry give rise to a left handed system $|L\rangle$ and a right handed system $|R\rangle$), which are coupled by the chiral operator $\mathcal{T}R_y(\pi)$, i.e.
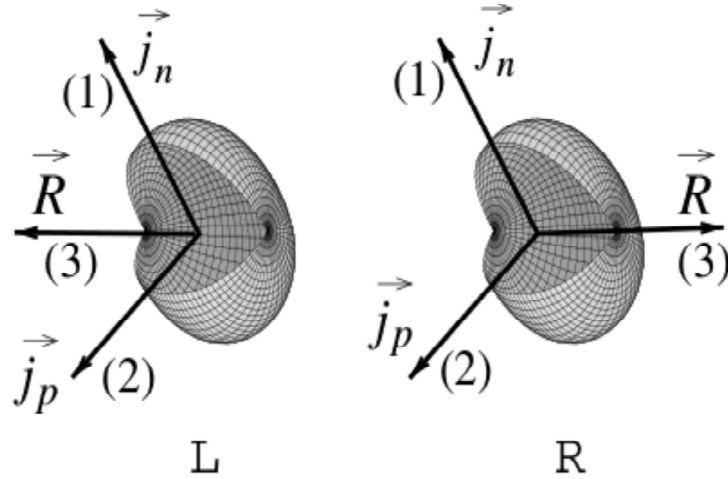
Figure 2.12: A pictorial representation of the chiral geometry. Figure taken from Ref. [47].

$$|R\rangle = \mathcal{T}R_y(\pi)|L\rangle$$
$$|L\rangle = \mathcal{T}R_y(\pi)|R\rangle$$

$$(2.57)$$

where, $\mathcal{T}$ represents the time-reversal operator. Now, the Hamiltonian of the system must be invariant under chiral transformation, i.e.

$$[H, \mathcal{T}R_y(\pi)] = 0 \tag{2.58}$$

Thus, H and $\mathcal{T}R_y(\pi)$ must have simultaneous eigenfunctions. A linear combinations of the wavefunctions of the right and the left handed systems can be assumed for this purpose, i.e.

$$
\begin{aligned}
|+\rangle &= \frac{1}{\sqrt{2}}(|R\rangle + |L\rangle) \ ; \ \mathcal{T}R_y(\pi)|+\rangle = |+\rangle \\
|-\rangle &= \frac{i}{\sqrt{2}}(|R\rangle - |L\rangle) \ ; \ \mathcal{T}R_y(\pi)|-\rangle = |-\rangle
\end{aligned}
\tag{2.59}
$$

Under the condition of strong symmetry breaking, i.e. $\langle R|H|L\rangle = \langle L|H|R\rangle^* = 0$, two eigenstates $|-\rangle$ and $|+\rangle$ are degenerate in the intrinsic frame of reference, thus, in the lab frame a pair of bands are formed with exact degeneracy. On the other hand, a non-zero value of $\langle R|H|L\rangle$ could be treated as a perturbation which mixes the pure states $|L\rangle$ and $|R\rangle$ and lifts the degeneracy.

Weak symmetry breaking is observed in the lab frame when the nuclear core rotation is small. The two non-degenerate bands grow together, while the strength of interband connecting transitions gives a measure of their mutual interaction. With increasing core contribution the chiral geometry becomes purer, and the energy of the partner bands become nearly degenerate at high spin. A close to the ideal situation has been observed in the partner bands of ^{126}Cs nucleus (Fig. 2.13), where the complete set of electromagnetic selection rules for chirality has been experimentally confirmed [47]. Most importantly, the interband $B(M1)$ staggering for the partner $\rightarrow$ yrast and the yrast $\rightarrow$ partner bands was observed in an

opposite phase with the inband $B(M1)$ staggering, which establishes the strong chiral symmetry breaking in the ^{126}Cs nucleus [48]. These identification of 'chiral

Figure 2.13: The chiral doublets observed in ^{126}Cs nucleus [48].

doublets' could be done from the following properties [28, 34, 47]

1. Same trend for in-band transition rates with spin.

2. The ratio of $B(M1)_{\text{in}}/B(M1)_{\text{out}}$ should be same for both the bands.

3. The staggering parameter, $S(I)\big(=\frac{E(I)-E(I-1)}{2I}\big)$, for both the bands should show a smooth variation with spin.

2.4 Study of A ∼ 100 region nuclei in high spin physics

In the present thesis, the high spin structure of Ag nuclei of $A \sim 100$ region have been studied. The primary motivations for this study are:

1. For the nuclei in A $\sim$ 100 region, the proton numbers are close to the shell closure at $z = 50$. A large shell gap limits the proton excitation across the shell gap. This reduces the configuration space for protons and theoretical calculations becomes easier.

   On the other hand, the neutron number ranges between $N = 50 - 65$. In this domain, $h_{\frac{11}{2}}$ is the intruder orbital with unique (negative) parity (Fig. 2.5). This makes a easy identification for the negative parity bands. In addition, the alignment of neutrons in $h_{\frac{11}{2}}$ orbital leads to a large gain ($\sim 8\hbar$) in the particle angular momentum.

2. A particle-hole configuration is natural in the odd or odd-odd nuclei of this mass region. The protons occupy high Ω orbitals of the $g_{\frac{9}{2}}$ orbital while the aligned neutrons occupy the low Ω orbitals of $(d_{\frac{5}{2}}/g_{\frac{7}{2}})$ and/or $h_{\frac{11}{2}}$. This configuration is suitable for the shears mechanism and has been reported in a large number of nuclei in this mass region [49]. On the neutron rich side, the cores are moderately deformed and an interplay of collective rotation with the shears mechanism is to be expected [7, 10, 13]. This may lead to a variety of interesting band structures.

   In the Cd and Pd isotopes, the two time reversed proton holes in $g_{\frac{9}{2}}$ orbitals and aligned neutrons in the $h_{\frac{11}{2}}$, $g_{\frac{7}{2}}$ and $d_{\frac{5}{2}}$ orbitals create a double shears

structure and the phenomena of AMR can be observed [46, 45, 50].

3. The shape driving effects of the low-Ω particle and the high-Ω hole orbitals are suitable to produce a stable triaxial deformed shape [47]. Thus, nuclei in this mass region are ideal to search for the foot prints of triaxiallity [51, 12]. This also facilitates the search for spin-chirality in the odd-odd nuclei [52, 53] of this mass region.

In the next chapter, the experimental techniques utilized to investigate the high-spin behaviour of the atomic nucleus, will be discussed in brief.

3

Experimental techniques and methods of

γ-spectroscopy

3.1   Introduction

With the discovery of radioactivity, the physicists found a way to probe the atomic nucleus and various nuclear properties could be studied by measuring properties of the α, β and γ radiations, emitted by the radioactive nuclei. However, these are finite number of nuclei. The accelerators, on the other hand, allow us to synthesize specific nuclei away from the line of stability and study specific structure properties. The in-beam experiments also demand sophistication in detection techniques and thus, specific detectors were developed. Among the vast field of nuclear physics instrumentation, this chapter will only cover the techniques relevant to this thesis work.

3.2   Heavy ion induced fusion evaporation reaction

A substantial amount of angular momentum can be transferred to nuclei using the heavy ion beams from the accelerators. The high angular momentum states in a nucleus can be populated mainly through two processes:

1. Coulomb excitation

2. Fusion evaporation reaction

For the process of Coulomb excitation, the beam energy is chosen slightly below the Coulomb barrier of the target-projectile combination. In this way, the projectile interacts with the target via Coulomb interaction only and no compound nucleus is formed. Thus, only the stable isotopes can be studied using this mode of excitation, in contrast to the fusion evaporation reaction. The present work concerns with the second mode of excitation using heavy ion beams.

The term heavy ion is used for any projectile with $A > 4$ [20]. In heavy ion induced fusion evaporation reaction, the heavy ion projectile approaches the target nuclei with sufficient kinetic energy to overcome their Coulomb barrier. The Coulomb barrier in the center of mass (C.O.M) frame is given by

$$V_{\mathrm{CM}}^c = \frac{Z_P Z_T e^2}{1.2(A_P^{1/3} + A_T^{1/3})} \tag{3.1}$$

where, $Z_P(Z_T)$ and $A_P(A_T)$ are the atomic number and mass number of the projectile (target), respectively. A conversion to the lab frame is done by using the formula

$$V_{\mathrm{LAB}}^c = \frac{A_P + A_T}{A_T} V_{\mathrm{CM}}^c \tag{3.2}$$

For a beam energy greater than V_{LAB}^c, there is a finite probability that the target and the projectile are fused together and a compound nucleus is formed. For a projectile energy E_P, the excitation energy of the compound nucleus in the C.O.M frame is given by

$$E_{\mathrm{CM}} = E_P \left(1 - \frac{M_P}{M_P + M_T} \right) \tag{3.3}$$

And the maximum angular momentum that can be transferred to the compound nucleus is

$$l_{\mathrm{max}} = \left(\frac{2\mu R^2}{\hbar^2}(E_{\mathrm{CM}} - V_{\mathrm{CM}}^c) \right)^{1/2} \tag{3.4}$$

where, μ is the reduced mass and $R\big(= 1.2(A_P^{1/3} + A_T^{1/3})\mathrm{fm}\big)$ is the maximum nucleus-nucleus distance for reaction to occur.

In fusion reaction, the compound nucleus reaches its thermodynamic equilibrium in $\sim 10^{-20}$ second [54]. By this time the nucleus loses its memory of formation and starts decaying to gain stability. The energy loss mainly takes place by the emission of high-energy statistical γ-rays or particles (α, p, n). Initially, the nucleus prefers to emit neutrons as the Coulomb barrier prevents charge particles like α or protons to escape. Once a nucleus is sufficiently neutron deficient, the probability of charge particle emission increases. A large amount of energy but only few units ($\hbar$) of angular momentum is carried away by the emitted particles. Once the nucleus reaches its particle emission threshold, the residual nucleus is left at a large angular momentum but low excited state. In this stage, the only way to lose energy and angular momentum is through discrete γ-emission. Thus a sequence of γ-transitions are emitted by the nucleus to reach its ground state. It takes $\sim 10^{-17}$ seconds for the compound nucleus to decay into its residual nucleus. It is to be noted that, the residual nucleus might be β unstable and may soon

decay to a stable isotope. However, the lifetime of this meta-stable state is long enough to gain stability against the γ-emission. In this way, the high spin states of nuclei away from the β-stability line can be populated and studied through discrete gamma spectroscopy.

Beam facilities: In the present thesis work, the fusion evaporation reactions were studied using the heavy ion beams of ^{14}N and ^{18}O. The 68 MeV ^{14}N beam was provided by the 14-UD pelletron at Tata Institute of Fundamental Research (TIFR), Mumbai, whereas the 70 MeV ^{18}O beam was provided by the 15-UD pelletron at Inter University Accelerator Center (IUAC), Delhi.

The Pelletron accelerators uses SNICS type ion-source to create a -ve charge state in the projectile atoms. A large positive voltage ($\leq$ 15 MeV) relative to the ion-source is maintained. In order to create the high voltage, static charge is accumulated by using a rotating belt composed of multiple metal pellets. Because of the electrostatic attraction, the -ve ions from the ion source gain kinetic energy and accelerate towards the stripper foil. In their flight path, they pass through the stripper foil and most of their electrons are removed. These positively charged ions then experiences a second acceleration due to the electromagnetic repulsion. In this way, the pelletron uses a two step (tandem) acceleration process to produce heavy ion energetic beams.

A specific target projectile combination is chosen to populate the nuclei of interest. The beam energy is tuned properly to increase the production cross-sections. The emitted discrete γ-rays are then detected and analyzed, to extract the properties of the high spin nuclear levels of the residual nuclei.

3.3 γ-ray detection

When a γ-ray enters a detector material it interacts via three processes:

1. **Photoelectric absorption**: In this process, a strongly bound atomic electron of the detector material gains kinetic energy by absorbing the incident photon completely. These are called 'photoelectrons'. For an incident γ of frequency ν, the electron with binding energy, B_e, gains a kinetic energy

$$T_e = h\nu - B_e$$

An output pulse is generated when these photoelectrons are collected at the electrode of a detector. In addition, an X-ray emission takes place when a electron from higher excited level makes a transition to fill the vacancy created by the photoelectron. This X-ray is also absorbed in the detector material. In this way the complete energy absorption of a photon is possible. The effect of photoectric absorption is highly dependent on the atomic number of the detector material (Z) as well as the γ energy, where the absorption cross-section is

$$\sigma \propto \frac{Z^n}{E_\gamma^n}$$

where, n= 4 or 5 depending on the Z value. Thus, the use of high-Z detector materials increases the photo-peak efficiency.

2. **Compton scattering**: In this process, the γ-ray transfers a part of its energy to an electron through the scattering process. For a scattering angle,

θ, the kinetic energy transferred to the electron is given by

$$T_e = \frac{E_\gamma^2(1 - cos(\theta))}{m_0 c^2 + E_\gamma(1 - cos(\theta))}$$

A detector pulse is produced by the collection of these electrons. The Compton scattered γ-ray suffers multiple such scatterings unless and until it gets absorbed through photoelectric process or escapes the detector. While the first process contributes to the photopeak, the second process gives rise to a continuous Compton background.

3. **Pair production**: The process of pair production takes place in the close proximity of the atomic nucleus [55], for γ-ray energies exceeding 1.02 MeV. The pair production process creates a electron-positron pair through the spontaneous disappearance of the photon. Both the electron and the positron, lose their kinetic energies through Coulomb scattering, followed by the positron annihilation. A pair of annihilation photons are produced, which either gets absorbed in the detector or escapes. A single escape peak at energy $(E_\gamma - 0.51)$ MeV and a double escape peak at energy $(E_\gamma - 1.02)$ MeV are produced.

The use of high resolution Hyper Pure Germanium (HPGe) detectors increases the photo-peak efficiency and thus, is ideal for discrete γ-ray spectroscopy. A conventional HPGe detector has a volume of 110 cc and an energy resolution of ~ 2 keV at 1.33 MeV. But the small volume of the detector increases the Compton-escape probability as well as the escape probability of the anihilation photons from the pair-production. This leads to the worsening of the peak to total (P/T) ratio.

68

Increasing the crystal volume is the natural way out to increase the P/T ratio but it is difficult to grow a single HPGe crystal in large size. In addition, a large size of the detector, increases the charge collection time and therefore leads to a lower timing resolution. To overcome these shortcomings, the composite clover detectors are used.

3.3.1   The Clover detector

A clover detector consist of four closely packed hyper-pure n-type germanium crystals in a special arrangement, shown in Fig. 3.1.(a). Each of these crystals are 50 mm in diameter and 70 mm in length [56]. With the clover geometry, 89% of the detector volume remains active, i.e. $\sim$ 470 cc. A common positive high voltage is applied to all the four crystals through an inner contact, while the outer contact surfaces are kept at ground voltage. Two separate outputs from each crystal carries the energy and the timing informations.
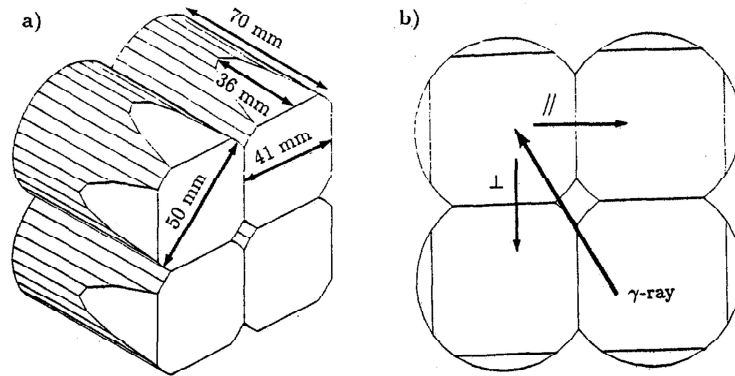
Figure 3.1: a) Typical geometry and size of clover detector, b) Schematic of the horizontal and the Compton scattering of γ-rays in the detector. Figure taken from Ref.[56].

Advantages of clover detector

1. In clover detector, four crystals are electrically isolated and the absence of any material along the length of the crystals ensures that there is no loss in energy when a photon scatters from one crystal to its neighbor. So if a Compton scattered photon from one crystal enters the second crystal and deposits its residual energy, the energy addition from these two crystals leads to a photopeak event. This time correlated addition of energies is called the 'addback mode' and the corresponding spectrum is called the 'addback spectrum'. To obtain a proper addback spectrum, the individual crystal pulses should be gain matched as closely as possible.

2. Individual crystal sizes of the clover detector are small. So a better timing characteristic is obtained for a clover, than a single large HPGe crystal of 470 cc.

3. For the high energy γ-rays ($\gtrsim$ 1MeV), the detection efficiency of a single HPGe crystal is small, as it records the photo-peak as well as the Compton background with same efficiency. On the other hand, a clover detector in addback mode, detects the background with low efficiency but the photo-peak with higher efficiency, as the photo-peak is regenerated by adding smaller energies deposited through two or more Compton scatterings.

4. The clover geometry allow us to use it as a polarimeter. The direction of Compton scattering in the neighboring crystal depends on the linear polarisation state of the γ-rays. Thus, the comparison of Compton events (leading to photopeak) in the reaction plane and out of the reaction plane, can be used to identify the state of polarization for γ-rays.

The anti-Compton shield: The anti-Compton shield of a clover detector, consist of 16 optically isolated Bismuth Germinate (BGO) crystals in a closely packed single casing. A central hole is provided in the casing to accommodate the clover detector. The BGO is a scintillation material with $Z = 83$ for the bismuth. Thus, it has a large photon detection efficiency. In this geometry, the Compton escape photons from the clover detector are absorbed in the BGO detector. The pulse of the clover is taken in anti-coincidence with the BGO pulse. Thus, the clover signal is rejected when a simultaneous pulse is detected in the BGO crystal. This way the Compton background is suppressed.

These arrangements improve the peak to total ratio, but the solid angle subtended by a Compton suppressed clover detector is very small and the photopeak efficiency is $< 1\%$ at 25 cm distance from the target. Thus, a multiple detector set up becomes a necessity. The multi detector setup used for the present work is called the Indian National Gamma Array (INGA) [57, 58].

3.3.2 Indian National Gamma Array

In the INGA setup, the Compton suppressed clover detectors are arranged in a 4π geometry, to cover most of the solid angle. The setup at TIFR (Fig. 3.2) [59], can hold maximum of 24 Compton suppressed clover detectors, arranged as 6 detectors at 90^0 and 3 detectors each at angles 23^0, 40^0, 65^0, 115^0, 140^0 and 157^0 respectively, with respect to the beam direction. The target used in the fusion evaporation reaction, is placed at the center of this array, such that the target to crystal distance is 25 cm [58]. From this, the achieved photopeak efficiency is $\sim 5\%$ at the γ-ray energy of 1 MeV and at a count rate of ~ 20 kHz [58].

On the other hand, the 24 Compton suppressed clover detectors at the INGA

Figure 3.2: The INGA array of Compton suppressed clover detectors set up at TIFR. Figure taken from Ref. [58].

setup of IUAC [57] are arranged as, 8 detectors at 90^0 and 4 detectors each at angles 32^0, 57^0, 123^0 and 148^0 where the target to crystal distance is 24 cm. Here also the achieved photpeak efficiency is $\sim 5\%$.

This setup along with a fast data acquisition system, was used to acquire higher fold coincidence data of in-beam experiments. On the other hand, the multiple angles of the setup was used to measure the angular distribution and Doppler shifts of the γ-rays emitted from the excited nucleus. In the present work, the data from the in-beam experiments were collected using the INGA setup with 18 and 20 Compton suppressed clover detectors at IUAC and TIFR, respectively.

Data sorting: The data acquisition system at TIFR, Mumbai, recorded time-stamped data based on the Pixie-16 modules of XIA LLC [58]. The time-stamped data was sorted into two or higher fold events using the code MARCOS [59], devel-

oped at TIFR, Mumbai.

On the other hand, the data acquisition system at IUAC, Delhi was CAMAC based [57], where TDC's were used to digitize the timing from individual clover crystals and two or higher fold coincidence was used as a master trigger for the data acquisition system. Data sorting was done using the offline sorting codes INGASORT [60] and SPRINGZ [61] developed at IUAC, New Delhi and UGC-DAE Consortium for Scientific Research, Kolkata, respectively.

1. **Energy and efficiency calibration:**

   The detected γ-ray energies are stored as a ADC channel number. The γ-ray energy can be related to the ADC channel number (x) as a power series expansion

   $$E_\gamma = A_0 + A_1 * x + A_2 * x * x$$

   The coefficients A_0, A_1, A_2 are obtained from the time-independent energy calibration using a known radioactive source. The ^{152}Eu and ^{133}Ba sources are routinely used to cover the full energy regime up to 1.4 MeV.

   The energy calibration coefficients were obtained for every crystal of the clover detector. These coefficients might change during the long run period of the experiment. Thus, an online calibration was helpful to track this change. The online calibration was done by noting the ADC channel numbers of few strong photo peaks of the populated nuclei. It may be noted here that the non-linear coefficient (A_2) is generally small ($\sim 10^{-6}$), indicating the linear nature of the ADC's used in the experiments.

   As discussed earlier, the photo peak detection efficiency decreases with increasing energy. The relative intensities of the γ-rays from the calibration

sources were used to estimate the photo peak detection efficiency as a function of energy.

2. **Formation of Cube / Matrix:**

A fusion evaporation reaction populates a number of residual nuclei in their excited states. Thus, it is necessary to collect the data with a time correlation. This way it is possible to assign sequences of γ-transitions to a specific evaporation channel. This time correlated event-by-event data is known as list mode data.

The raw list mode data was first gain matched for every ADC for all the data files collected over the run period. Thus, for a 20 clover set up, 80 ADC's were gain matched. After the gain matching, the ADC channels corresponded to the four crystals of each clover were added. Thus, after the addback, each virtual ADC corresponded to one clover. From this data, the 2-fold or 3-fold coincidence relation between detected γ rays were used to sort the data into a matrix or a cube, respectively. Usually a time window of 200 ns was taken for the determination of a coincidence event. In a matrix, the two ADC values (corresponding to the two coincident γ energies) were stored as the two coordinates (x, y). In general, both these axes stored data in 4096 channels. This $\gamma - \gamma$ matrix was symmetrised so that a γ energy gate could be used only along one axis (generally the x-axis). However, different detector combinations could be constructed to create different angle dependent matrices. A cube on the other hand, stored the γ energies of 3-fold coincidence events as the (x, y, z) coordinates of the cube.

The symmetric $\gamma - \gamma$ matrix along with the cube were used to build a level-

scheme. On the other hand, angle dependent matrices were used for polarisation, angular correlation and level lifetime measurements.

3.4 γ spectroscopy techniques

3.4.1   Building the level-scheme

A level-scheme represents the properties (energy, spin and parity) of multiple excited levels in a nucleus.

Level energy:

The energy of the γ-rays gives the separation energy between the initial and the final level, i.e.

$$E_\gamma = E_i - E_f \qquad (3.5)$$

Sometimes, energy levels with similar characteristics (spin and parity) tend to group together and form a band. To establish band structure, intensity of the coincident γ-energies are measured. For a given band, all the γ-rays are emitted in coincidence. The energy of the first excited state can be found from the energy of the most intense coincident γ. Higher energy levels are then placed with the decreasing order of intensities. For two coincident γ-rays, the intensity is given by [62]

$$I_{\gamma_1\gamma_2} = \frac{A}{\epsilon_{\gamma_1}\epsilon_{\gamma_1}} \qquad (3.6)$$

where, A is the area under the γ_2-peak in coincidence with the γ_1 and ϵ_{γ_1} (ϵ_{γ_2}) is the efficiency for γ_1 (γ_2). Thus, the level energies can be fixed by coincidence intensity measurement of γ rays. A 2-fold symmetric matrix or a 3-fold cube is used for these coincidence measurements using the GTKESC or the GTKLEV programs of the RADWARE packages [63], respectively.

Level spin: the DCO ratio

The spin difference between two levels determines the multipolarity of the connecting γ-ray. Thus, multipolarity measurement of a γ-ray fixes a level spin, if one of the levels spin is already known.

In heavy ion fusion reaction, a compound nucleus is produced in a strongly oriented state. The spin anisotropy is reflected in the angular distribution of the emitted γ-rays. For a γ-ray emitted at an angle, θ, with respect to the beam direction, the angular distribution is given by

$$W(\theta) = \sum_l A_l P_l(cos\theta) \tag{3.7}$$

where, the coefficient A_l is the amplitude for multipole 2^l. These amplitudes are calculated for known multipolarity of the stretched transitions and compared with the fitted values. Thus, an accurate result can be obtained for stretched transitions, but for mixed multipolarity transitions, the angular distribution becomes difficult as the angular coverage is limited in the detector array. However, the difficulty can be resolved by measuring the angular correlation between two coincident γ-rays [64]. With multi detector arrays it is possible to measure the angular correlation between two coincident γ-rays.
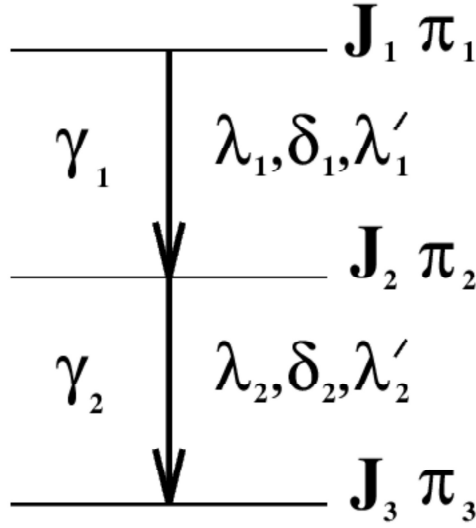
Figure 3.3: The decay scheme of two coincident γ-rays. Figure taken from Ref. [65].

Suppose the nuclear level $[J_1, \pi_1]$ decays to the level $[J_3, \pi_3]$ by emitting γ_1 and γ_2 in sequence (Fig. 3.3). For γ_1, the lowest two orders of multipoles are

$$|J_1 - J_2| \geq \lambda_1, \ \lambda_2 \leq J_1 + J_2$$

where, the mixing ratio between two multipoles are determined by the quantity δ, measured from

$$\delta^2 = \frac{T(\lambda_2)}{T(\lambda_1)}$$

where, T is the transition probability.

The angular correlation between two consecutive γ-rays is defined by the function, $W(\theta_1, \theta_2, \Delta\phi)$, where θ_1 and θ_2 are the emission angles with respect to the beam direction and $\Delta\phi$ is the angle between two planes defined by the beam axis and direction of γ-rays (Fig. 3.4). A unpolarised beam provides

an 180° axial symmetry, which is realised as [65]

$$W(\theta_1, \theta_2, \Delta\phi) = W(180° - \theta_1, 180° - \theta_2, \Delta\phi)$$
$$= W(\theta_1, 180° - \theta_2, \Delta\phi)$$
$$= W(180° - \theta_1, \theta_2, \Delta\phi) \tag{3.8}$$
$$= W(\theta_1, 180° - \theta_2, 180° - \Delta\phi)$$
$$= W(180° - \theta_1, \theta_2, 180° - \Delta\phi)$$

The correlation function $W(\theta_1, \theta_2, \Delta\phi)$, is proportional to the intensity of γ_1 detected at an angle θ_1 when γ_2 is detected at an angle θ_2. The ratio for 'Directional Correlation of γ-rays deexciting Oriented states' (DCO) is defined to get rid of the proportionality function, i.e.

$$R_{dco} = \frac{W(\theta_1, \theta_2, \Delta\phi)}{W(\theta_2, \theta_1, \Delta\phi)}$$
$$= \frac{I_{\gamma\gamma}(\theta_1, \theta_2[\text{gate}])}{I_{\gamma\gamma}(\theta_2, \theta_1[\text{gate}])} \tag{3.9}$$

The sensitivity of the DCO ratio depends on the mixing ratio (δ) and is ~ 1 if both the transitions are pure ($\delta = 0$). To maximise the sensitivity of measurement, one of the angle is chosen close to 90° and the other one close to 0°, with respect to beam direction. For stretched transitions of same multipolarity the ratio is 1.0, and for different multipolarities the ratio is close to 0.5 or 2.0, depending on definition of ratio. For mixed transitions, this ratio increases (decreases) for positive (negative) values of δ.
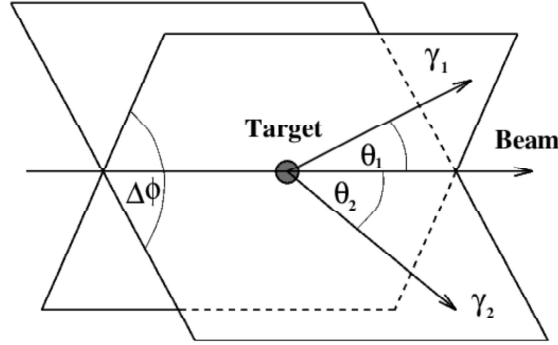
Figure 3.4: The angular correlation scheme for two coincident γ-rays. Figure taken from Ref. [65].

Level parity: the PDCO ratio

For a γ-ray with multipolarity, λ, connecting two levels with parities Π_i and Π_f, respectively

$$
\begin{aligned}
\Pi_i \Pi_f &= (-1)^{\lambda}; \quad \text{Electric type} \\
&= (-1)^{\lambda+1}; \quad \text{Magnetic type}
\end{aligned}
\tag{3.10}
$$

Thus, by measuring γ type (electric or magnetic) we can fix relative parity between two levels. The method of 'Polarization by Directional Correlation of Oriented states' (PDCO) is used to ascertain the electric or magnetic character of the γ-rays.

In a detector, the direction of Compton scattered photon is directly related to its electric or magnetic nature. The four segments of a CLOVER detector (Fig. 3.1(b)) is ideal to measure this asymmetry by measuring the number of Compton scattered photons in the perpendicular or parallel directions. The

PDCO ratio is defined as [66]

$$\Delta = \frac{aN_\perp - N_\parallel}{aN_\perp + N_\parallel} \qquad (3.11)$$

where, $N_\perp(N_\parallel)$ denotes the number of coincident counts between the segment of CLOVER detector in the direction perpendicular (parallel) to the emission plane and 'a' denotes the correction due to the inherent asymmetry of the detector. The value of $a = \left(\frac{N_\parallel}{N_\perp}\right)_{\text{unpolarised}}$, is measured using a unpolarised source of γ-rays, such as radioactive source. The positive or negative values of Δ correspond to the electric or magnetic character of the γ-transitions, respectively.

3.4.2   Level lifetime measurement: DSAM

Importance of lifetime measurements: The partial decay width of a $I_i \to I_f$ gamma transition of energy E_γ and multipolarity λ, is given as [26]

$$\Gamma_{fi}(\lambda) = \frac{8\pi(\lambda+1)}{\lambda((2\lambda+1)!!)^2}\left(\frac{E_\gamma}{\hbar c}\right)^{2\lambda+1} B(\lambda : I_i \to I_f) \qquad (3.12)$$

where, the reduced matrix element $B(\lambda : I_i \to I_f)$, can be calculated using the electromagnetic multipole operator $M(\lambda)$

$$B(\lambda : I_i \to I_f) = \frac{1}{2I_i+1}\langle I_f||M(\lambda)||I_i\rangle^2 \qquad (3.13)$$

The total decay width of the γ-transition is

$$\Gamma = \sum_\lambda \Gamma(\lambda) = \frac{\hbar}{\tau} \qquad (3.14)$$

where, τ is the mean lifetime of the decaying level. The nuclear model wavefunctions can be used to calculate the value of $B(\lambda : I_i \to I_f)$ from Eq. 3.13. On the other hand, the experimentally measured lifetime can be used to calculate the same using Eq. 3.12 and Eq. 3.14. Thus, the level lifetime measurement provides a stringent test for the calculated model wavefunctions.

In a deformed nucleus, the measured quadrupole transition rate, $B(E2)$, in a rotational band is directly proportional to the intrinsic quadrupole moment (Q_0), which in turn can be associated to the quadrupole deformation (β_2) of the band. Therefore, the $B(E2)$ values can be used to identify the Nilsson states involved in the single particle configuration for a rotational band.

On the other hand, the magnetic dipole transition rates, $B(M1)$, are governed by the g-factors of the single particle states near the Fermi surface. Thus, the $B(M1)$ rates also indicate the single particle configuration of a band structure.

Thus, the measurements of the level lifetimes give the important information about the single particle configurations for the bands, which in turn can be linked to the angular momentum generation mechanism in an atomic nucleus.

Doppler Shift Attenuation Method :

The lifetime measurements using the 'Doppler Shift Attenuation Method' (DSAM) is based on the fact that the stopping time of the energetic heavy ions in solid, is comparable with the lifetimes of the nuclear levels which form a band structure. The basic requirement for this method is to use a backed target (Fig. 3.5) in the fusion evaporation reaction. The residual

nuclei stop in the backing material (high-Z), where the slowing down time is typically of the order of 10^{-13} seconds. Thus, this method is useful for the sub-picosecond lifetime measurements which are observed in the high spin bands. If the nucleus is recoiling with a velocity $v(t)$ inside the backing

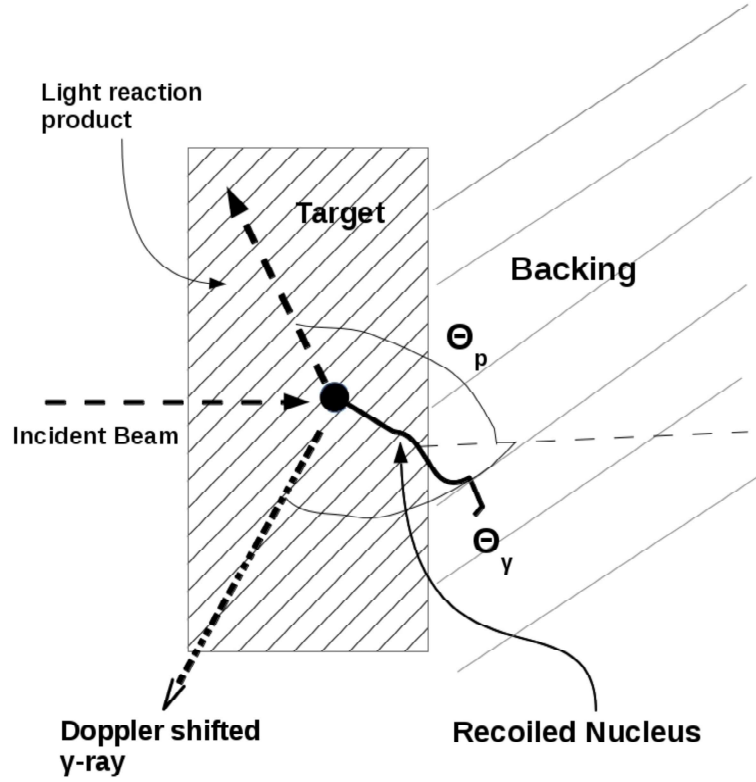Figure 3.5: The schematic representation of the Doppler shift attenuation method (DSAM).

material, the energy of the γ ray, detected at an angle θ can be written as:

$$E(\theta, t) = E_0 \Big(1 + \frac{v(t)}{c} \cos \theta\Big) \tag{3.15}$$

Thus, a lineshape is generated for a mono-energetic γ-ray, if the level lifetime is comparable to the slowing down time of the nucleus. On the other hand,

the γ-ray energy is unshifted if the level lifetime is larger and gives rise to a stopped peak in the lineshape. It is to be noted that, detectors at 90^0 do not exhibit any lineshape, so the 90^0 spectra is useful for estimating the true energy of the γ-rays and identification of any contaminant γ-rays.

The basic scheme of this measurement is to generate theoretical lineshapes using different lifetime values, which are then compared with the observed lineshape and the χ^2-minimisation technique is used to estimate the best value. The theoretical lineshape is obtained by calculating the number, $\frac{dN(V)}{dV}$, which measures the number of nuclei that decay between the velocity range $V(t)$ and $V(t) - dV$. This also gives the number of nuclei that decay between the time t and $t + dt$, i. e. the decay rate can be written as

$$\frac{dN(t)}{dt} = \left(\frac{dN(V)}{dV}\right)\left(\frac{dV(t)}{dt}\right) \tag{3.16}$$

For a two level system where the level 2 is directly fed by the transition from level 1, the decay rate formula is given by

$$\frac{dN_2(t)}{dt} = -\left[\frac{N_1^0}{\tau_2 - \tau_1}\left(e^{-t/\tau_1} - e^{-t/\tau_1}\right)\right] \tag{3.17}$$

where, N_1^0 (N_2^0) and τ_1 (τ_2) are the population and lifetime of the level 1 (level 2) respectively,

Thus, the theoretical lineshape, $\left(\frac{dN(V)}{dV}\right)$, can be generated from Eq. 3.16 and Eq. 3.17. In this calculation, the value of $\frac{dV(t)}{dt}$ is obtained by simulating the energy loss of the nuclei inside the target as well as the backing, i.e.

$$\frac{dV(t)}{dt} = -\frac{1}{m}\frac{dE}{dx} \tag{3.18}$$

where, m is the mass of the recoiling nuclei. The energy loss $\left(\frac{dE}{dx}\right)$ of the recoiling nuclei is mainly governed by the two slowing down processes, which are :

(a) **Electronic stopping:** In this process, the electrons of the recoiling nucleus interacts with that of the stopping material via Coulomb interaction. This process dominates for $\beta \gtrsim 2\%$

(b) **Nuclear stopping:** The nuclear stopping dominates for $\beta \lesssim 0.5\%$ and the recoiling nucleus interacts with the atomic nucleus of the stopping material.

Thus,

$$\frac{dE}{dx} = \left(\frac{dE}{dx}\right)_{\text{electronic}} + \left(\frac{dE}{dx}\right)_{\text{nuclear}} \tag{3.19}$$

The code DECHIST_OR calculate this energy loss using any of these three options [26]:

(a) Ward's effective charge and Ziegler's proton stopping power

(b) Ziegler's heavy-ion stopping power

(c) Shell-corrected Northcliff and Schilling stopping powers

The program DECHIST_OR [68] generates a velocity profile, where the magnitude and direction of the velocity is calculated at fixed time intervals during the slowing-down process of the recoiling nuclei. From this, a time dependent velocity profile as seen by the detector, is created by using the code HISTAVER_OR [68]. Typically, a velocity profile contains 5000 events simulated at a time step of 0.001 ps.

In the final step, the LINESHAPE [68] code is used for lifetime estimation. This program can simultaneously fit multiple lineshapes in a γ-cascade. In a band, the lifetime measurement starts by fitting the lineshape of the topmost transition, where the side-feeding intensity is assumed as 100%. The lifetime obtained for this level is called the 'effective lifetime', which is kept fixed while the line shapes for the lower lying transitions in the band are fitted globally by varying the transition quadrupole moment, the top and the side feeding quadrupole moments. The other parameters such as the background, the intensity, the energy of the γ ray transition and the FWHM are assumed as input parameters. For a given set of parameters, the experimentally observed line shapes are fitted using the χ^2-minimisation routines of MINUIT [67]. The angle dependent asymmetric matrices are used to extract the lineshapes at different angles. The 90° spectra is also fitted simultaneously to identify the peak positions of the desired transition as well as the contaminant transitions, if any. It is to be noted that the spectra at 90°, have a Doppler broadening effect due to finite size of the detector. This broadening is also accounted by the code LINESHAPE.

In case a level is fed by two γ transitions, the two top level feeds is taken into account through the intensity weighted average of the half-lives of the feeding levels which is considered as the top feeding lifetime for the fitting transition.

The uncertainties in the lifetime measurements are derived from the χ^2 behavior in the vicinity of the minimum for the simultaneous fit at all the angles. The other sources of uncertainties in the level lifetime measurement are due to the variation in the side-feeding intensity and the side-feeding
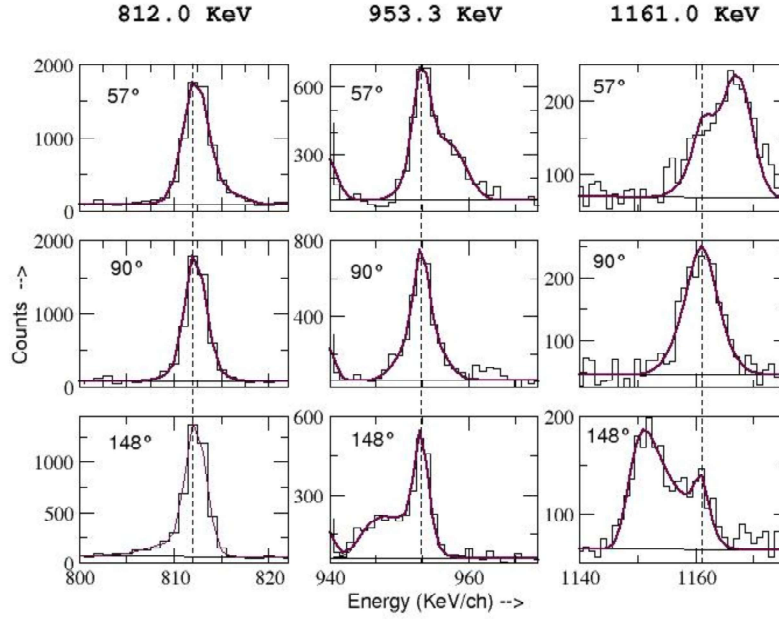
Figure 3.6: Examples of the lineshape fits for the transitions in ^{110}Cd nucleus.

lifetime. These errors are estimated by finding the level lifetimes for the extremum values of the side-feeding intensities and the side-feeding quadrupole moments. The final statistical uncertainty is calculated by adding in quadrature the uncertainties due to the line-shape fitting, the side-feeding intensity and the side-feeding quadrupole moment. However, this estimated error does not include the systematic uncertainty that arises due to the choice of the stopping powers. This uncertainty increases from 8% at low spins to 28% for the topmost level [10].

The lineshape analysis has been used extensively during the course of this thesis work. The fitted lineshapes of few high-spin transitions of the ^{110}Cd nucleus have been shown in Fig. 3.6.

4

Interplay between core rotation and shears mechanism in ^{106}Ag

4.1 Introduction

The yrast partner bands of ^{106}Ag has already been studied and it was found that they are not chiral partners [6, 69, 70]. Their origin may be attributed to the γ-softness of ^{106}Ag [69]. In the present work, the structures of the non-yrast bands of ^{106}Ag has been explored.

4.2 Experiment

The high spin states of ^{106}Ag was populated using the 68 MeV ^{14}N beam from the 14-UD Pelletron at TIFR through ^{96}Zr(^{14}N, 4n) reaction. The 1 mg/cm^2 thick enriched ^{96}Zr target was used which had a ^{206}Pb backing of 9

mg/cm^2. The γ rays were detected in the INGA setup of TIFR [58, 59], which consisted of 20 Compton suppressed clover detectors. These were arranged at seven angles with four detectors at 90°, three each at 40°, 65°, 140° and 157° and two each at 23°, 115° with respect to the beam direction [7]. The target to detector distance was 25 cm. The data acquisition system used in this experiment along with the data sorting techniques have been discussed in Chap.3.

4.3 Analysis and results

4.3.1 Level scheme

The γ-ray energies and their relative intensities were primarily determined by analyzing the symmetric $\gamma - \gamma$ matrix and the $\gamma - \gamma - \gamma$ cube using the RADWARE programs GTKESC and GTKLEV [63], respectively. However, the cube and the symmetric matrix were not suitable for extracting the intensities of γ rays de-exciting the levels having sub pico second lifetimes as they exhibit Doppler broadened line shapes. The relative intensities of these γ rays were obtained from the 90°-vs-all matrix, which were normalized with the intensities of the transitions of the same multipolarity estimated from the cube. The multipolarities of the γ rays were determined by the DCO ratio method. The linear polarization measurements were also performed to extract the electromagnetic character of the de-exciting γ rays. These techniques have been described in detail in chapter 3.
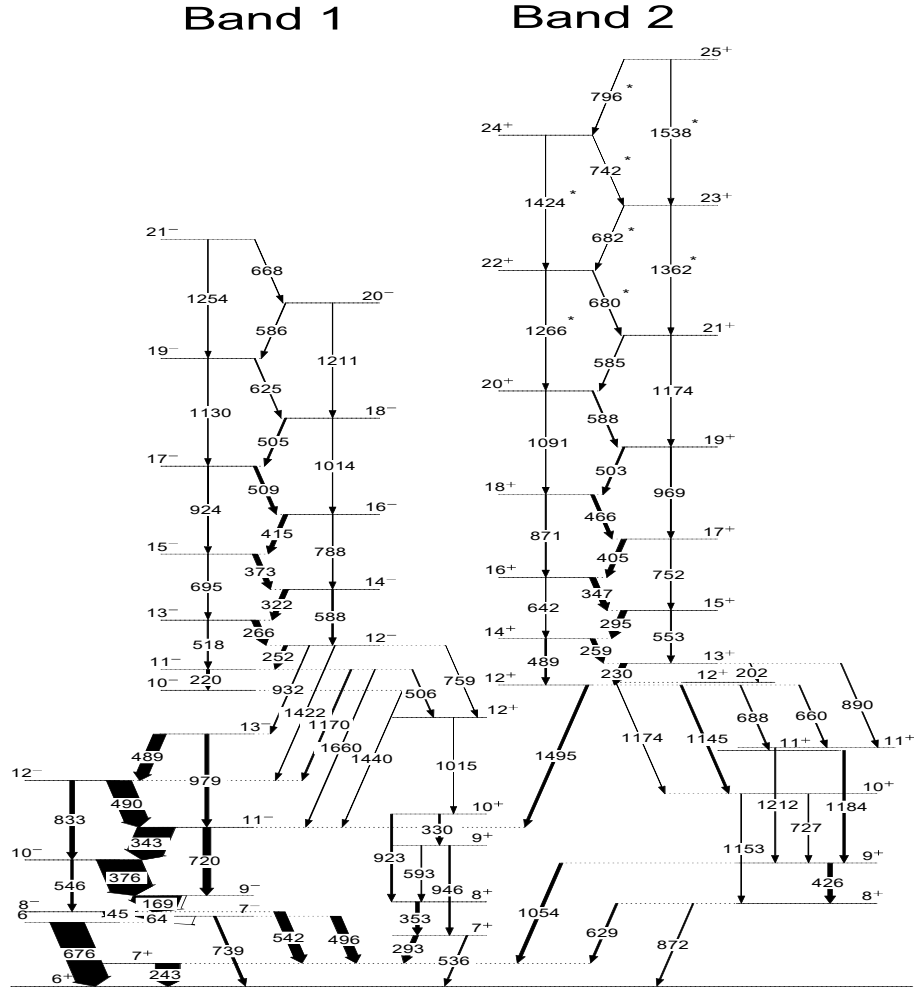
Figure 4.1: The partial level scheme of ^{106}Ag.

Band 1

The negative parity band was first reported by Jerestam *et al.* [71] and was extended up to $I = 15\hbar$. The feed out paths of the band was very limited and the placement of $M1$ transitions were also not in proper order. Then it was revisited by Lieder *et al.* [6] and a complete band structure was reported. In the present work, a completely independent analysis was carried out which agrees well with the published results of Ref. [6]. A sum gated spectra of

	Band 1			Band 2	
E_γ(keV)	$I_i^\pi \to I_f^\pi$	Rel. Int.	E_γ(keV)	$I_i^\pi \to I_f^\pi$	Rel. Int.
252	$12^- \to 11^-$	8.4(5)	230	$13^+ \to 12^+$	12.8(5)
266	$13^- \to 12^-$	14.5(5)	259	$14^+ \to 13^+$	16.3(5)
322	$14^- \to 13^-$	11.5(3)	295	$15^+ \to 14^+$	13.7(3)
373	$15^- \to 14^-$	11.1(4)	347	$16^+ \to 15^+$	12.3(4)
415	$16^- \to 15^-$	9.6(3)	405	$17^+ \to 16^+$	10.9(3)
505	$17^- \to 16^-$	4.0(5)	466	$18^+ \to 17^+$	8.6(4)
509	$17^- \to 16^-$	7.2(4)	466	$18^+ \to 17^+$	8.6(4)
518	$13^- \to 11^-$	3.0(3)	489	$14^+ \to 12^+$	3.7(8)
586	$20^- \to 19^-$	1.7(4)	503	$19^+ \to 18^+$	8.4(3)
588	$14^- \to 12^-$	3.2(3)	553	$15^+ \to 13^+$	.5(5)
625	$19^- \to 18^-$	2.3(3)	585	$21^+ \to 20^+$	3.6(4)
668	$21^- \to 20^-$	1.0(3)	588	$20^+ \to 19^+$	3.9(4)
695	$15^- \to 13^-$	1.0(1)	642	$16^+ \to 14^+$	1.9(3)
788	$16^- \to 14^-$	1.8(2)	680	$22^+ \to 21^+$	2.6(3)
924	$17^- \to 15^-$	2(2)	682	$23^+ \to 22^+$	1.6(3)
1014	$18^- \to 16^-$	1.2(2)	688	$12^+ \to 11^+$	2.8(4)
1130	$19^- \to 17^-$	0.8(2)	742	$24^+ \to 23^+$	1.0(3)
1211	$20^- \to 18^-$	1.3(3)	752	$17^+ \to 15^+$	2.1(3)
1254	$21^- \to 19^-$	0.5(3)	796	$25^+ \to 24^+$	0.6(1)
			871	$18^+ \to 16^+$	3.9(3)
			969	$19^+ \to 17^+$	3.4(3)
			1091	$20^+ \to 18^+$	3.2(4)
			1174	$21^+ \to 19^+$	3.4(4)
			1266	$22^+ \to 20^+$	1.8(3)
			1362	$23^+ \to 21^+$	1.8(4)
			1424	$24^+ \to 22^+$	1.5(2)
			1538	$25^+ \to 23^+$	1.9(2)

Table 4.1: The energies and the relative intensities for the in band γ transitions of ^{110}Ag. The relative intensities were scaled by considering the intensity of 169 $(9^- \to 8^-)$ keV transition as 100.

252 keV $(12^- \to 11^-)$ and 266 keV $(13^- \to 12^-)$ transitions at 90° angle is shown in Fig. 4.2, where all the transitions belonging to the band 1 can be seen. The spin and parity of the band were assigned by Lieder *et al.* [6], from which the bandhead can be fixed at $I^\pi = 10^-$.

Band 2

The positive parity band of ^{106}Ag was first reported by Jerrestam *et al.* [71] and was revisited by He *et al.* [72].
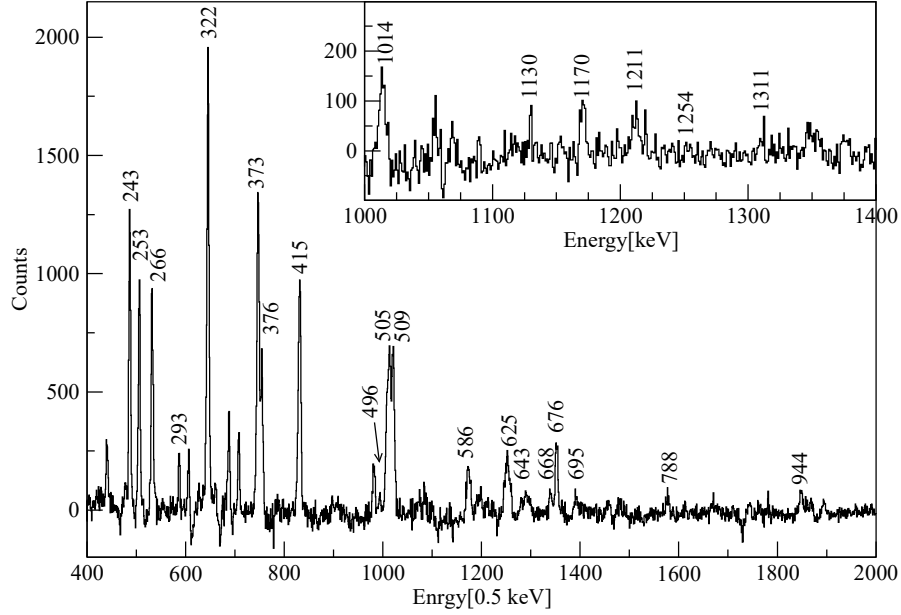
Figure 4.2: Sum gated spectra of 252 ($12^- \rightarrow 11^-$) and 266 ($13^- \rightarrow 12^-$) keV transitions showing γ transitions belonging to the negative parity band of ^{106}Ag nucleus. The observed high energy transitions have been magnified in the inset.

The sum gate of 258 and 295 keV in Fig. 4.4, shows the γ rays belonging to this positive parity band of ^{106}Ag, where the newly placed transitions are marked with '∗ '. The effect of the Doppler broadening at 90° is clearly visible in the inset of the Fig. 4.4 for 1266, 1362, 1424 and 1538 keV transitions whereas, this effect is negligible in the case of 1495 keV transition, since it is a retarded E1 transition. This observation is consistent with the present level scheme and confirms the same reported by C. Y. He *et al.* [72] till $I^\pi = 21^+$ except few changes. The previously placed 1212 keV transition between $22^+ \rightarrow 20^+$ is found to be inconsistent as it does not exhibit Doppler broadening but the immediately lower E2 transition, namely 1091 keV ($20^+ \rightarrow 18^+$), is Doppler broadened. In addition, the 628 keV
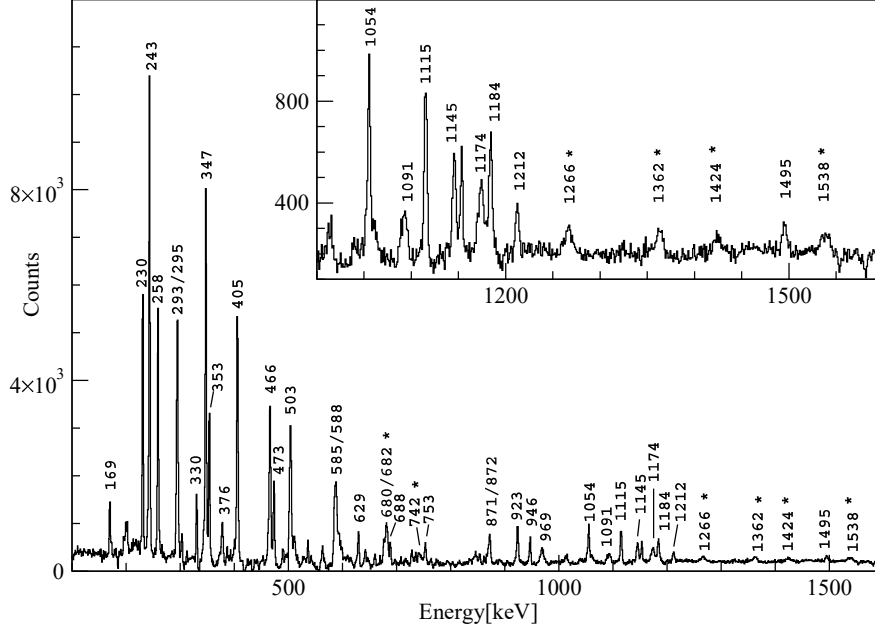
Figure 4.3: Sum gated spectra of 258 ($14^+ \rightarrow 13^+$) and 295 ($15^+ \rightarrow 14^+$) keV transitions showing γ transitions belonging to the positive parity band of ^{106}Ag nucleus. The observed high energy transitions have been magnified in the inset.

($22^+ \rightarrow 21^+$) transition is not present in the sum gate of 1495 ($12^+ \rightarrow 11^-$) and 1145 ($12^+ \rightarrow 10^+$) keV transitions, but two new transitions of 680 and 682 keV are clearly visible. The sum gated spectra of 1495 and 1115 keV is shown in Fig. 4.4. These two transitions have been placed in the present level scheme as the $22^+ \rightarrow 21^+$ and the $23^+ \rightarrow 22^+$ transitions. This placement is further supported by the presence of the two cross over E2 transitions, 1266 ($22^+ \rightarrow 20^+$) and 1362 ($23^+ \rightarrow 21^+$), which exhibit the expected Doppler broadening. The level scheme has been further extended to 25^+ level through the placement of two more M1 transitions (742 and 796 keV) and the corresponding cross over E2 transitions (1424 and 1538 keV). In the present
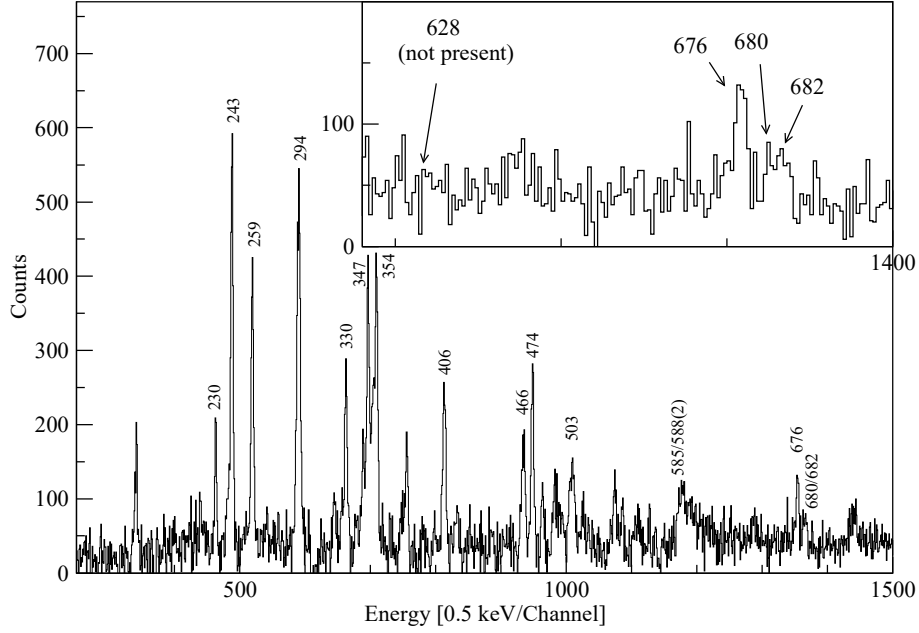
Figure 4.4: Sum gated spectra of 1495 ($12^+ \rightarrow 11^-$) and 1115 ($12^+ \rightarrow 10^+$) keV transitions showing γ transitions belonging to the positive parity band of ^{106}Ag nucleus. The unobserved transition of 628 keV is pointed in the inset.

level scheme (Fig. 4.1), the 629 and the 1212 keV transitions de-excite the lower spin states of 8^+ and 11^+, respectively. It is consistent with the gated spectrum shown in Fig. 4.4. At the lower spin domain, an additional 12^+ level was identified which de-excites to the 10^+ level through a 1015 keV $E2$ transition. It may be noted that the previously reported [72] $E1$ transition of 1238 keV ($13^+ \rightarrow 12^-$) connecting the negative parity state could not be confirmed in the present analysis. The spins and parities of the states were firmly established through the DCO and the PDCO measurements of the 1495 ($12^+ \rightarrow 11^-$) and the 1145 keV ($12^+ \rightarrow 10^+$) transitions. The values are 0.48(17) and 0.21(13) for 1495 keV and 1.11(15) and 0.35(11) for 1145 keV γ

rays, respectively [10].

4.3.2   Lifetime measurement : DSAM

In order to extract the transition rates ($B(M1)$ and $B(E2)$), the level lifetime measurements were carried out for both the bands. As mentioned earlier the high spin states of ^{106}Ag were populated in a backed target, so the level lifetime measurement was carried out using 'Doppler shift attenuation method'. The lifetimes were measured by fitting the experimental line shapes at the forward and the backward angles simultaneously with the theoretical line shapes derived from the code LINESHAPE by Wells and Johnson [68]. The details of LINESHAPE analysis has been discussed in Chap.3.

Band 1

For the level lifetime measurements of band 1, the experimental line shapes were extracted from the sum gate of 252, 266 and 518 keV transitions, and the line shape fitting at three angles namely 40°, 90° and 157°, was carried out simultaneously. The two cascades of the cross over $\Delta I = 2$ transitions of this band were fitted separately.

   For the even spin-states cascade, the effective lifetimes for the 20^- and the 21^- levels were found by fitting the line shapes of the corresponding de-exciting $E2$-transitions of 1211 and 1254 keV, respectively by assuming 100% side-feed. The top feed lifetime for 18^- level was estimated from the intensity weighted average of the lifetimes for 20^- and 19^- levels since this level is fed

416 keV   **1014 keV**
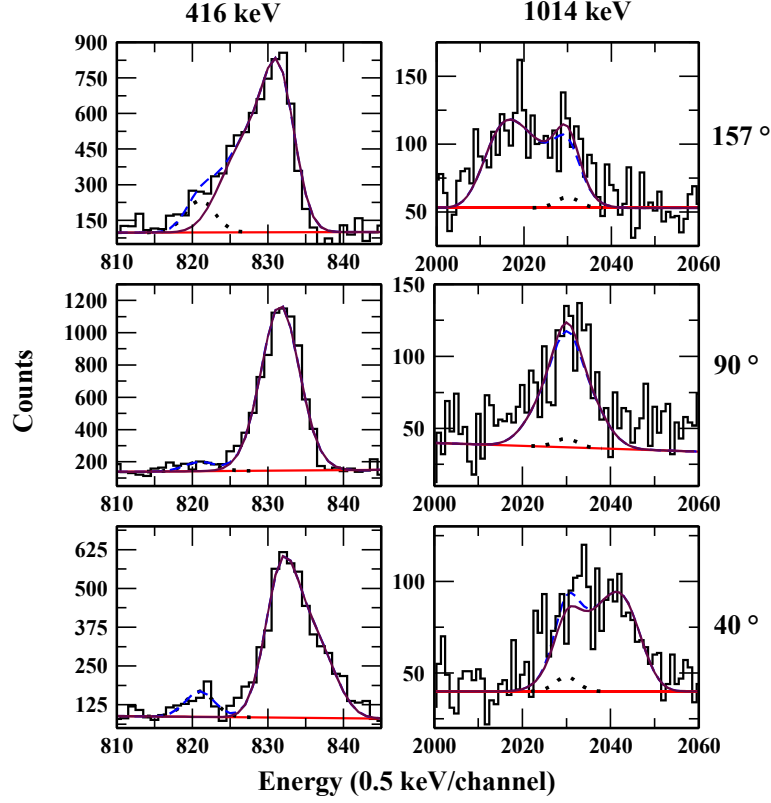
Figure 4.5: Examples of the line shape fits for 416 ($16^- \rightarrow 15^-$) keV and 1014 ($18^- \rightarrow 16^-$) keV transitions at 40°, 90° and 157° with respect to the beam direction. The Doppler broadened line shapes are drawn in solid lines while the contaminant peaks are shown in dotted lines. The result of the fit to the experimental data is shown in dashed lines.

by both 625 ($19^- \rightarrow 18^-$) keV $M1$ and 1211 ($20^- \rightarrow 18^-$) keV cross over $E2$ γ rays. The side feeding intensity at this level was fixed to reproduce the observed intensity pattern at 90° with respect to the beam direction. In this way, each lower level was added one by one and fitted until the observed line shapes for 1014 ($18^- \rightarrow 16^-$) and 788 ($16^- \rightarrow 14^-$) keV γ rays were included into a global fit as described before. The other cascade of $\Delta I = 2$ transitions of 1130 ($19^- \rightarrow 17^-$), 924 ($17^- \rightarrow 15^-$) and 695 ($15^- \rightarrow 13^-$) keV, were

fitted in similar way.

In these angle dependent sum gated spectra, there is a weak contamination of 1015 keV transition ($12^+ \rightarrow 10^+$) in the 1014 keV line shape (shown in Fig. 4.5). However it is interesting to note that the 1015 keV transition should not exhibit any line shape since it is only fed by E1 transitions which are expected to have lifetime of more than a picosecond. This was ascertained from the 509 keV gate from which the intensity of the contaminant stopped peak of 1015 keV was estimated.

The line shapes of the $\Delta I = 1$ γ-ray sequence was also fitted following the same prescription. The examples of the lineshape fits are shown in Fig. 4.5 for the 416 keV and 1014 keV gamma transitions. Lieder *et al.* [6] did not mention the uncertainties while quoting the level lifetimes and hence, the two results can not be compared critically. However, the values are in the similar range.

Band 2

For band 2, the level lifetimes of the high spin states beyond $I = 16\hbar$ were measured. These line shapes were extracted at the specific angles by using the sum gates of 230 and 258 keV transitions on the angle specific matrices. The lifetimes of 25^+ and 24^+ levels were considered to be effective and then the lower level lifetimes were measured using the cascade fit method. The energy levels below $I = 24\hbar$ were fed by two top γ transitions. So a intensity weighted average of the half-lives of the feeding levels was considered as the top feeding lifetime for the fitting transition. The line shapes of both the $E2$ and the $M1$ transitions were fitted to extract the level lifetimes of the
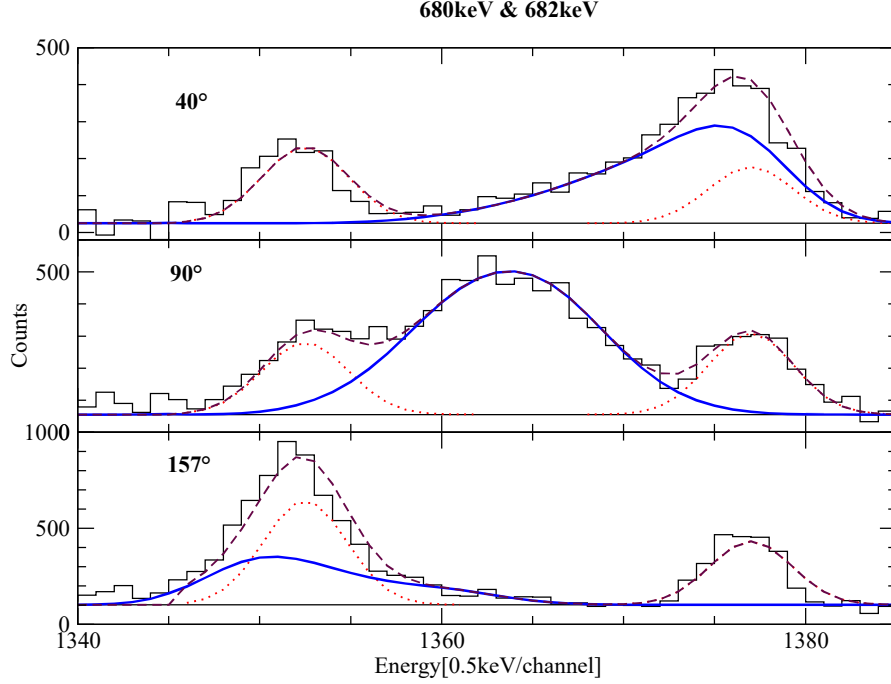
680keV & 682keV

Figure 4.6: Examples of the composite line shape fits for 680 ($22^+ \rightarrow 21^+$) and 682 ($23^+ \rightarrow 22^+$) keV transitions at 40°, 90° and 157° with respect to the beam direction. The calculated line shapes are shown as solid lines and the contaminant peaks are shown as dotted lines.

levels with $I < 20\hbar$. The top four M1 transitions namely 682 ($23^+ \rightarrow 22^+$), 680 ($22^+ \rightarrow 21^+$), 585 ($21^+ \rightarrow 20^+$) and 588 ($20^+ \rightarrow 19^+$) keV, form two composite line shapes and could not be fitted by the standard prescription. However, these composite line shapes have been used to cross check the level lifetimes which were extracted by fitting the corresponding E2 transitions. This was performed by fixing lifetime of one of the levels to the extracted value (e.g. $\tau_{I=23\hbar} = 0.12$ ps) and vary the lifetime of the other ($I = 22\hbar$) to fit the composite line shape and vice versa. The composite lineshapes of 680 ($22^+ \rightarrow 21^+$) and 682 ($23^+ \rightarrow 22^+$) keV transitions is shown in Fig. 4.6 and the composite lineshapes of 585 ($21^+ \rightarrow 20^+$) and 588 ($20^+ \rightarrow 19^+$) keV
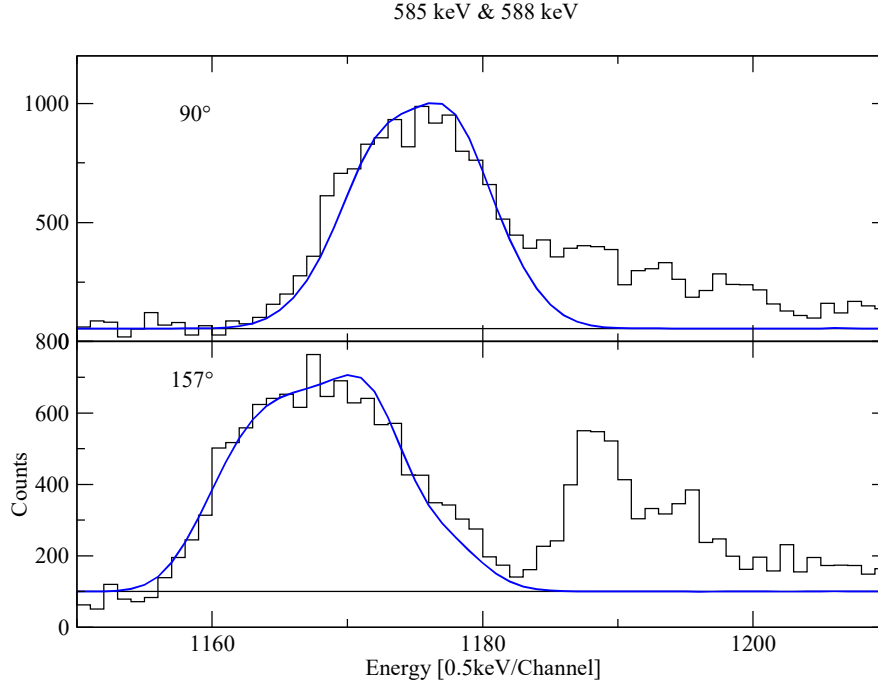
585 keV & 588 keV

Figure 4.7: Examples of the composite line shape fits for 585 ($21^+ \rightarrow 20^+$) and 588 ($20^+ \rightarrow 19^+$) keV transitions at 90° and 157° with respect to the beam direction. The calculated line shapes are shown as solid lines and the contaminant peaks are shown as dotted lines.

transitions is shown in Fig. 4.7. It is to be noted that, for the second case, the composite lineshape at 40° could not be fitted because it is contaminated due to the presence of Ge(n, $n'\gamma$) reaction. The other fitting parameters for the levels like side feeding intensities and quadrupole moments were kept fixed to the values used to fit the corresponding line shapes of the E2 transitions. The four level lifetimes obtained by this procedure agree within $\pm\, 1\sigma$ with those found by fitting the E2 transition line shapes. This exercise adds to the significance of the reported level lifetimes for $I > 19\hbar$. In order to further crosscheck the consistency of the level lifetime measurements, the line shapes of the 466 ($18^+ \rightarrow 17^+$) and 405 ($17^+ \rightarrow 16^+$) keV transitions were extracted
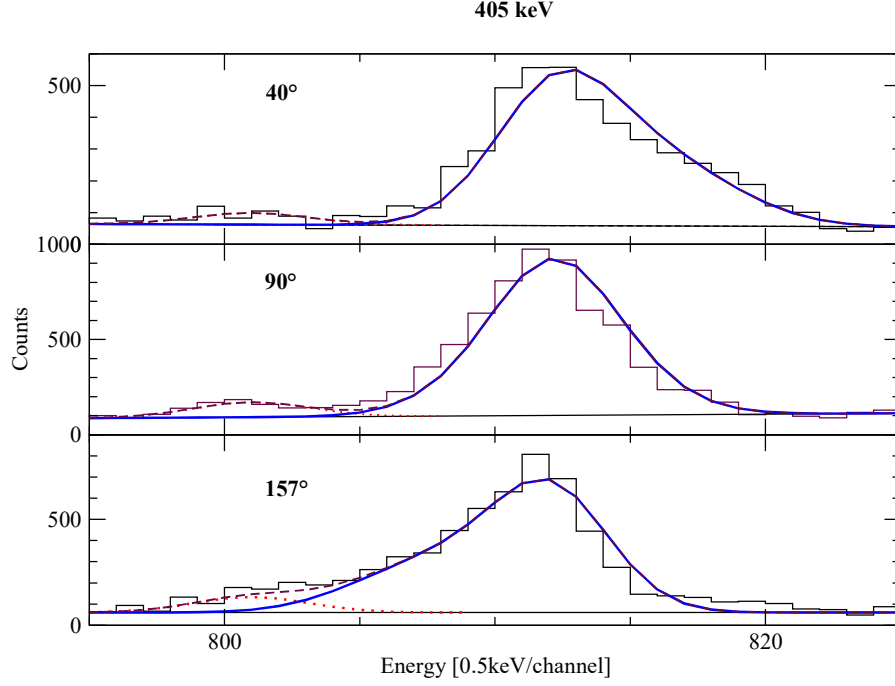
Figure 4.8: Examples of the top gated line shape fit for 405 ($17^+ \rightarrow 16^+$) keV transition at 40°, 90° and 157° with respect to the beam direction. The calculated line shapes are shown as solid lines and the contaminant peaks are shown as dotted lines.

from top gating. The lineshape of 405 keV transition from top gating is shown in Fig 4.8. In these cases, the observed line shapes were fitted by taking into account the complete top cascade but no side feeding at the level of interest. The results from the top and bottom gates were found to agree within $\pm 1\sigma$. The example of lineshape fits to bottom gated spectra of band 2 is shown in Fig. 4.9. In an earlier work by Deo *et al.*, [73] the lifetimes of the $I = 16\hbar$ to $18\hbar$ levels (spin adjusted in accordance to the later publications) were measured using line shape analysis with an effective lifetime of 0.31(3) ps for the $I = 19\hbar$ level. The reported values for the $I = 18\hbar$ and $17\hbar$ levels were 0.34(1) and 0.52(2) ps respectively. These values are in clear disagreement
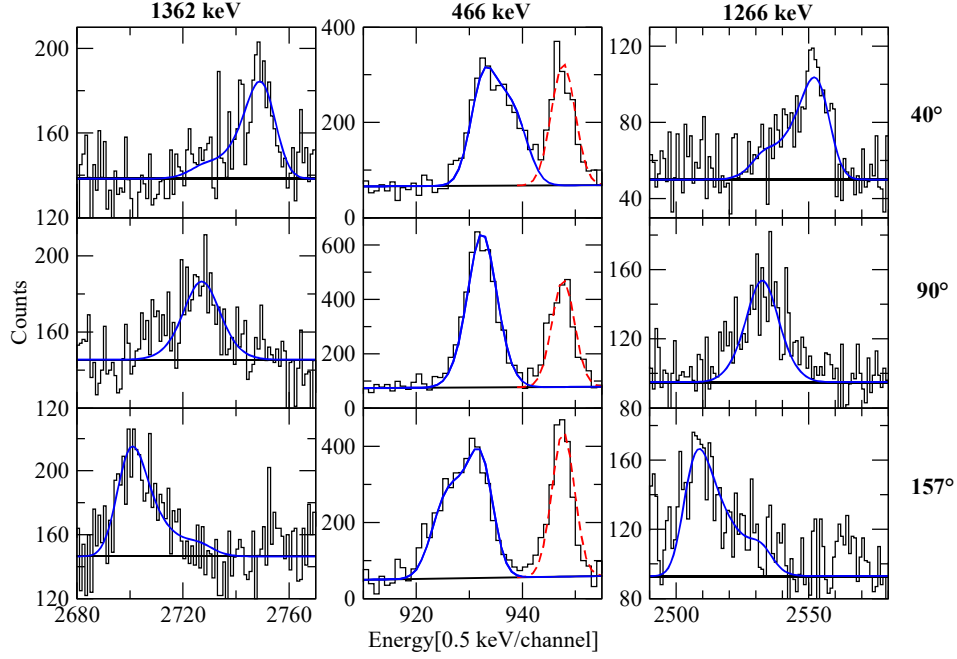
Figure 4.9: Examples of line shape fits for 1362 ($23^+ \rightarrow 21^+$), 466 ($18^+ \rightarrow 17^+$) and 1266 ($22^+ \rightarrow 20^+$) keV transitions at 40°, 90° and 157° with respect to the beam direction. The calculated line shapes are shown as solid lines and the contaminant peaks are shown as dashed lines.

with the present measurement. In order to investigate this discrepancy, the observed lineshapes from the present work for 466 ($18^+ \rightarrow 17^+$) and 405 ($17^+ \rightarrow 16^+$) keV transitions were fitted by assuming an effective lifetime of 0.31(3) ps for the $I = 19\hbar$ level. In this case the extracted lifetimes for the $I = 17\hbar$ and $18\hbar$ levels agreed well with the reported values by Deo *et al* [73]. Conversely, the line shape for 503 ($19^+ \rightarrow 18^+$) keV transition was fitted with a single level formula and the effective lifetime extracted from the present data was 0.51 ps. The lifetime values for $I = 17\hbar$ and $18\hbar$ extracted with this effective lifetime were found to agree with the results quoted in Tab. 4.2. Thus, it may be concluded that the discrepancy arouse due to an

Chapter 4. Interplay between core rotation and shears mechanism in ^{106}Ag

erroneous estimation of the effective lifetime for the $I = 19\hbar$ level by Deo *et al.* [73].

4.3.3 Transition rates

With the calculated values of level lifetime, the $B(M1)$ and the $B(E2)$ transition rates have been extracted. The $B(M1)$ values can be extracted using

Spin	Lifetime	Mixing Ratio	Br. Ratio	$B(M1)$	$B(E2)$
	±Stat. ±Sys.	±Stat.	±Stat.	±Stat. ±Sys.	±Stat. ±Sys.
$[\hbar]$	[ps]	$[\delta]$	$[B_r]$	$[\mu_N^2]$	$[e^2b^2]$
	Band 1				
14^-	0.41 ±0.03 ± 0.04	0.11 ±0.05	0.88 ±0.05	3.60±0.34 ± 0.36	0.34±0.03 ±0.04
15^-	0.40 ±0.03 ± 0.04	0.13 ±0.05	0.81 ±0.05	2.18±0.22 ± 0.21	0.24±0.02 ±0.04
16^-	0.35 ±0.04 ± 0.03	0.19 ±0.06	0.75 ±0.07	1.64±0.24 ± 0.21	0.19±0.03 ±0.03
17^-	0.34 ±0.05 ± 0.04	0.21 ±0.05	0.69 ±0.09	0.83±0.17 ± 0.14	0.11±0.02 ±0.02
18^-	0.18 ±0.04 ± 0.04	0.18 ±0.06	0.65 ±0.10	1.55±0.42 ± 0.42	0.15±0.04 ±0.03
19^-	0.14 ±0.04 ± 0.03	0.23 ±0.06	0.56 ±0.11	0.88±0.31 ± 0.29	0.14±0.05 ±0.04
20^-	0.17	0.19 ±0.06	0.52 ±0.14	0.83	0.09
	Band 2				
17^+	0.33 ±0.04 ±0.03	0.15 ±0.04	0.80 ±0.05	2.03 ±0.30 ±0.20	0.21 ±0.03 ±0.02
18^+	0.21 ±0.02 ±0.02	0.18 ±0.05	0.76 ±0.05	1.97 ±0.23 ±0.23	0.19 ±0.02 ±0.02
19^+	0.18 ±0.02 ±0.01	0.19 ±0.06	0.71 ±0.08	1.74 ±0.28 ±0.22	0.16 ±0.03 ±0.02
20^+	0.15 ±0.03 ±0.02	0.24 ±0.07	0.55 ±0.07	0.97 ±0.23 ±0.18	0.15 ±0.04 ±0.03
21^+	0.22 ±0.03 ±0.03	0.21 ±0.07	0.52 ±0.06	0.64 ±0.12 ±0.11	0.08 ±0.02 ±0.01
22^+	0.14 ±0.03 ±0.02	0.18 ±0.07	0.58 ±0.08	0.72 ±0.18 ±0.14	0.07 ±0.02 ±0.01
23^+	0.12 ±0.02 ±0.02	0.15 ±0.04	0.48 ±0.08	0.70 ±0.17 ±0.16	0.08 ±0.02 ±0.02
24^+	0.11	0.15 ±0.04	0.41 ±0.08	0.50	0.07

Table 4.2: The measured lifetimes, the E2/M1 mixing ratios, the branching ratios and the corresponding $B(M1)$ and $B(E2)$ values for band 1 and band 2 of ^{106}Ag. The statistical errors as well as the systematic errors in lifetime measurement are tabulated.

the following relation:

$$B(M1) = 5.68 \times 10^{-14} \times E_\gamma^{-3} \times B_r \times \frac{1}{\tau \times (1 + \delta^2)} \qquad (4.1)$$

where B_r is the $B(M1)$ branching ratio, τ is the half life time in second, δ is the mixing ratio and the γ-ray energy (E_γ) is expressed in MeV. In case of $M1$ transitions a sufficient amount of $E2$ mixing is possible, thus evaluation of mixing ratios (δ) was done using the measured DCO values assuming the width of the sub-state population, σ/j to be 0.3 [70].

The $B(E2)$ values has been extracted using the relation:

$$B(E2) = 8.156 \times 10^{-14} \times E_\gamma^{-5} \times \frac{(1 - B_r)}{\tau}. \tag{4.2}$$

The calculated transition rates has been tabulated in Tab. 4.2.

4.4 Discussion

4.4.1 Band 1

It is apparent from Tab. 4.2 that the $B(M1)$ rates fall rapidly between the spin range of $14\hbar$ to $17\hbar$ from the value 3.60 (34) μ_N^2 to 0.83 (17) μ_N^2. However, at $I = 18\hbar$, the $B(M1)$ value increases significantly to 1.55 (42) μ_N^2 and follow a similar but slower falling trend as a function of spin. This trend was also reported by Lieder *et al.* [6]. A similar discontinuity in $B(M1)$ values as a function of spin was reported in the neighboring even-even nucleus ^{108}Cd [74], and was associated to the crossing between the two shears bands originating from the six and the eight valence particle configurations. Thus, it is possible that a crossing between the shears band is occurring in ^{106}Ag nucleus. As can be seen in Fig. 4.10, there is not much alignment gain during

the band crossing, however it is possible a weak band mixing takes place in the region of $I = 18\hbar$.

The behavior of the routhian as well as the transition rates were described in the framework of the SPAC model [9] by assuming a band-crossing at $I = 18\hbar$. For the SPAC calculations, it is essential to fix the quasi particle configuration of the band. It may be noted that the value for the quasi particle alignment for band 1 of ^{106}Ag is substantially higher than that for the yrast band, as can be seen in Fig. 4.10. The two quasi particle configuration of the yrast
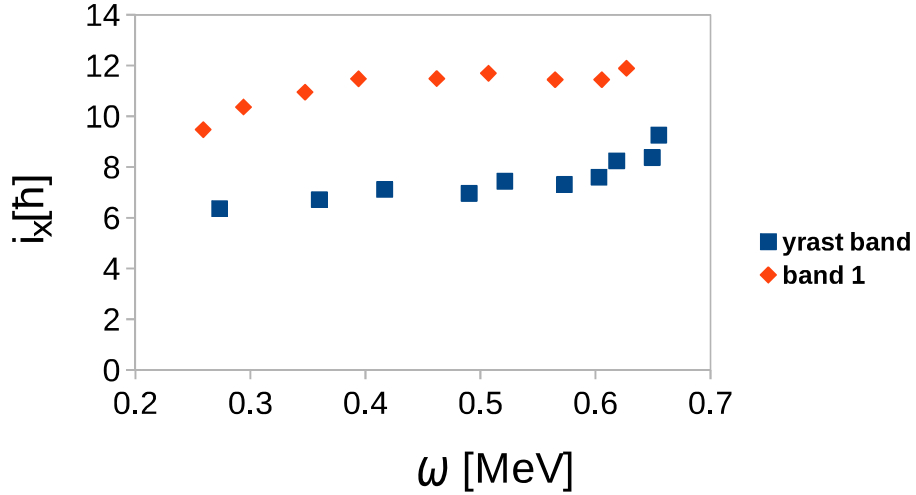
Figure 4.10: The quasi particle alignment(i_x) as a function of the rotational frequency (ω). The Harris parameters used are $\mathfrak{I}_0 = 8.9 \ \hbar^2/\text{MeV}$ and $\mathfrak{I}_2 = 15.7\hbar^4/\text{MeV}^3$ [6].

band is $\pi g_{9/2}^{-1} \otimes \nu h_{11/2}$ [6]. In addition, the band head energy of the band 1 is ~ 2 MeV higher than the yrast band. These observations indicate that the band 1 originates from a four quasi particle configuration. There are three possible four quasi particle configurations with negative parity for band 1,

namely $\pi g_{9/2}^{-1} \otimes \nu[h_{11/2}^{1}(g_{7/2}, d_{5/2})^2]$, $\pi g_{9/2}^{-1} \otimes \nu h_{11/2}^{3}$ and $\pi g_{9/2}^{-3} \otimes \nu h_{11/2}$. Lieder *et al.* [6] have calculated the excitation energies and electromagnetic transition rates for $\pi g_{9/2}^{-1} \otimes \nu[h_{11/2}^{1}(g_{7/2}, d_{5/2})^2]$ configuration within the particle rotor model framework where the core was assumed to be nearly prolate ($\beta = 0.21$ and $\gamma = 5.3°$). The calculated aligned angular momentum was found to be in good agreement for the configuration but these calculations failed to reproduce the observed falling trend of $B(M1)$ values. The second configuration $\pi g_{9/2}^{-1} \otimes \nu h_{11/2}^{3}$ was ruled out in Ref. [6] as it predicts larger alignment gain than the observed value . Thus, the third configuration with three proton holes structure becomes a possibility for band 1, however, such structure has not been reported in Ag isotopes.

In the present work, SPAC calculation has been performed with $\pi g_{9/2}^{-1} \otimes \nu[h_{11/2}^{1}(d_{5/2}/g_{7/2})^2]$ configuration proposed by Lieder *et al.* [6] and the results are compared with both experimentally observed routhian and the $B(M1)$ transition rates. For this configuration, $\left|\vec{j_1}\right|$ has been assumed to be $4.5\hbar$, which corresponds to the $g_{9/2}$ proton hole and $\left|\vec{j_2}\right| = 9.5\hbar$ is determined to reproduced the band head spin of $11\hbar$. The initial value of $\mathcal{J}$ has been assumed to be 8.6 $\hbar^2$/MeV which is consistent with the systematic of this mass region [32]. The θ values have been extracted for each level from the condition of energy minimization. The value of V_2 has been obtained from the fit to the experimental routhian up to the band crossing spin of $17\hbar$ and is found to be 0.75 MeV. The calculated values for the routhian and the $B(M1)$ transition rates are shown by the dashed lines in
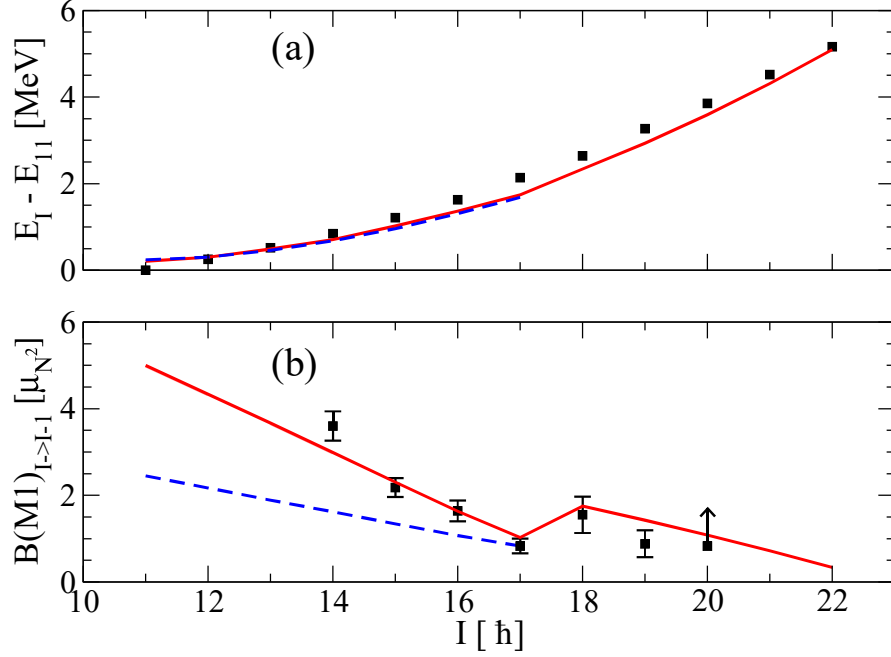
Figure 4.11: The measured and the calculated (a) routhian(E$_I$-E$_{11}$), where E_{11} is the band head energy at 11^- level and (b) $B(M1)$ rates for the band 1 of ^{106}Ag. Dotted line represents $\pi g_{9/2}^{-1} \otimes \nu[h_{11/2}(d_{5/2}/g_{7/2})^2]$ configuration and the solid line represents $\pi g_{9/2}^{-3} \otimes \nu h_{11/2}$ configuration up to $I = 17\hbar$ and $\pi g_{9/2}^{-3} \otimes \nu[h_{11/2}(d_{5/2}/g_{7/2})^2]$ configuration afterwards. Error bars on measured values of a given level include errors in intensity and lifetime of the level added in quadrature.

Fig. 4.11(a) and Fig. 4.11(b), respectively. The $B(M1)$ values have been estimated using $g_1 = 1.27, g_2 = 0.126, g_R = 0.44$ which have been calculated using the single particle g-factor values $g_{g_{9/2}} = 1.27$ for protons and $g_{g_{9/2}} = 0.21$, $g_{h_{11/2}} = -0.21$ for neutrons. It can be observed from the figure that the $B(M1)$ transition rates are clearly under-predicted and thus, $\pi g_{9/2}^{-1} \otimes \nu[h_{11/2}^1(d_{5/2}/g_{7/2})^2]$ configuration fails to describe the band 1 before the alignment.

In this connection, it may be noted that such large $B(M1)$ rates with similar falling trend has already been reported in this mass-region in a shear band

in ^{110}Cd nucleus with $\pi g_{9/2}^{-2}$ structure [43]. In addition, the three proton hole configuration $\pi[g_{9/2}^{-3}g_{7/2}] \otimes \nu[h_{11/2}^{1}(d_{5/2}/g_{7/2})]$, was assigned to the shears band of ^{108}Cd before the band crossing, which reproduced the observed $B(M1)$ transition rates [74]. Thus, the SPAC calculation has been carried out for $\pi g_{9/2}^{-3} \otimes \nu h_{11/2}$ configuration for the shears band of ^{106}Ag.

For this configuration, the $\left|\vec{j_2}\right|$ value has been assumed to be $5.5\hbar$ which corresponds to the $h_{11/2}$ neutron particle and the $\left|\vec{j_1}\right|$ value of $8.5\hbar$ has been used to reproduce the band head spin. The values of $\mathfrak{J}$ and V_2 has been kept unchanged. The calculated values are shown by solid line in Fig. 4.11(a) and Fig. 4.11(b). The calculated routhian values are similar for the two single particle configurations but the experimental $B(M1)$ values are well reproduced by the three proton hole configuration.

In order to describe the levels beyond $I = 17\hbar$, the value of $\mathfrak{J}$ has been continuously changed from 8.6 $\hbar^2$/MeV to 10.5 $\hbar^2$/MeV across the band crossing region. The variation in $\mathfrak{J}$ across the band crossing region was calculated using the Boltzmann function [9]. The V_2 value beyond the band crossing was found to be 1.5 MeV from the fit to the experimental routhian in the spin range between $18\hbar$ to $22\hbar$. This increase in V_2 value indicates that the shears structure beyond $17\hbar$ is generated by higher number of valence particles and the probable configuration is $\pi g_{9/2}^{-3} \otimes \nu[h_{11/2}^{1}(d_{5/2}/g_{7/2})^2]$. Under these assumptions, the energy minimization for each level of band 1 has been shown in Fig. 4.12, which reproduces the shears band crossing at $I = 17\hbar$. The numerical values for θ, θ_I and $\left|\vec{R}\right|$ as a function of spin are plotted in Fig. 4.13. It may be noted from Fig. 4.11(a) and Fig. 4.11(b) that these calculated values reproduces both the experimental routhian and also the magnitude and
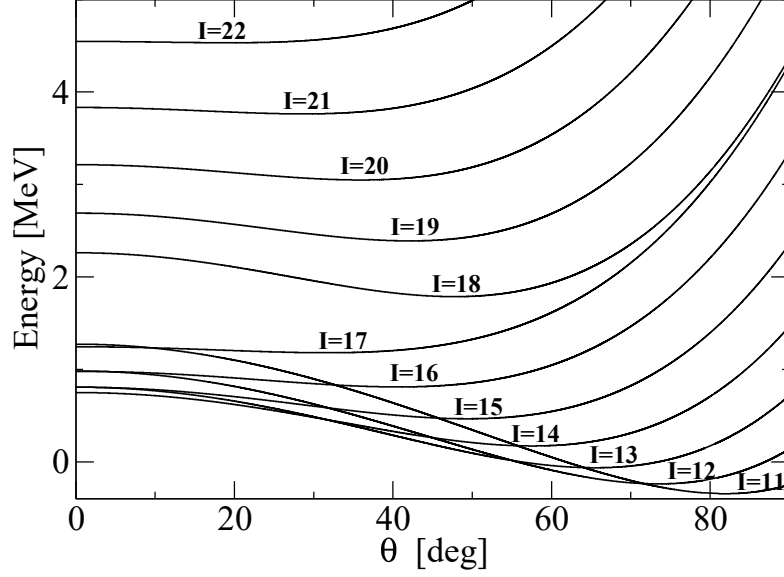
Figure 4.12: The energy minimization plot using SPAC calculation for band 1.

the spin dependence of the $B(M1)$ rates for the entire spin range of band 1. Thus, the numerical calculations based on SPAC framework give a good description of the high spin behavior of the band 1 of ^{106}Ag for $\pi[g_{9/2}^{-3}] \otimes \nu[h_{11/2}]$ configuration before the band crossing and $\pi[g_{9/2}^{-3}] \otimes \nu[h_{11/2}(d_{5/2}/g_{7/2})^2]$ configuration after.

This three proton hole configuration of band 1 is expected to exhibit strong polarization effect and hence strongly influence the $B(E2)$ transition rates. The solid line in Fig. 4.14 corresponds to the calculated $B(E2)$ values using $eQ_{\text{eff}} = 9$ eb and $eQ_{\text{coll}} = 1$ eb. As shown in the Fig. 4.14, the observed variation of the $B(E2)$ values with angular momentum is well reproduced by these values of collective and quasi particle quadrupole moments.

In the present framework, the sharp fall of the $B(E2)$ values is governed by Q_{eff}, which can be correlated to e_{pol} through the equations 2.49 and 2.50 of
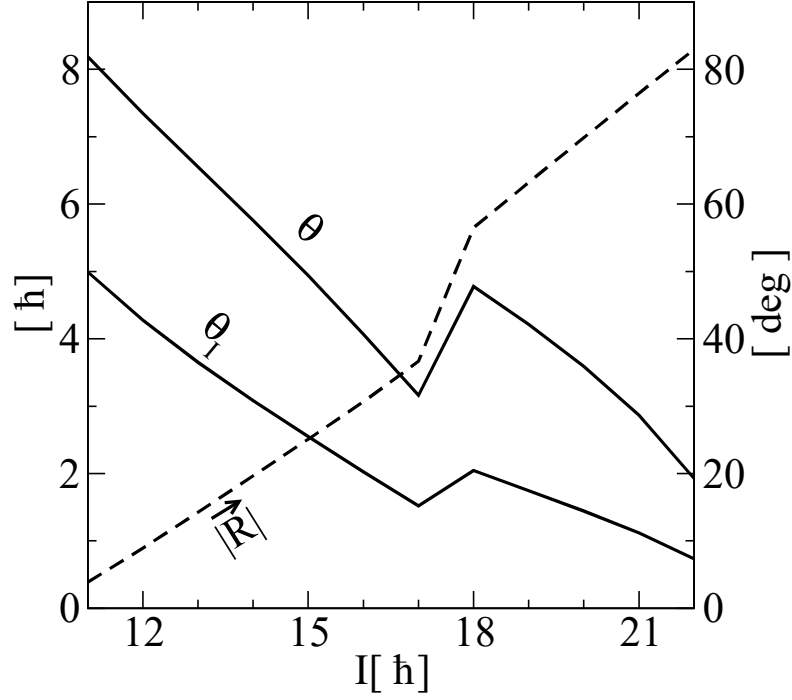
Figure 4.13: The variation for the theoretical values of θ, θ_I and R as a function of spin.

Chap. 2. A value of $\left(e_{\mathrm{pol}}\right)_{E2} \approx 5e$ has been obtained for the band 1 using $eQ_{\mathrm{eff}} = 9$ eb. The large value of the polarization charge may be attributed to the strong polarization effect due to the three proton hole configuration. It may be noted that $\left(e_{\mathrm{pol}}\right)_{E2}$ has been found to be $\sim 3e$ for the two protons and two neutrons configurations in Pb region [32]. Thus, the enhanced $B(E2)$ rates observed in the band 1 of ^{106}Ag can be described by assigning a large polarization charge in the framework of SPAC model, which is consistent with the three proton hole configuration for this band. However, it may be noted that the nuclei in this mass region are soft in both β and γ deformation [69] and an alternative explanation is also possible.
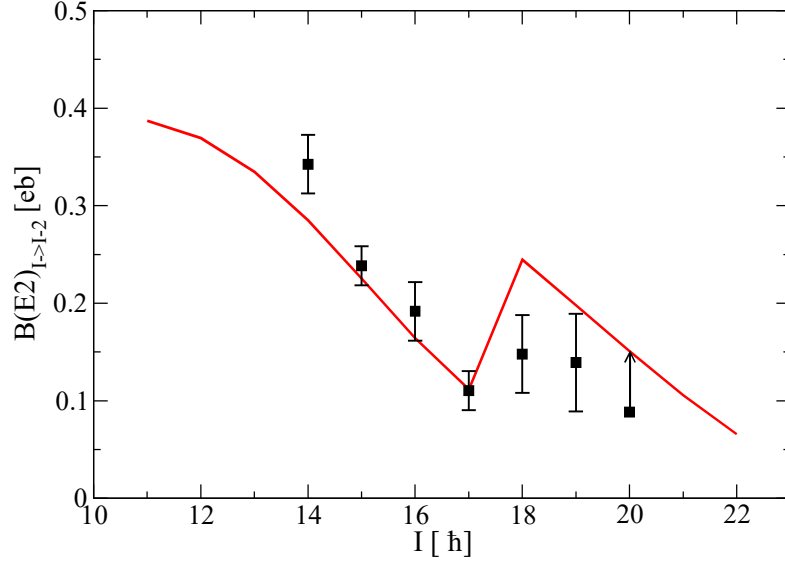
Figure 4.14: The measured and the calculated $B(E2)$ rates for the band 1 of ^{106}Ag for eQ$_{\text{eff}}$=9 eb and eQ$_{coll}$= 1 eb.

4.4.2 Band 2

The calculated transition rates for band 2 (Tab. 4.2) also shows a falling nature with increasing spin, a indication of shears mechanism as a possible case of high spin generation mechanism. The most probable single particle configuration for this positive parity band is $\pi g_{9/2}^{-1} \otimes \nu[h_{11/2}^2(g_{7/2}/d_{5/2})]$ which has also been proposed in the earlier works [72, 73]. For this configuration, the deformation aligned angular momentum, $|\vec{j}_1|$ is assumed to be $4.5\hbar$ which corresponds to the proton hole while the rotation aligned angular momentum, $|\vec{j}_2| = 10.5\hbar$ has been used in order to reproduce the band head spin of $12\hbar$. The maximum angular momentum which can be generated by this shears structure is $15\hbar$. However, the transition rates have been found to decrease steadily up to $21\hbar$, thereby indicating a contribution of $6\hbar$ from the core

rotation. This interplay of core rotation and shears mechanism prompted
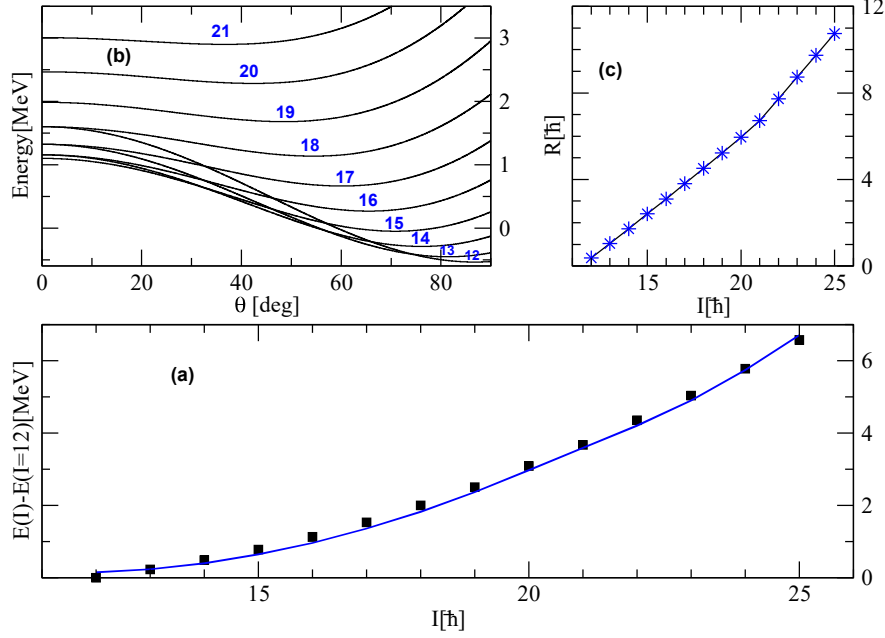
Figure 4.15: (a)The measured and the calculated routhian (E(I)-E(I=12)), where E(I=12) is the band head energy; and the solid line represents the calculated values from SPAC. (b) The energy minimization plot using SPAC. (c) The core contribution to the total angular momentum as a function of spin.

the use of the SPAC model.

In order to reproduce the transition rates the shears blades are assumed to be completely closed at $I = 21\hbar$, as the $B(M1)$ value is lowest at this spin. The best fit to the routhian between $I = 12 \rightarrow 21\hbar$ yields $V_2 = 1.1$MeV, and $\mathfrak{J} = 9$ $\hbar^2$/MeV. These values are consistent with the values obtained from the band 1. Systematics of the mass$\sim$100 region also supports the argument. After $I = 21\hbar$ the $B(M1)$ as well as $B(E2)$ rates attains a constant value. This implies a constant shears angle. So, the energy levels beyond $I = 21\hbar$ can be generated from the core rotation ($|\vec{R}(I,\theta)|$) alone while the shears angle, θ,
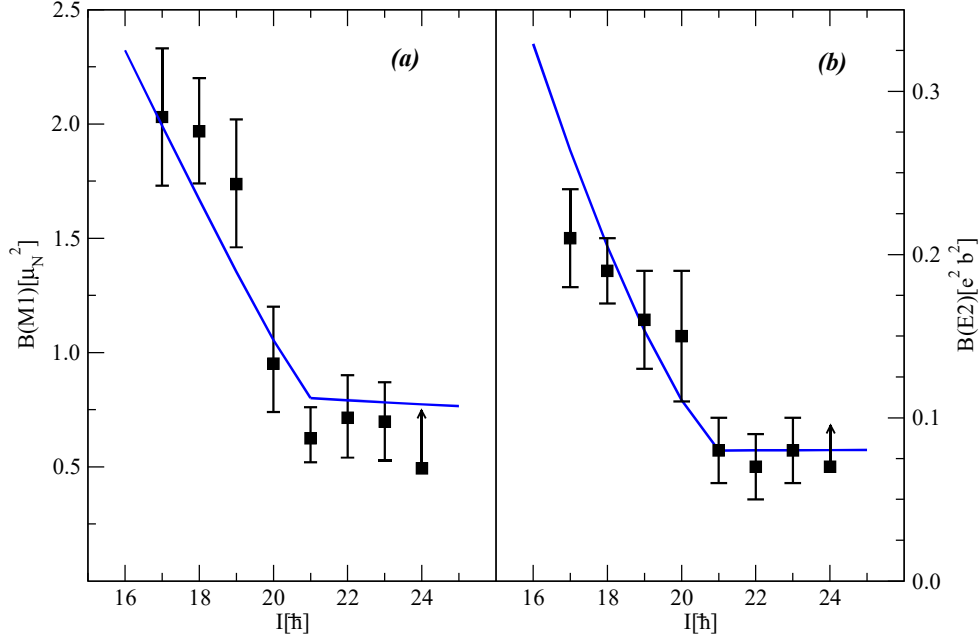
Figure 4.16: The measured and calculated (a) $B(M1)$, (b) $B(E2)$ rates for positive parity band of ^{106}Ag for $\pi g_{9/2}^{-1} \otimes \nu[h_{11/2}^2(g_{7/2}/d_{5/2})]$ configuration. Error bars on measured values of a given level include statistical errors in intensity and the level lifetime added in quadrature. The solid line represents the theoretical values with $\mathfrak{J} = 9\hbar^2/\text{MeV}$ and $V_2 = 1.1$ MeV, while the dashed line represents the theoretical values with $\mathfrak{J} = 12\hbar^2/$ MeV and $V = 2.5$ MeV.

remains fixed at the minimum value of 36.7°. In order to obtain the best fit to the observed routhian, the value of $\mathfrak{J}$ was changed continuously from 9 to 10.5 $\hbar^2/\text{MeV}$ across $I = 21\hbar$. The calculated routhian plot and $|\vec{R}(I,\theta)|$ as a function of total angular momentum shown in Fig. 4.15(a) (solid line) and Fig. 4.15(c), respectively.

The $B(M1)$ values are calculated using Eq. 4.1. The value of θ is obtained from the energy minimisation plot (Fig. 4.15(a)). The $B(M1)$ values were calculated using the single particle g-factor values of 1.27 for $g_{9/2}$ protons

and 0.21 and -0.21 for $g_{7/2}$ and $h_{11/2}$ neutrons, respectively. The calculated values are shown as solid line in Fig. 4.16(a). A good agreement between the theoretical and experimental value can be seen in the figure. It is to be
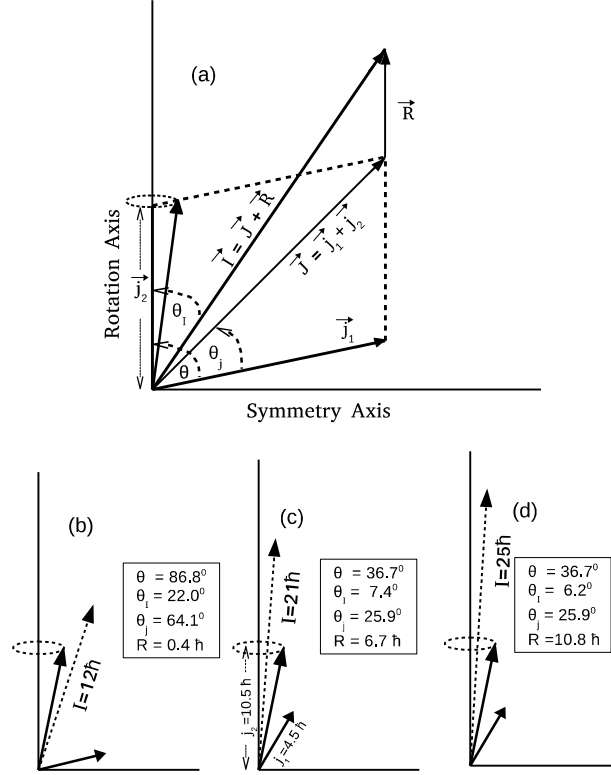
Figure 4.17: (a) The general angular momentum vector coupling used in the SPAC model. The vector alignment at different spins are shown in (b) $I = 12\hbar$, (c) $I = 21\hbar$, (d) $I = 24\hbar$.

noted that the shears angle, θ, attains a constant value at $I = 21\hbar$, but the angle between $\vec{j}_2$ and $\vec{I}$, θ_I, decreases afterwards. Because of this decrease in θ_I value the $B(M1)$ rates also fall slowly. However within the limit of uncertainty the experimental data indicates a almost constant value. The snapshots of the angular momentum coupling at different spins are shown at

Fig. 4.17.

The next step is to check the validity of single particle configuration used in this calculation. For this, the $B(E2)$ values are fitted between the spin range $I = 17 \rightarrow 21\hbar$ using Eq. 4.2. The quadrupole moments obtained from the best fit (shown in Fig. 4.16(b)) are $eQ_{\mathrm{eff}} = 4.42$ eb and $eQ_{\mathrm{coll}} = 0.63$ eb. Using these values, a polarisation charge of $\left(e_{\mathrm{pol}}\right)_{E2} \sim 2e$ has been obtained, which is lower than that observed in band 1 and the possibility of three proton hole structure can be ruled out.

4.5   Summary

The lifetimes of the high spin levels of band 1 in ^{106}Ag has been measured using the DSAM. The deduced $B(M1)$ and $B(E2)$ rates exhibits a sharp fall up to $I = 17\hbar$ followed by a small increase and again a slow fall. The γ-ray energies also exhibit a discontinuity at $I = 17\hbar$. These features have been described within the framework of SPAC model as a shears band crossing. The observed large $B(M1)$ values can only be explained by assuming a three proton hole configuration for this band. In addition, the observed $B(E2)$ transition rates can be described by assuming a large polarization charge. This observation is also consistent with the three proton hole configuration for the band 1 of ^{106}Ag.

The positive parity band-structure of ^{106}Ag has been extended significantly. The lifetimes of the levels of this band were extracted using the DSAM. The deduced $B(M1)$ and $B(E2)$ values decrease with increasing spin up to $I = 21\hbar$ which is the manifestation of shears mechanism. Beyond $I = 21\hbar$, the

transition rates remain substantially small and exhibit a slow gradual change. The comparison between the experimental data and the SPAC calculations seems to indicate a novel observation of a transition from shears mechanism to non-collective rotation in the band 2 of ^{106}Ag.

5

High spin states in ^{110}Ag

5.1 Introduction

The odd-odd Ag isotopes are in the focus of contemporary nuclear structure research in connection to the observation of nearly degenerate bands and the possibility of identifying them as chiral partners. These experimental studies are primarily centered around the negative-parity doublet bands with $\pi g_{9/2}^{-1} \otimes \nu h_{11/2}^{1}$ configuration [51, 70, 69]. The results seem to indicate that these doublet bands may correspond to different nuclear shapes associated with different γ-values or have different single particle configurations but are not the chiral partners [38]. It is not uncommon among nuclei to possess γ softness where the valance neutrons and the protons occupy competing shape driving orbitals and the Ag isotopes are no exceptions. However, such configurations may also lead to shears like structures [43, 34], and hence, the tilted (non principal) axis rotation emerges as an alternate possibility

of generating the higher angular momentum states. Such possibilities have been investigated in Ag isotopes both for the positive and the negative-parity bands up to ^{109}Ag [7, 10, 14, 75]. It has been observed that for the higher spin states, the in-band M1 transition energies exhibit an increasing trend while the $B(M1)$ transitions rates fall smoothly with increasing spin. These features indicate the loss of π-rotational symmetry as a consequence of tilted axis rotation [34]. However, it is to be noted that these transitional nuclei are moderately deformed, therefore, the role of core rotation needs to be considered. This is corroborated by the fact that the majority of these bands are observed beyond the maximum spin achievable by the complete closing of the angular momentum vectors of the particles and the holes [32]. Thus, a semi-classical model, shears with principal axis cranking (SPAC) [9], has been successfully employed in recent times to study both the positive and the negative-parity bands of the Ag isotopes [7, 10].

A deviation from this systematic was first reported by our group in ^{110}Ag [12]. It is the heaviest Ag isotope studied so far using the heavy-ion induced fusion evaporation reaction and only the negative-parity yrast band was established. Unlike the lighter Ag isotopes, the high spin states of ^{110}Ag display staggering of the in-band M1 transition energies and in the $B(M1)$ transition rates, till the highest observed spin of $20\hbar$ [12]. This observed staggering is the characteristic of the principal axis rotation and is associated with the signature quantum number. Thus, N = 62 is the neutron boundary for the dominance of the tilted axis rotation along the yrast band in Ag isotopes. However, it is an open question whether the same conclusion holds true for the non-yrast bands of ^{110}Ag.

In this work, two non-yrast bands (1 and 2) have been identified for the first time which predominantly decays to the isomeric 6^+ state through a newly observed decay path and also through the known yrast sequence [12]. The level lifetime measurements have been carried out for the high spin states of the positive parity band (band 2), while the same for the negative parity band (band 1) was not possible due to inadequate statistics. However, the $B(M1)/B(E2)$ values were estimated from the measured intensities to understand the angular momentum generation mechanism in band 1.

5.2 Experiment

The high spin states of ^{110}Ag were populated using the 70 MeV ^{18}O beam from the 15-UD Pelletron at Inter University Accelerator Center, New Delhi through the ^{96}Zr(^{18}O, p3n)^{110}Ag reaction. The 1 mg/cm^2 thick enriched ^{96}Zr target had a ^{206}Pb backing of thickness 9 mg/cm^2. The γ rays were detected in the INGA setup of IUAC [57], which consisted of 18 Compton suppressed clover detectors. These detectors were arranged in rings at 32°, 57°, 90°, 123° and 148° with respect to the beam direction. The data acquisition system used here has been described in Chap.3. The data trigger was set to three or higher fold prompt γ-ray coincidence which resulted into 1.3 billion events. It is to be noted that the ^{96}Zr(^{18}O, p3n)^{110}Ag reaction channel contains only about 2% of the total fusion-evaporation cross-section while the pure neutron evaporation channels consume 95%. Thus, the present investigation of ^{110}Ag is primarily based on the γ- γ- γ cube analysis.

5.3 Analysis and results

The data sorting was done by the offline codes described in Chap.3. The angle dependent asymmetric matrices were used for the lineshape analysis using the DSAM. In order to measure the γ-ray multipolarities by the DCO ratio method [76], an angle dependent matrix was constructed by placing the γ-ray energy detected at 90° along one axis while the coincident γ-ray energy at 32° on the other axis. The linear polarization measurement was also performed to extract the electromagnetic character of the de-exciting γ rays using the integrated PDCO method [66]. The details of the method and the procedure have been discussed in Chap.3. These analysis were first performed on the strong transitions of the ^{109}Cd in order to validate the methods.

5.3.1 Level scheme

The non-yrast levels of ^{110}Ag were first identified using the 1229 keV gate for band 1 and the 1357 keV gate for band-2 (shown in the inset of Fig. 5.1(a) and (b)), which showed a sequence of low energy γ-transitions (272, 312, 366 keV for band 1 and 185, 194, 246 and 320 keV for band-2) in coincidence with the 191, 407 and 746 keV transitions of the yrast cascade. The observation of the cross-over transitions corresponding to these transitions confirm their placement, and their ΔI=1 character. The γ-transitions belonging to the band 1 could be identified from the triple gate of 273 ($7^+ \rightarrow 6^+$) or 384 ($8^+ \rightarrow 7^+$) keV or 191 ($9^- \rightarrow 8^-$) or 407 ($10^+ \rightarrow 9^+$) keV and 312 ($13^- \rightarrow 12^-$) keV as shown in Fig. 5.1(a). On the other hand, the γ-transitions belonging to band-
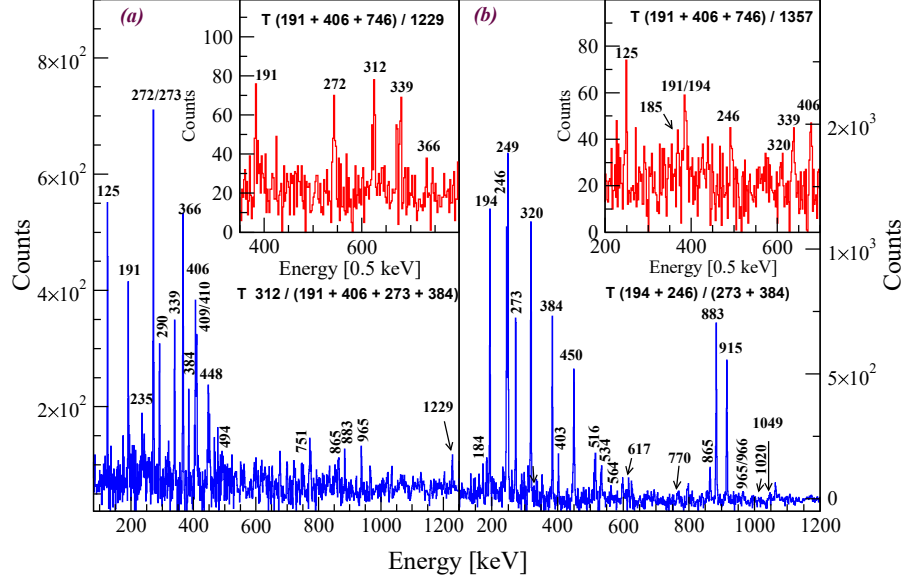
Figure 5.1: (a) The triples gated spectrum generated by the coincidence condition of 273 ($7^+ \rightarrow 6^+$) or 384 ($8^+ \rightarrow 7^+$) keV or 191 ($9^- \rightarrow 8^-$) or 407 ($10^+ \rightarrow 9^+$) keV with 312 ($13^- \rightarrow 12^-$) keV transition. The transitions belonging to band 1 are marked accordingly. The triples spectrum of 1229 ($12^- \rightarrow 11^-$) keV transition with 191 ($9^- \rightarrow 8^-$) or 407($10^- \rightarrow 9^-$) or 746 ($11^- \rightarrow 9^-$) keV transitions is shown in the inset. (b) The triples gated spectrum generated by the coincidence condition of 194 ($14^+ \rightarrow 13^+$) or 246 ($15^+ \rightarrow 14^+$) keV with 273 ($7^+ \rightarrow 6^+$) or 384 ($8^+ \rightarrow 7^+$) keV transitions. The transitions belonging to band-2 of ^{110}Ag are marked accordingly. The triples spectrum of 1357 ($12^+ \rightarrow 11^-$) keV transition with 191 ($9^- \rightarrow 8^-$) or 407($10^- \rightarrow 9^-$) or 746 ($11^- \rightarrow 9^-$) keV transitions is shown in the inset.

2 were identified from the triple gate of 273 ($7^+ \rightarrow 6^+$) or 384 ($8^+ \rightarrow 7^+$) keV and 194 ($14^+ \rightarrow 13^+$) or 246 ($15^+ \rightarrow 14^+$) keV as shown in Fig. 5.1(b). These newly observed transitions were placed according to their relative intensities after satisfying the corresponding coincidence criteria. The result of these observations has been summarized in the partial level scheme of ^{110}Ag as shown in Fig. 5.2. It is to be noted that few positive-parity states were previously reported [77]. However these states were not observed in the present

experiment.

In order to measure the relative intensities of the non-yrast states, the intensities of the 272, 312, 194 and 246 keV transitions were first estimated from the 191 ($9^- \rightarrow 8^-$) keV gate and were normalized with respect to the intensities of the 468 ($14^- \rightarrow 13^-$) and 491 ($13^- \rightarrow 12^-$) keV transitions. These normalized values were further multiplied by the intensity ratio of 273 to 191 keV transitions to estimate the true intensities. The further increment to the intensities due to the parallel decay path of 658 ($8^+ \rightarrow 6^+$) keV was done by noting the relative intensities of 273 and 658 keV transitions. The rest of the γ-ray intensities were determined relative to the estimated intensities of 312 keV for band 1 and 194 and 246 keV for band-2.

It may be noted that, both the non-yrast bands are well anchored with respect to the yrast band. The spin and parity of the band-heads were assigned through the DCO and the iPDCO measurements of these anchoring transitions. The $M1$ character of the 1229 keV transition fixed the spin and parity of the 12^- level of band 1 and the $E1$ character of the 1278 and 1357 keV transitions fixed the 11^+ and 12^+ levels of band-2 respectively. These measured DCO and iPDCO values have been listed in Table. 5.1.

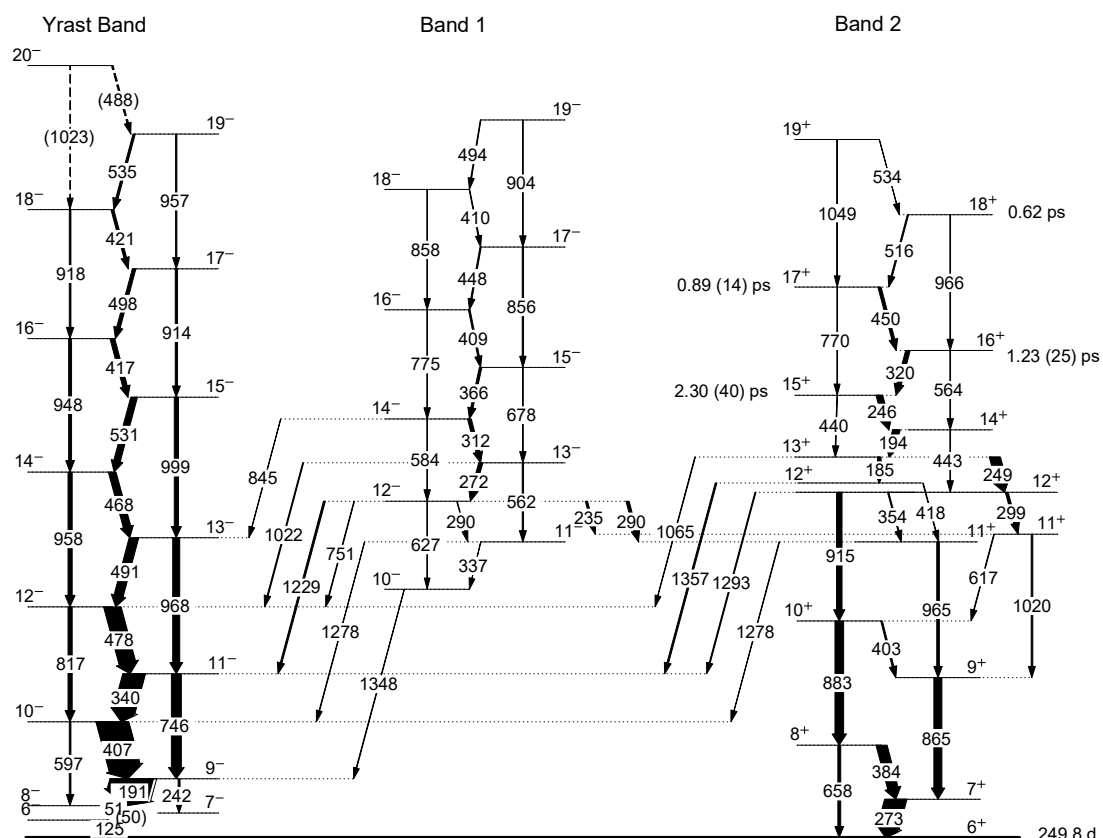Figure 5.2: The partial level scheme of the ^{110}Ag. All the non-yrast levels and their decay paths have been observed for the first time. The deduced level lifetimes for the 15^+, 16^+, 17^+ and 18^+ levels are indicated. However, the quoted value for the 18^+ level is the effective lifetime.

E_γ(keV)	$I_i^\pi \to I_f^\pi$	Rel. Intensity	DCO	iPDCO
185	$13^+ \to 12^+$	7.8(1.0)	0.77(0.20)	
194	$14^+ \to 13^+$	16.6(1.1)	0.82(0.12)	
235	$12^- \to 11^+$	5.0(1.2)		
246	$15^+ \to 14^+$	14.7(1.0)	0.92(0.12)	
249	$13^+ \to 12^+$	24.3(0.9)	1.07(0.13)	-0.02(0.01)
272	$13^- \to 12^-$	9.2(0.9)		
273	$7^+ \to 6^+$	50.0(3.0)	0.69(0.11)	
290	$12^- \to 11^+$	7.0(2.2)		
290	$12^- \to 11^-$	<1		
299	$12^+ \to 11^+$	6.5(1.2)	0.84(0.10)	
312	$14^- \to 13^-$	8.9(1.0)		-0.17(0.10)
337	$11^- \to 10^-$	<1		
320	$16^+ \to 15^+$	10.3(1.1)	0.70(0.14)	-0.18(0.10)
354	$12^+ \to 11^+$	2.7(0.6)		
366	$15^- \to 14^-$	5.8(0.8)		
384	$8^+ \to 7^+$	25.1(3.0)	0.67(0.14)	-0.08(0.10)
403	$10^+ \to 9^+$	4.1(0.6)	0.71(0.20)	
409	$16^- \to 15^-$	3.7(0.5)		
410	$18^- \to 17^-$	2.0(0.6)		
418	$12^+ \to 11^+$	1.5(0.3)	0.79(0.22)	
440	$15^+ \to 13^+$	1.8(0.3)		
443	$14^+ \to 13^+$	1.3(0.3)		
448	$17^- \to 16^-$	2.7(0.4)		
450	$17^+ \to 16^+$	7.3(2.0)		
494	$19^- \to 18^-$	1.6(0.3)		
516	$18^+ \to 17^+$	3.1(0.8)		
534	$19^+ \to 18^+$	1.2(0.3)		
562	$13^+ \to 11^+$	2.7(0.3)		
564	$16^+ \to 14^+$	1.4(0.4)		
584	$14^- \to 12^-$	1.3(0.2)		
627	$12^- \to 10^-$	<1		
617	$11^+ \to 10^+$	1.4(0.2)		
658	$8^+ \to 6^+$	7.4(1.2)		
678	$15^- \to 13^-$	2.1(0.2)		
751	$12^- \to 12^-$	1.6(0.2)		
770	$17^+ \to 15^+$	1.3(0.4)		
775	$16^- \to 14^-$	1.3(0.2)		
856	$17^- \to 15^-$	2.5(0.6)		
858	$18^- \to 16^-$	1.2(0.4)		
865	$9^+ \to 7^+$	18.9(1.5)	1.68(0.71)	0.22(0.08)
883	$10^+ \to 8^+$	20.1(2.1)		
904	$19^- \to 17^-$	1.5(0.3)		
915	$12^+ \to 10^+$	13.9(1.6)	1.40(0.25)	0.20(0.09)
965	$11^+ \to 9^+$	6.0(1.2)	1.20(0.22)	0.24(0.08)
966	$18^+ \to 16^+$	1.8(1.0)		
1020	$11^+ \to 9^+$	3.8(0.7)		
1049	$19^+ \to 17^+$	0.7(0.6)		
1065	$13^+ \to 12^-$	1.0(0.5)		
1229	$12^- \to 11^-$	1.1(0.1)	0.84(0.60)	-0.11(0.02)
1278	$11^+ \to 10^-$	1.1(0.1)	0.76(0.40)	0.15(0.10)
1278	$11^- \to 10^-$	<1		
1293	$12^+ \to 11^-$	1.8(0.2)	0.64(0.14)	
1348	$10^- \to 9^-$	<1		
1357	$12^+ \to 11^-$	3.3(0.2)	0.66(0.20)	0.24(0.13)

Table 5.1: The energies, the relative intensities, the DCO and the iPDCO ratios for newly placed γ transitions of ^{110}Ag. The uncertainty in the γ-ray energies were ~ 0.4 keV for strong transitions (intensity ≥ 10) and ~ 0.6 keV for weaker **122** transitions. The relative intensities were scaled by considering the intensity of 191 $(9^- \to 8^-)$ keV transition as 100.

It may be noted that as per the systematic of the odd-odd Ag isotopes, the lowest observed 6^+ state is common to both the positive and the negative-parity sequences. In order to realize the same structure in ^{110}Ag, a transition of 50 keV has been assumed between 7^- to 6^- levels in the yrast sequence which was otherwise reported as 'unobserved' in all the previous works [78, 79]. It may be noted that this value is consistent with that of ^{106,108}Ag, where these transition energies are 64.2 and 58.5 keV [71, 51], respectively.

The band heads of the two non-yrast bands are at $I = 12\hbar$, thereby indicating a 4 quasiparticle structure for both of them.

5.3.2 Lifetime measurement : DSAM

In order to investigate further the underlying excitation mechanism of these states, the transition rates were measured for the $I = 15^+$ to 18^+ levels. The lifetime of these levels were obtained by fitting the observed line shapes of the corresponding M1 transitions at 57°, 90° and 123° simultaneously with the theoretical line shapes derived from the code LINESHAPE by Wells and Johnson [68]. The details of the fitting procedure has been discussed in detail in Chap.2.

The observed lineshape of the 516 keV ($18^+ \rightarrow 17^+$) transition was fitted assuming 100% side-feed. This analysis provided the effective lifetime for the $I = 18\hbar$ level. The next lower transition in the sequence was fitted with this effective lifetime and the side-feeding lifetime as the input parameters. The side-feeding into each level were modeled as a cascade of five transitions with the comparable moment of inertia of the present band. The quadrupole

moments of the side-feeding sequences were allowed to vary which combined with the moment of inertia gave an effective side-feeding lifetime parameters for each level. It is to be noted that the side-feeding at a given level was fixed to the missing intensity determined from the spectra at 90° with respect to the beam direction. This way the three levels of the band were added

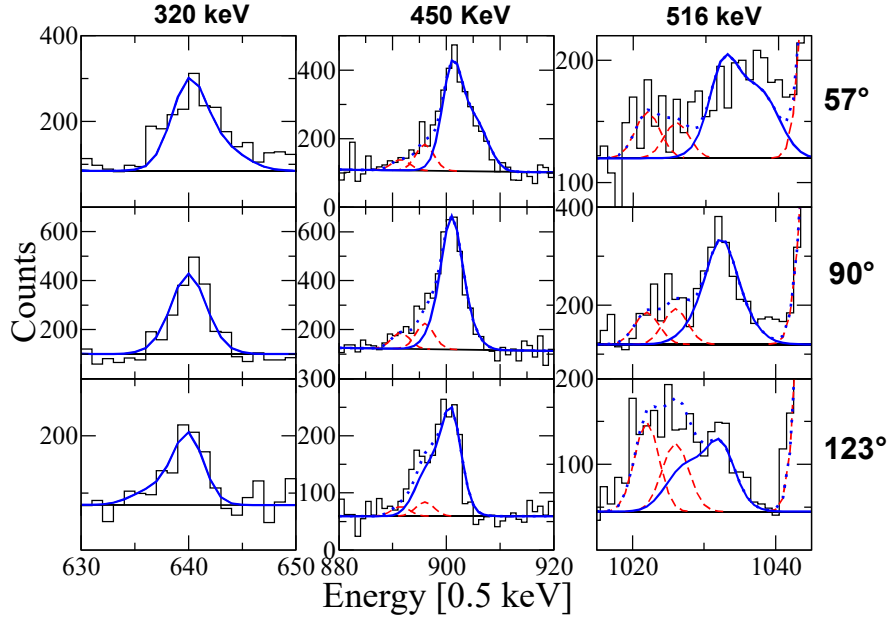

Figure 5.3: The examples of the lineshape fits for 320 ($16^+ \rightarrow 15^+$) keV, 450 ($17^+ \rightarrow 16^+$) keV and 516 ($18^+ \rightarrow 17^+$) keV transitions at 57°, 90° and 148° with respect to the beam direction. The Doppler broadened line shapes are drawn in solid lines while the contaminant peaks are shown in dashed lines. The result of the fit to the experimental data is shown in dotted lines.

sequentially one after another and the corresponding lineshapes were fitted. The uncertainties in these measurements were derived from the behavior of the χ^2 around the minimum for the simultaneous fit at the three angles. The effect of variation of the side-feeding intensity and lifetime were estimated by finding the level lifetimes for the extreme values of these two parameters and

it was found to be $\sim 20\%$. The final statistical uncertainty was calculated by adding in quadrature the uncertainties due to line-shape fitting, side-feeding intensity and side-feeding lifetime. However, this estimated error does not include the systematic uncertainty that arises due to the choice of the stopping powers which may have additional contribution of 8% at low spins to 15 % for the topmost level. The examples of the line-shape fits are shown in Fig. 5.3 and the measured level lifetime values are given in the level scheme of Fig. 5.2.

The experimentally observed level lifetimes were used to extract the electromagnetic transition rates without any loss of generality. The derived $B(M1)$ and the $B(E2)$ values have been plotted in Fig. 5.9(a) and (b), respectively. It is apparent from the Fig. 5.9 that both the $B(M1)$ and the $B(E2)$ rates fall rapidly between the spin range of 15 $\hbar$ to 17 $\hbar$. In contrast, the yrast levels in the same spin domain exhibit the staggering in the $B(M1)$ rates while the $B(E2)$ rates remain nearly constant [12].

5.4 Discussion

5.4.1 Band 1

The yrast band sequence of ^{110}Ag is build on a single particle configuration $\pi g_{9/2}^{-1} \otimes \nu h_{11/2}^{1}$ up to $I = 16\hbar$ and $\pi g_{9/2}^{-1} \otimes \nu h_{11/2}^{3}$ after that [12]. Moreover, the signature staggering observed in this band was attributed to the principle axis rotation of a triaxial core ($\gamma \sim 30^0$). This high-j particle-hole structure along with the triaxiality of the core, enhances the likelihood of observing
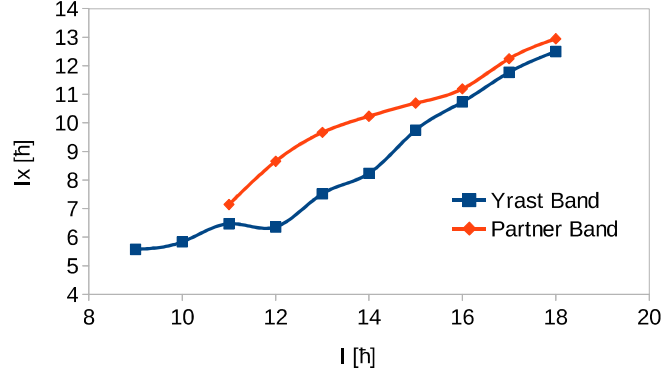
chiral partner bands.

Figure 5.4: The quasi particle aligned angular momentum (I_X) as a function of spin.

In this regard, the structure of band 1 has been explored further to investigate the similarity in its properties with the yrast band. In order to establish the single particle structure of this band, the aligned angular momenta of the two bands have been plotted in Fig. 5.4. A nearly identical aligned angular momentum can be seen in both the bands for $I > 15\hbar$. This led us to assign a single particle structure of $\pi g_{9/2}^{-1} \otimes \nu h_{11/2}^{3}$ for the band 1 beyond $15\hbar$. On the other hand, the plotted routhian in Fig. 5.5 shows that the experimental energy separation between these bands is 212 keV at $I = 15\hbar$ and continually decreases to a value of 100 keV at $I = 19\hbar$. Based on these properties, the negative parity bands may be identified as the partners beyond $15\hbar$.

The partner bands rising from the chiral geometry of a nucleus is expected to be observed at a sufficiently high spin, so that the magnitude of the core rotation is comparable to the particle and hole spin [47]. This condition is fulfilled beyond $15\hbar$, as $I_X \sim 12\hbar$. Moreover, the bands tend towards an energy degeneracy at the high spin, which relates to the fact that the chi-
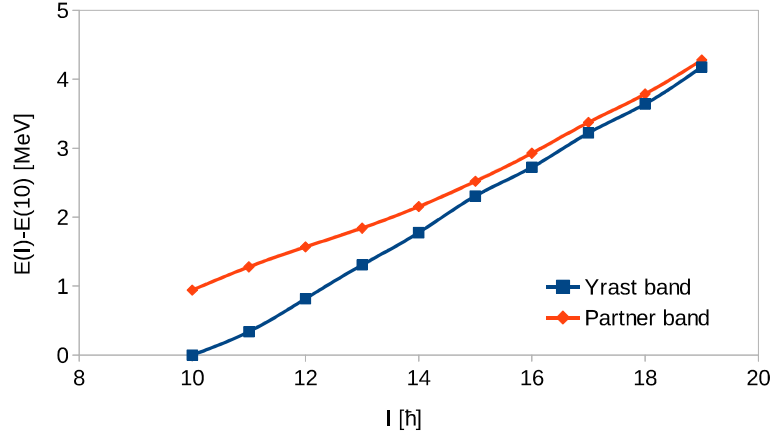
Figure 5.5: The experimental energy $(E(I) - E(10))$ as a function of spin for the partner bands, where $E(10)$ is the energy of the 10^- state of the yrast band.

ral symmetry breaking is getting stronger with increasing spin. Both the bands exhibit an in-phase signature staggering for $I > 15\hbar$ and to magnify the effect, the staggering parameter $S(I)\left(\frac{E(I)-E(I-1)}{2I}\right)$, has been plotted in Fig. 5.6. As can be seen from this figure that a similar trend of $S(I)$ beyond 15 $\hbar$ strengthen the possibility of chiral partners. Finally, a same transition rate behaviour is expected to confirm the bands as chiral partners. As discussed earlier, absolute values of the transition rates could not be measured because of the weak statistics. However, the ratio of the transition rates, $B(M1)/B(E2)$, were estimated using the measured intensities. The plotted $B(M1)/B(E2)$ values in Fig. 5.7, establish a similar staggering trend for the partner bands. Thus, the negative parity bands of ^{110}Ag could be identified as strong candidates for the chiral partners beyond the spin 15 $\hbar$. The four quasi-particle structure, $\pi g_{9/2}^{-1} \otimes \nu h_{11/2}^3$, for these bands also strengthen the possibility of spin-chirality, as the mixing with other 4-qp bands is expected to be small. It is to be noted here that, this is the first time that the
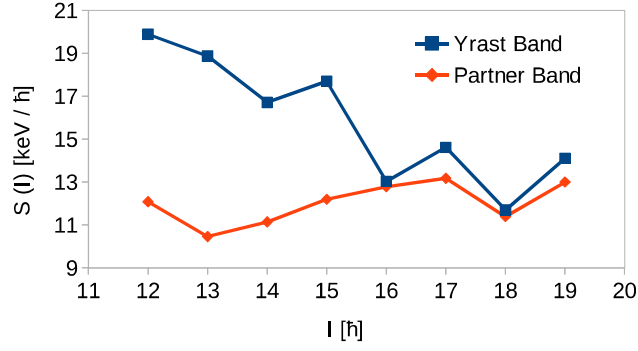
Figure 5.6: The $S(I)$ $\left(= \frac{E(I)-E(I-1)}{2I} \right)$ plot as a function of spin for the partner bands.

phenomena of spin-chirality may have been identified to a four quasiparticle configuration in the mass ~ 100 region nuclei.
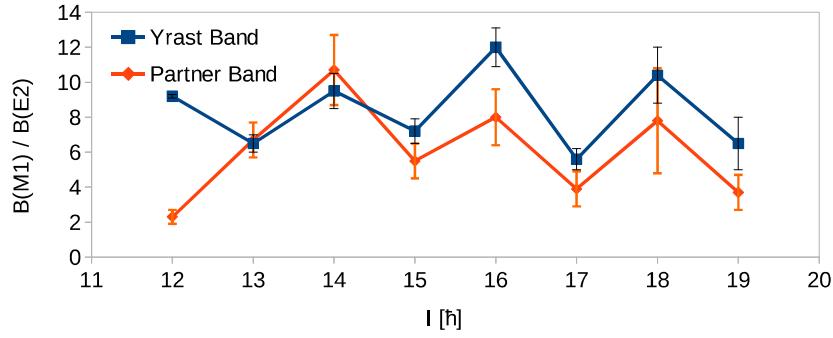
Figure 5.7: The $B(M1)/B(E2)$ ratios for the partner bands.

5.4.2 Band 2

It is observed from the level scheme (Fig. 5.2) that the high spin levels between 12^+ and 19^+ form a band structure which is very similar to that observed in ^{106}Ag [10]. It is interesting to note that the energies of the M1 transitions in this band increases smoothly in contrast to those in the negative-parity band which exhibit a staggering in energy. This feature has

been depicted in Fig. 5.8. The energy staggering in the negative-parity band has been associated to the signature splitting [80]. Thus, the absence of signature splitting in the positive-parity band may indicate the loss of π-rotational symmetry which in turn can be associated to the tilted axis rotation. The low spin states of this band has been considered to arise from
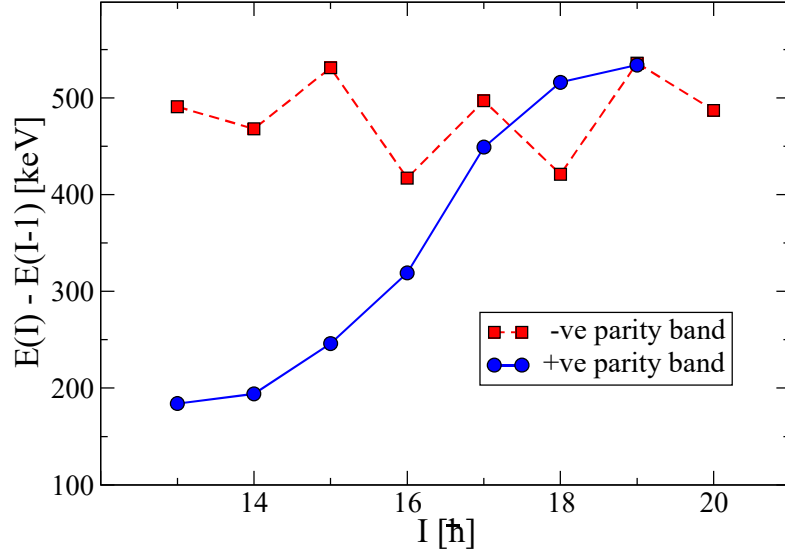

Figure 5.8: The energy difference $E(I) - E(I-1)$ as a function of spin for the positive and the negative-parity bands of ^{110}Ag.

the $\pi g_{9/2}^{-1} \otimes \nu(d_{5/2}/g_{7/2})^1$ configuration. This assignment is due to the limited phase space available to the proton sector due to large Z = 50 shell gap and the presence of $h_{11/2}$ intruder orbital for the neutrons. Thus, the choice of positive-parity states at low spin, restrict the neutron single particle levels to the $d_{5/2}$ and the $g_{7/2}$ while the proton to the $g_{9/2}$ orbital. The high spin levels ($I > 12\hbar$) have significantly large aligned angular momentum of $\sim$10 $\hbar$. In this mass region, such large aligned angular momentum can only be associated with the neutron alignment in $h_{11/2}$ orbital which lead to

the $\pi g_{9/2}^{-1} \otimes \nu[(d_{5/2}/g_{7/2})^1 h_{11/2}^2]$ configuration for the positive-parity band. It may be noted that this configuration is suitable for shears mechanism and, thus, the observed falling trends in the $B(M1)$ and the $B(E2)$ rates can be understood as a consequence of this mechanism.

In this context, I have calculated the experimental routhian and the transition rates within the framework of the SPAC model to examine the validity of the above assumptions. Recently this model has been successfully used to describe the routhian and the transition rates in both the positive and the negative-parity bands in ^{106}Ag [7, 10]. The details of this model have been discussed in the Chap.2 of this thesis.

The present SPAC calculation for the positive-parity band was performed for the $\pi g_{9/2}^{-1} \otimes \nu[(d_{5/2}/g_{7/2})^1 h_{11/2}^2]$ configuration with the band-head at 12^+. The deformation aligned angular momentum vector ($|\vec{j}_1|$) was assumed to be 4.5 $\hbar$ which corresponded to the contribution of the lone proton-hole in the $g_{9/2}$ orbital. The $|\vec{j}_2|$ was calculated to be 10.5 $\hbar$ to reproduce the band-head. It is to be noted that the maximum possible angular momentum that can be generated by this geometry is 15 $\hbar$. However, the present band extends up to 19 $\hbar$ and this extra four units of angular momentum is accommodated in the present version of SPAC through the core rotation. The best simultaneous fit to the experimental routhian and $B(M1)$ rates was observed for an effective moment of inertia $\mathcal{J} = 8 \ \hbar^2/\text{MeV}$ and the shears potential $V_2 = 0.8$ MeV which are consistent with this mass region [7, 10]. The results of these best fits to the $B(M1)$ transition rates and the experimental routhian are shown by the solid lines in Fig. 4.11(a) and 4.11(c) respectively. It is to be noted that though the present calculation reproduces the trend of the observed

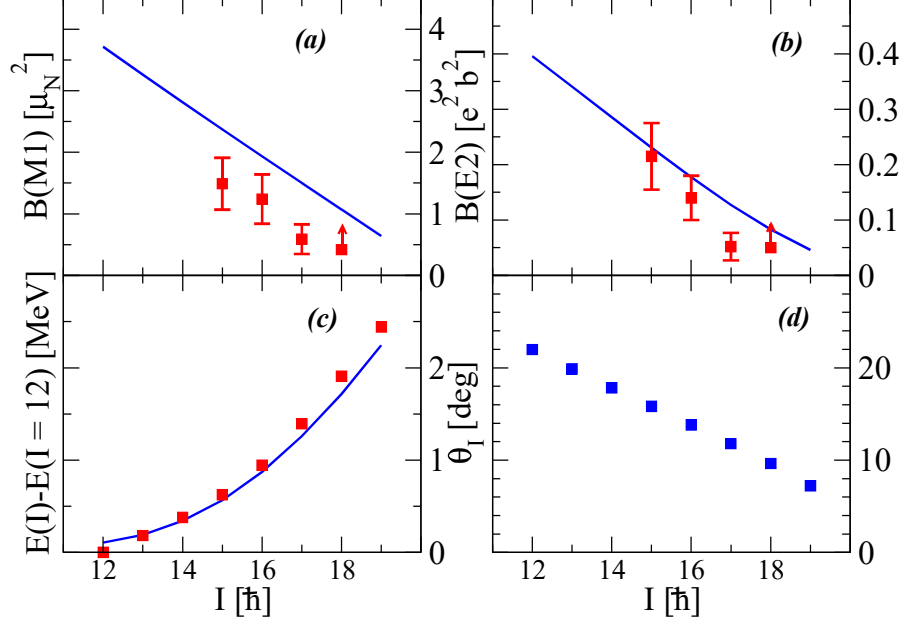B(M1) rates, it predicts relatively higher values. This may be attributed

Figure 5.9: The measured and calculated (a) B(M1), (b) B(E2) rates for the positive-parity band of ^{110}Ag. (c) The measured and the calculated Routhian [E(I) - E(I = 12)], where E(I = 12) is the band-head energy and the solid line represents the calculated values from SPAC. (d)The tilt angle (θ_I) as a function of angular momentum (I).

to the simplistic geometric approach of the model calculation as well as the choice of the gyromanetic factor to their free values. The best fit to the experimental $B(E2)$ values (Fig. 4.11(b)) was obtained for $eQ_{\mathrm{eff}} = 3.5$ eb and $eQ_{\mathrm{coll}} = 0.5$ eb. It is to be noted that eQ_{eff} is related to the core polarisation effect measured by the polarisation charge e_{pol} [9]. In the present case a polarisation charge of $e_{\mathrm{pol}} \sim 2e$ is obtained which is consistent for the present single particle configuration [10] of one valance proton. The variation of the tilt angle (θ_I) as a function of the angular momentum is shown in Fig. 4.11(d).

This value changes from 22° at $I = 12\hbar$ to 7° at $I = 19\hbar$ while in the present geometry, the principal axis rotation corresponds to $\theta_I = 0°$.

From the above discussion it can be concluded that the observed features of the positive-parity band can be described by assuming non-principal (tilted) axis rotation.

5.5   Summary

In summary, an extended level scheme with the non-yrast negative and positive parity band structures in the neutron-rich ^{110}Ag has been identified for the first time. The observed negative parity partner bands above $I = 15\hbar$ have been identified as chiral-doublets. Chiral doublets built on a four quasi-particle structure may have been observed for the first time in the mass $\sim$ 100 region.

On the other hand, the levels lifetimes of the positive-parity band has been measured and the deduced $B(M1)$ and $B(E2)$ rates exhibit a falling trend with increasing spin. These are the distinctive features of tilted axis rotation.

6

The staircase bands in $^{105,\,107,\,109}$Ag

6.1 Introduction

The band structures in nuclei are formed through a sequence of predominantly electric quadrupole ($E2$) or magnetic dipole ($M1$) transitions. The $E2$ bands are mostly formed due to the rotation of a quadrupole deformed nucleus. The nature of these bands are governed by the collective properties of all the nucleons. An exception can be found in the $E2$ bands generated from the 'antimagnetic rotation' [34], where the angular momentum is generated by the shears mechanism.

On the other hand, the behaviour of the $M1$ bands are governed by the unpaired nucleons, as there is no collective contribution to the $M1$ transition operator. In a deformed odd or odd-odd nucleus, the $M1$ transitions are accompanied with cross-over $E2$ transitions and the band structure follow the $E(I) \propto I(I+1)$ behaviour. If the Fermi levels of the unpaired nucleons are

close to $\Omega = \frac{1}{2}$, then a staggering in the $M1$ transition energies is observed. Otherwise, the $M1$ transition energies increase smoothly. In the first case the $B(M1)$ transition rates exhibits staggering , while in the second case it remains nearly constant.

However, $M1$ bands generated from the 'shears mechanism' [32] has a completely different origin. Here the simultaneous alignment of high-Ω proton (neutron) holes and low-Ω neutron (proton) particles generate the high-spin states. The level energy in these bands also follow a nearly $E_I \propto I(I+1)$ behaviour and the $M1$ transition energies increases smoothly. However in this case, the $B(M1)$ transition rates are large and shows a decreasing trend with increasing spin. Thus, the angular momentum generation mechanism leaves
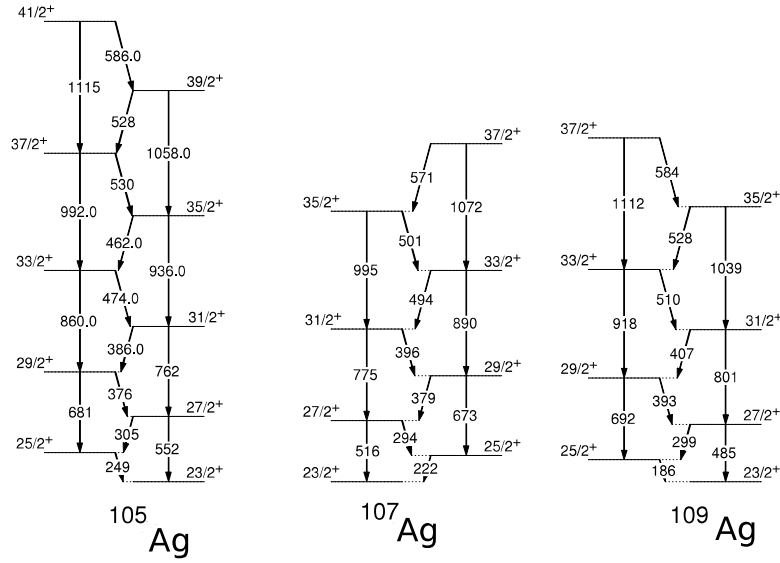

Figure 6.1: The staircase bands in $^{105,\,107,\,109}$Ag nuclei.

its footprint in the band structure and most importantly, in the transition rates observed in a band.

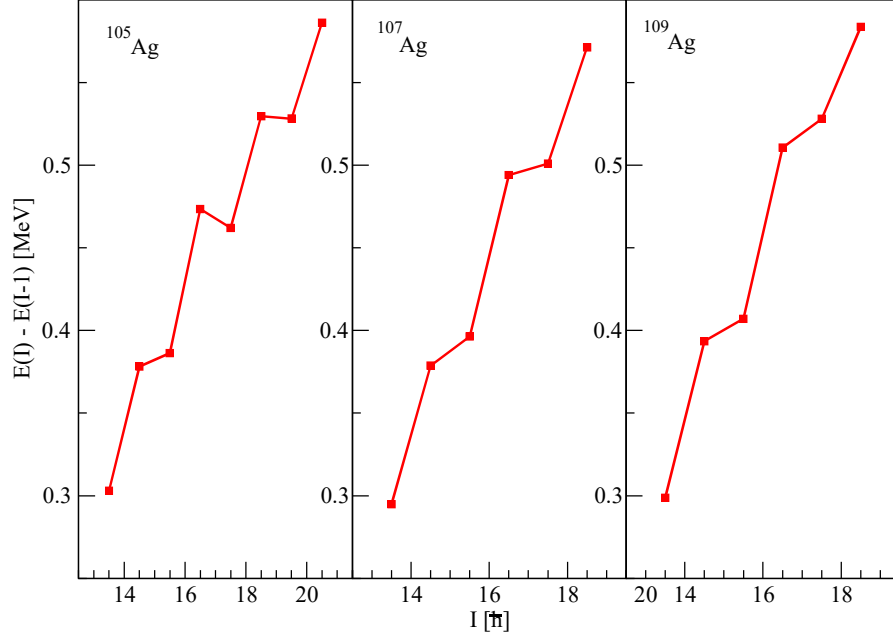In this context, the positive parity yrast cascades of $^{105,\,107,\,109}$Ag nuclei have

Figure 6.2: $E(I) - E(I-1)$ as a function of spin for the staircase bands of $^{105,\,107,\,109}$Ag nuclei.

been studied. In these odd mass Ag isotopes, the high spin levels above $I = 21/2\hbar$ (shown in Fig. 6.1) are generated from the $\pi g_{9/2}^{-1} \otimes \nu h_{11/2}^2$ configuration. The experimental routhians for these 3-qp bands have been plotted in Fig. 6.2. It is found that the high spin behaviours of the three bands are similar and have a unique structure. The $M1$ transition energies remain nearly constant among two neighboring levels while for the next pair they exhibit an abrupt jump and this behaviour continues. Thus, these bands exhibit a staircase like structure. This behaviour does not match with the conventional observations of increase or staggering in the $M1$ energies as a function of angular momentum. In addition, the measured $B(M1)$ rates in ^{107}Ag [81] and ^{109}Ag [14] show a distinct falling trend with increasing spin. This indicates the involvement of shears mechanism but the $M1$ transition

energies do not increase smoothly with spin.

In this thesis work, the level lifetime of the 3-qp band in ^{105}Ag have been measured and a model calculation has been performed to understand the observed behaviour of these 'staircase' bands.

6.2   Experiment and analysis

The high-spin states of ^{105}Ag were populated through the $^{96}Zr(^{14}N,5n)$ reaction using a 68 MeV ^{14}N beam from the 14-UD Pelletron at Tata Institute of Fundamental Research (TIFR). The experimental details is given in Chap.4. The relative intensity measurement was carried out for the positive parity band, which agreed within the 2σ value reported by J. Tima'r et $al.$ [82].

The linehshape analysis was carried out to measure the level lifetimes of the staircase band. The lineshape fitting procedure have been discussed in the Chap.3 of this thesis. In this band, the lifetime of $I^\pi = 39/2^+$ level was measured by fitting the lineshape of 1058 ($39/2^+ \rightarrow 35/2^+$) transition. A 100% side-feed was assumed for this level and the lifetime of this level was considered as effective. Lower level lifetimes were estimated by using the cascade fit method. Lineshapes were calculated from the 249 ($25/2^+ \rightarrow 23/2^+$) keV gated spectra at 40^0, 90^0 and 157^0 angles. The 90^0 angle was included in the fit to identify the contaminant peaks, if any. The lineshapes at these angles were fitted simultaneously using the lineshape code [68]. To measure lifetime of the $37/2^+$ level, the composite lineshape of 528 ($39/2^+ \rightarrow 37/2^+$) keV and 530 ($37/2^+ \rightarrow 35/2^+$) keV transitions were fitted together. In this fit, the transition quadrupole moment of the 528 ($39/2^+ \rightarrow 37/2^+$)
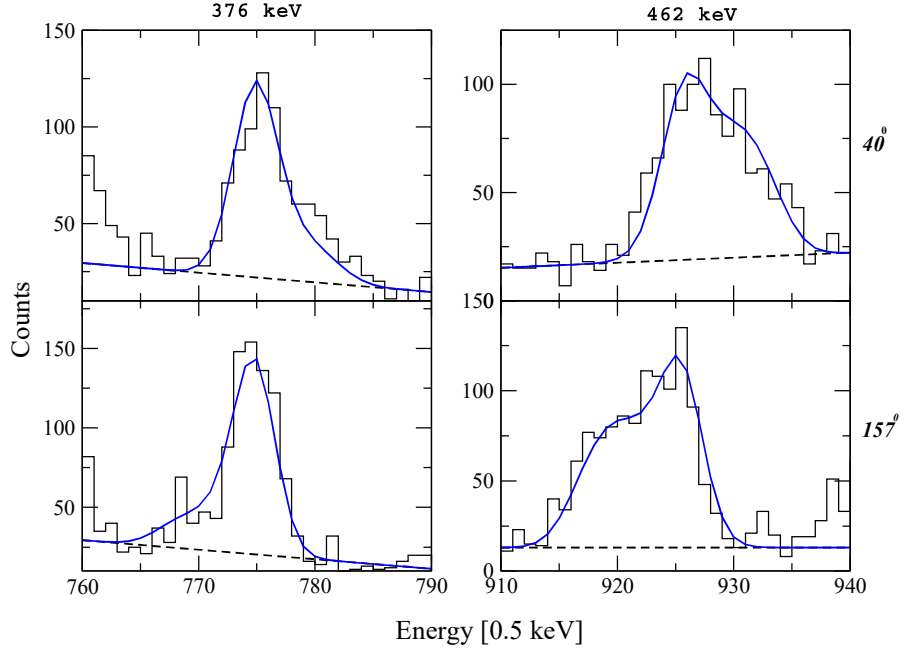
Figure 6.3: Example of lineshape fits for 376 ($29/2^+ \rightarrow 27/2^+$) keV, 462 ($35/2^+ \rightarrow$ $33/2^+$) keV transitions of ^{105}Ag.

keV transition was estimated from the effective lifetime of the $39/2^+$ level, and was kept fixed during the fit. To estimate lower level lifetimes, the $M1$ transitions were included one by one in the cascade and a global fit was performed. Apart from this, the two $E2$ cascades were fitted separately. The results from the separate fits of $E2$ and $M1$ transitions matches within the 3σ error bar and thus, increases the confidence level of the present analysis. The examples of the lineshape fits are shown in Fig. 6.3 and the measured lifetimes are given in Tab. 6.1.

6.3   Discussion

The behaviour of the observed transition rates in $^{105,\ 107,\ 109}$Ag seems to indicate that the high spin states in the 3-qp bands also originate due to the shears mechanism. During the course of this thesis work, the SPAC model has been successfully employed to describe the observed features of the non-yrast bands of ^{106}Ag [Chap. 4] and ^{110}Ag [Chap. 5]. Thus, it is natural to employ

Spin [$\hbar$]	Lifetime [ps]	Br. Ratio [B_r]	B(M1) [μ_N^2]	B(E2) [e^2b^2]
$31/2^-$	0.27 (03)	0.86 (05)	3.15 (52)	0.16(02)
$33/2^-$	0.20 (04)	0.78 (06)	2.08 (45)	0.19(04)
$35/2^-$	0.23 (05)	0.72 (05)	1.80 (40)	0.14(07)
$37/2^-$	0.20 (04)	0.80 (06)	1.56 (30)	0.09(02)
$39/2^-$	0.25	0.78 (06)	1.22	0.05

Table 6.1: The measured lifetimes , M1 Branching Ratios, the corresponding B(M1) and B(E2) values for the staircase band of ^{105}Ag.

the SPAC calculations to explore the 3-qp bands with the same parameter set, namely $\mathfrak{J} = 8.6\ \hbar^2$/MeV and $V_2 = 1.5$ MeV as for ^{106}Ag. For the $g_{9/2}^{-1} \otimes h_{11/2}^2$ configuration, the $j_\parallel = 4.5\hbar$ and the $j_\perp = 10.0\hbar$ is used. Thus, a maximum spin of $29/2\hbar$ can be generated by the shears mechanism while the band has been observed to extend up to $41/2\hbar$ for ^{105}Ag. This justifies the use of SPAC model.

The results of the SPAC calculations are shown in Fig. 6.4. It may be observed that, the average routhian (Fig. 6.4(a)) and the $B(M1)$ rates (Fig. 6.4(c)) can be described by the calculated values. However, the calculated $M1$ transition energies (Fig. 6.4(b)) show a smooth increase with increasing spin and the staircase structure can not be reproduced by these calculations. In order to
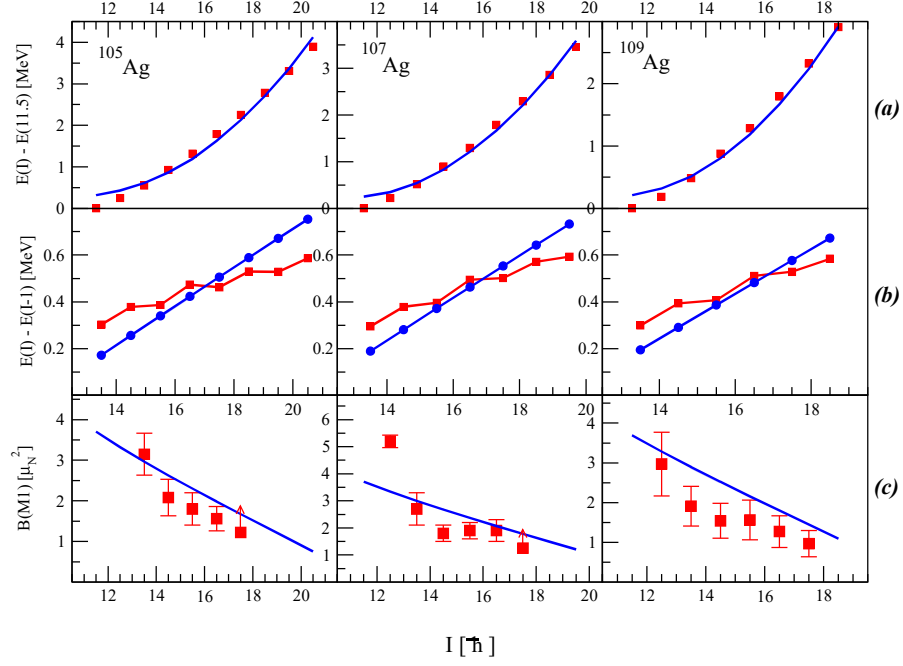
Figure 6.4: The measured and calculated (a) routhian, $E(I) - E(11.5)$, (b) $E(I) - E(I-1)$ and the (c) $B(M1)$ rates for the staircase bands of $^{105,\,107,\,109}$Ag. The theoretical values are estimated from the standard calculations of SPAC.

gain further insight of the staircase structure, the $[E(I) - E(I-1)]/2I$ has been plotted as a function of angular momentum in Fig. 6.5. This plot shows a clear staggering, which might be linked to the signature quantum number. The favoured signature for a single particle configuration is defined by

$$\alpha_f = \frac{1}{2} \sum_i (-1)^{j_i - \frac{1}{2}} \qquad (6.1)$$

Thus, for the $\pi g_{9/2}^{-1} \otimes h_{11/2}^2$ configuration, the favoured signature is $-\frac{1}{2}$ and the observed staggering of Fig. 6.5 supports this fact. It may be noted that, the two rotation aligned neutrons occupies the low-Ω orbitals of the $h_{11/2}$, which can induce the observed signature staggering.
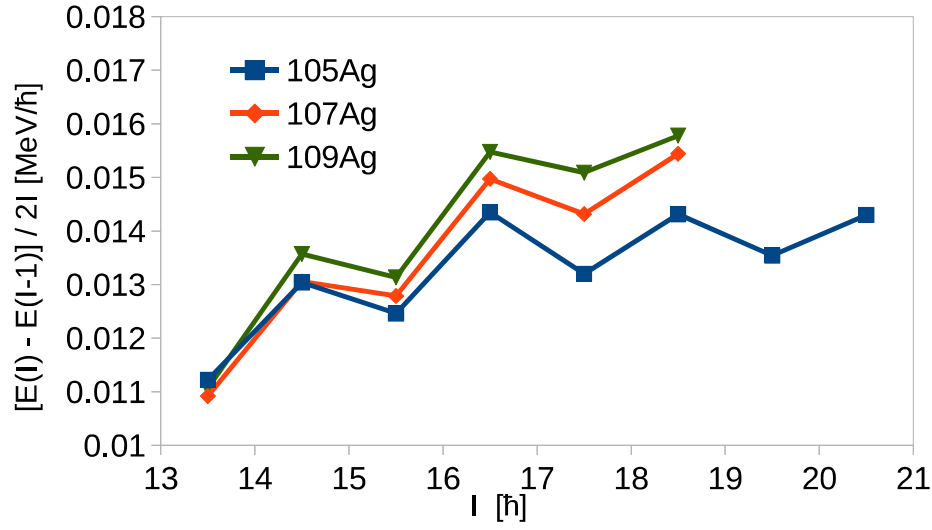
Figure 6.5: The $\big(E(I) - E(I-1)\big)/2I$ plot as a function of spin for the staircase bands.

This observation motivated the inclusion of a decoupling term [25] in the standard SPAC hamiltonian, i.e.

$$H = \frac{1}{2\mathfrak{J}} \left| \vec{I} - \vec{j}_{\parallel} - \vec{j}_{\perp} \right|^2 + V_2 P_2(\theta) + \frac{1}{2\mathfrak{J}}[a(-1)^{I+1/2}(I+1/2)] \qquad (6.2)$$

The calculated routhian with the modified hamiltonian is shown in Fig. 6.6 for $a = -0.02$, while the values of other parameters of SPAC have been kept fixed. Thus, an inclusion of a decoupling term can generate a staircase like band structure which closely resembles the experimental observations. However, the presence of a decoupling term will also affect the $M1$ transition rates. This has been accounted by noting the energy difference $(\Delta e')$ between the single particle routhians of the two signature partners (Fig. 6.7). The signature dependence of the $B(M1)$ values can be estimated using the
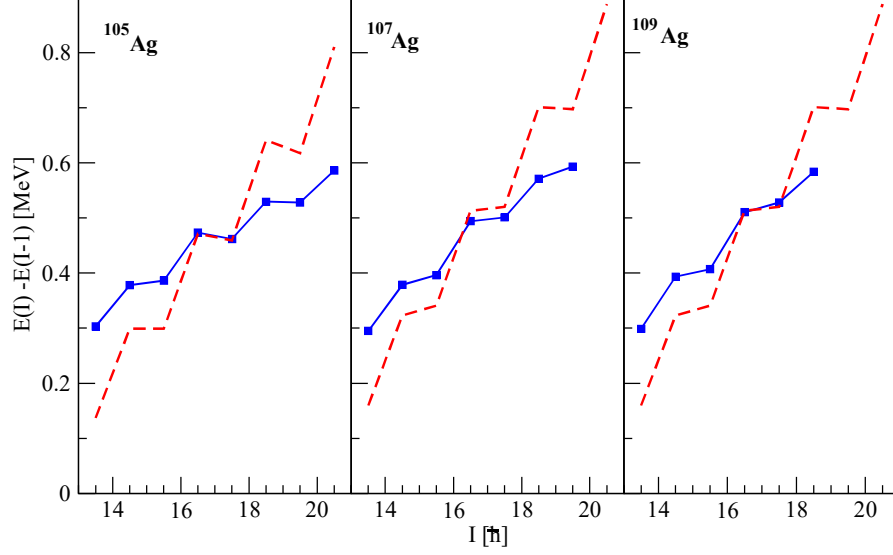
Figure 6.6: The measured and calculated values of $E(I) - E(I-1)$ as a function of I for the staircase bands. Values obtained from model calculations are given as dashed lines.

formula [83]

$$B(M1) = B(M1)_{\text{SPAC}} * \left(1 - \frac{\Delta e'}{\omega}\right)^2 \qquad (6.3)$$

where, the $B(M1)$ values of higher energy sequence is multiplied with the factor of $\left(1 - \frac{\Delta e'}{\omega}\right)^2$. These calculated $B(M1)$ values are plotted in Fig. 6.8. It may be noted that, the new values show a small signature dependence due to the small value of $\Delta e'$. The present uncertainties on the level lifetime measurements are too large to distinguish this small change.
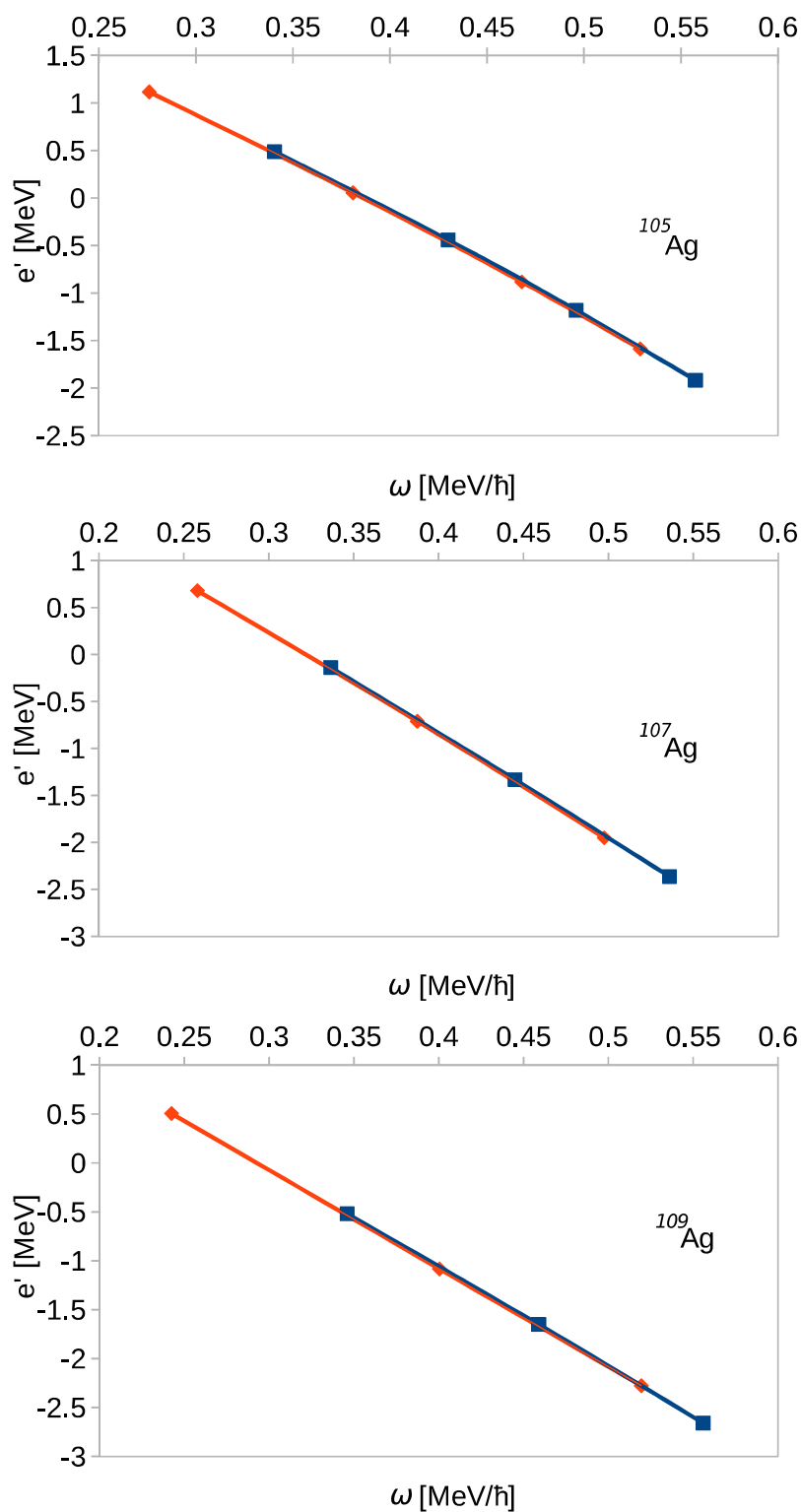
Figure 6.7: The experimental routhians for the staircase bands.
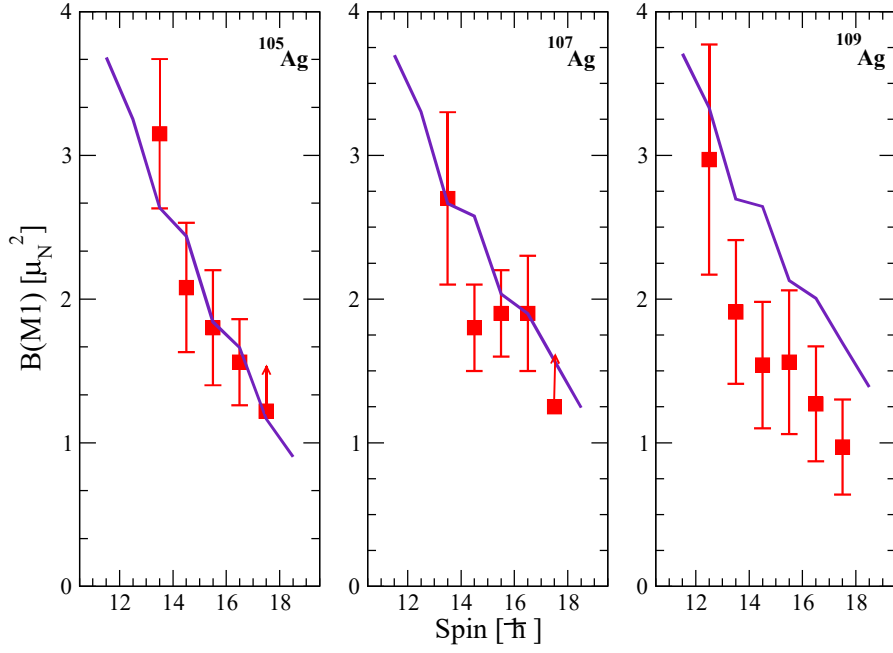
Figure 6.8: The measured and calculated $B(M1)$ rates for the staircase bands. The calculated values are plotted as solid line.

6.4   Summary

The staircase structure in the +ve parity bands of the odd Ag isotopes can be described by the inclusion of a decoupling term in the SPAC hamiltonian. Apart from the Ag isotopes, similar kind of band structures are also observed in the Rh and In isotopes [81]. This new framework may be employed to study these isotopes.

7

Summary

The primary objective of this thesis work was to explore the angular momentum generation mechanisms by studying the high-spin states in the Ag isotopes of mass ~ 100 region. The basic requirement of high-spin spectroscopy, is to impart a large angular momentum in the nuclei and the methods of which have been discussed in Chap.3. Thereafter, we study the nuclear decay through γ emission to its ground state. These γ-decays can be grouped in two catagories based on their origin - the statistical and the discrete γ rays. The nuclear levels in the statistical region are populated just after the energy of the nucleus falls below its particle emission threshold. At this stage, the nucleons inside the nucleus arrange themselves to increase their pairing correlations, thus, levels at this region are of single particle in nature. In the statistical region, the nucleus mostly loses its energy rather than losing angular momenta, as a result statistical $E1$ transitions are emitted. These gamma rays form a continuum spectrum due to very high density of lev-

els. Once the nucleus is cold enough, the increase in correlation effect can be observed from the ordering of the levels. This ordering leads to a much less density of the levels [26]. In this region, the sequence of levels with the lowest energy for a given spin form the 'yrast band'. The levels other than these are categorized as non-yrast. It is to be noted that, all the non-yrast excited levels end up by decaying to the yrast levels. As a result, the levels in the yrast-band have the highest intensity for a given spin. Thus, the yrast-bands are most suitable to study through the discrete γ-spectroscopy. On the other hand, the γ-spectroscopic studies for the non-yrast bands need substantial volume of data and thus, requires large γ-arrays. In this regard, the INGA array [57, 58], has been suitable for the present work where the non-yrast bands of ^{106,110}Ag were studied. In addition, I have also studied the systematics of the yrast band in $^{105,\ 107,\ 109}$Ag.

The study of both the yrast and the non-yrast levels in nuclei have their specific physics interests. The single particle configurations for the yrast bands are dominated by the levels near the Fermi surface. Thus, different angular momentum generation mechanisms can be attributed through the systematic study of the yrast bands. The phenomena of deformed nuclear rotation was established from the observed yrast band structures in the nuclei of mass regions $150 < A < 190$ and $A > 220$ [24]. Similarly, the phenomena of 'Magnetic Rotation' and 'Anti-Magnetic Rotation' were observed in the yrast band structures of Pb nuclei [30] and Cd nuclei [46], respectively. On the other hand, the non-yrast bands originate due to varied single particle configurations and exotic modes of excitations may be identified. The examples of such occurrences are the 'Wobbling Mode' of excitation [28], the

'Spin Chirality ' [29], the phenomena of 'Shape Co-existence ' [38] etc.

In the present work, the level-scheme of ^{106}Ag was extended by establishing the negative and the positive parity non-yrast bands. The high spin transition rates were calculated for both the bands using the measured lifetime from DSAM. Both the bands exhibit a falling nature in the $B(M1)$ and $B(E2)$ rates with spin as shown in Fig. 7.1. Thus, as a first choice, the shears
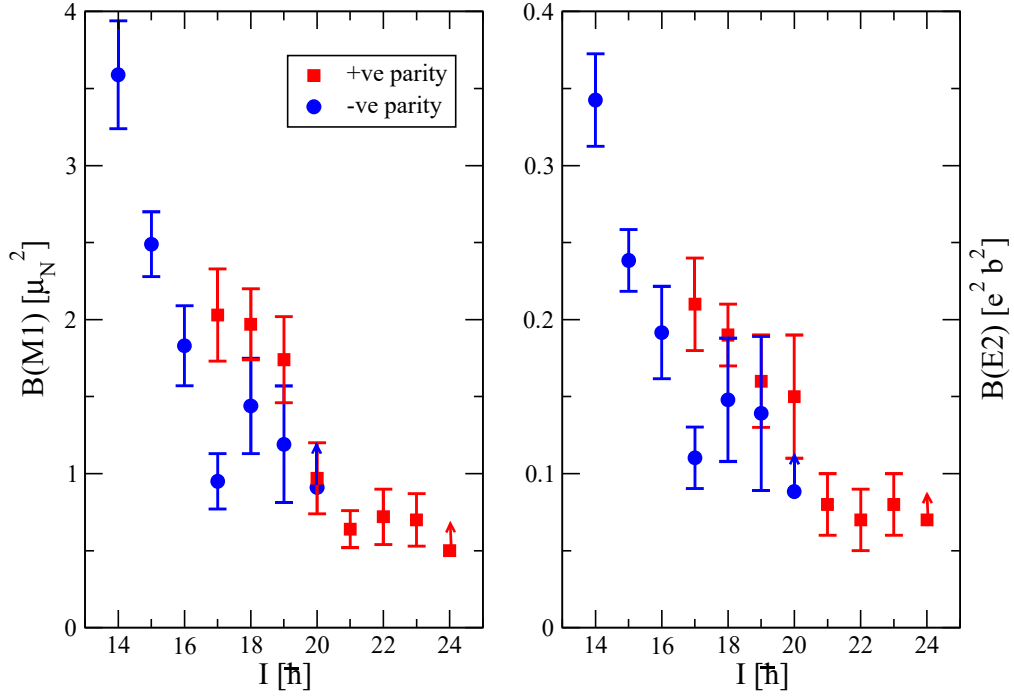
Figure 7.1: The $B(M1)$ and the $B(E2)$ rates for the non-yrast positive and negative parity bands of ^{106}Ag.

mechanism [32] was considered to generate the high-spin states based on the single particle configurations $\pi g_{9/2}^{-3} \otimes \nu h_{11/2}$ and $\pi g_{9/2}^{-1} \otimes \nu[(d_{5/2}/g_{7/2})h_{11/2}^2]$ for the negative and the positive parity bands, respectively. In these non-yrast bands, the principal axis rotation was found to co-exist with the shears

mechanism to generate the high spin states. In addition, the shears structure in this nucleus led to interesting observations. The shears mechanism in the negative parity band was found to arise from a $\pi g_{9/2}^{-3} \otimes \nu h_{11/2}$ configuration and this three proton hole structure was observed for the first time in the Ag nucleus [7]. A shears band-crossing was also found in this band, after the neutron alignment in the $(d_{5/2}/g_{7/2})$ orbitals at a spin of $I = 17\hbar$. On the other hand, no band-crossing was observed in the positive parity band, as the AB-crossing is blocked. Thus, to generate the high spin states in this band after the shears mechanism was exhausted, the nucleus exhibit a non-collective rotation. As a result, the falling trend of the transition rate becomes nearly constant beyond the spin of $I = 21\hbar$. Thus, a clear termination of the shears mechanism was observed for the first time in the positive parity non-yrast band of ^{106}Ag [10].

The non-yrast positive parity band of ^{110}Ag was found to originate due to the shears mechanism with the particle-hole configuration of $\pi g_{9/2}^{-1} \otimes \nu[(d_{5/2}/g_{7/2})h_{11/2}^2]$. The positive parity band of ^{106}Ag also has the same configuration. Thus, the transition rates were found to be similar in the two cases (Fig. 7.2). However, the positive parity band of ^{110}Ag could be established up to $I = 18\hbar$ and thus the saturation effect of the transition rates observed in the ^{106}Ag (beyond $I = 20\hbar$) was not found.

The negative parity non-yrast band of ^{110}Ag is a partner of the yrast band. The partner band in ^{106}Ag was found to originate due to the different shapes arising from a broad TRS minimum [69]. The partner band in ^{108}Ag, on the other hand, originated due to two different quasiparticle configurations [51]. This was evident from the fact that the yrast band is a 2-qp band up to
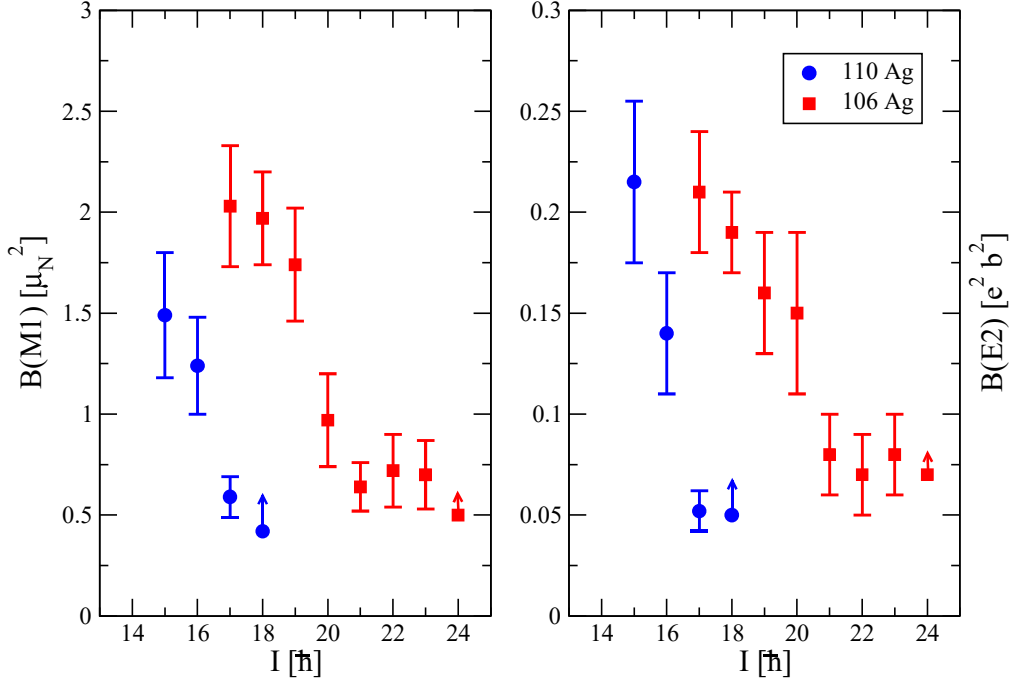
Figure 7.2: The $B(M1)$ and the $B(E2)$ rates for the positive parity bands of ^{106}Ag and ^{110}Ag.

$I \sim 15\hbar$ while the partner band originates due to a 4-qp structure with a band head at $I = 10\hbar$. However, the observed features of the doublet band could be well described by triaxial projected shell model (TPSM) calculation [38]. This indicated that ^{108}Ag might be a triaxial nucleus. It was only for the heavier ^{110}Ag that the triaxiality could be confirmed through the observation of a signature splitting [12].

The routhians for the partner bands of ^{106}Ag cross each other around $I \sim 15\hbar$, thereby indicating a weak interaction. In ^{110}Ag, however, the 4-qp partner band shows a strong interaction and the separation energy decreases with increasing spin and at $I = 19\hbar$ the value is 100 keV. The routhians of

$^{106,\ 108,\ 110}$Ag have been shown in Fig. 7.3 (a). In addition, the magnitude and phase of the $B(M1)/B(E2)$ staggering is similar for the partner bands (Fig. 7.3 (b)). These observations seem to indicate that the 4-qp partner bands of ^{110}Ag (for $I > 15\hbar$) arise due to weak chiral symmetry breaking and there is an indication of the strong symmetry breaking beyond $I = 19\hbar$.
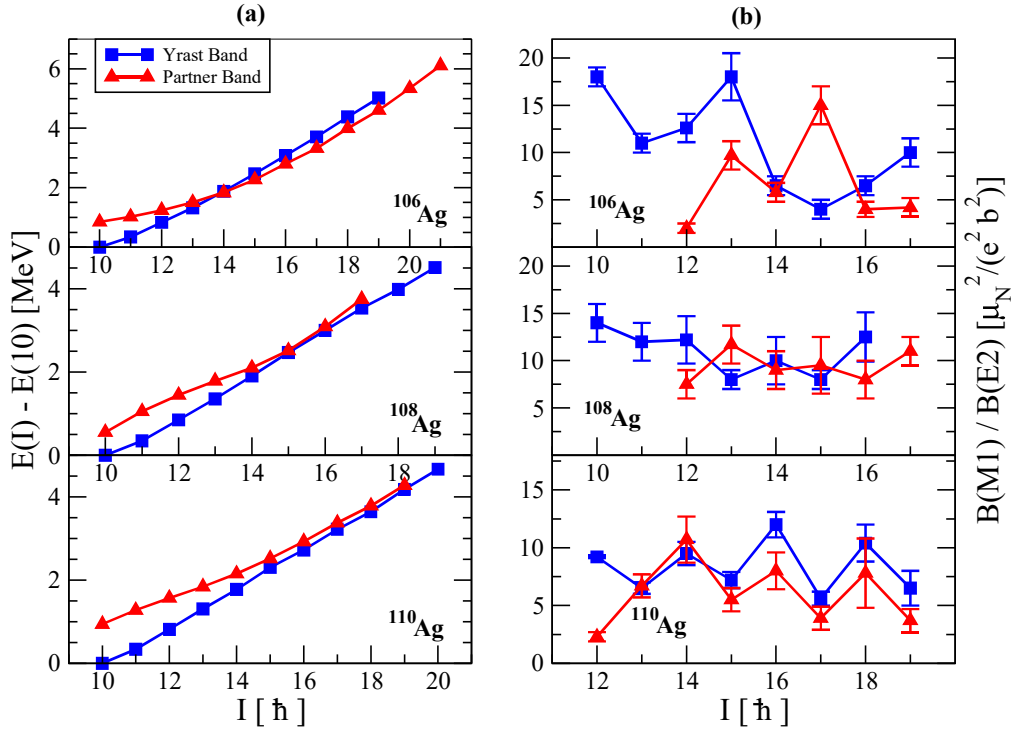

Figure 7.3: The experimental (a) routhians and (b) the $B(M1)/B(E2)$ values for the partner bands observed in $^{106,\ 108,\ 110}$Ag.

In a separate study of the yrast band systematics, the bands of $^{105,\ 107,\ 109}$Ag have been explored. The novel band structure, named as the 'staircase band', seems to generate due to the shears mechanism built on decoupled band. This

observation is based on the fact that the staircase structure can be reproduced by the inclusion of a decoupling term in the SPAC hamiltonian.

Future Directions

In the present thesis, a number of angular momentum generation mechanisms in Ag isotopes have been studied where the basic process is the shears mechanism. This happens due to our choice to study the neutron rich Ag isotopes. The diversity of the observed phenomena is due to the co-existence of collective rotation and the shears mechanism. This largely happens as the shears blades in this mass region are much small compared to those of $A \sim 200$ region and the nuclei are moderately deformed. Thus, while the high spin bands in the $A \sim 200$ region can be generated entirely by the shears mechanism, the shears bands of $A \sim 100$ region have $\sim 30\%$ rotational contribution. Thus, it might be interesting to extend similar studies to $A \sim 80$ region where the shears structure is formed by the $g_{9/2}$ proton particle and the $g_{9/2}$ neutron holes. In these cases, a stronger interplay between collective rotation and shears mechanism is expected and a number of exotic nuclear behaviour may be observed. Very recently, octupole correlations between multiple chiral bands have been observed in ^{78}Br [84]. However, to establish such exotic modes, the transition rates of the high spin states of these bands have to be measured. The importance of this knowledge has been established during the course of the present thesis.

151

Bibliography

[1] Joachim Alexander Maruhn, Paul-Gerhard Reinhard and Eric Suraud, *Simple Models of Many-Fermion Systems* (Springer, 2012).

[2] M. G. Mayer and J. H. D. Jensen, *Elementary Theory of Nuclear Shell Structure* (Wiley, New York, 1955).

[3] M. J. Wright *et al.*, Phys. Rev. Lett. **99**, 150403 (2007).

[4] Ch. Sikorski and U. Merkt, Phys. Rev. Lett. **62**, 2164 (1989); T. Demel, D. Heitmann, P. Grambow and K. Ploog, Phys. Rev. Lett. **64**, 788 (1990).

[5] R. M. Diamond and F. S. Stephens, Ann. Rev. Nucl. Part. Sci. **30**, 85 (1980).

[6] E. O. Lieder *et al.*, Phys. Rev. Lett. **112**, 202502 (2014).

[7] B.Das *et al.*, Phys. Rev. C **93**, 064322 (2016).

[8] R. M. Clark and A. O. Macchiavelli, Annu. Rev. Nucl. Part. Sci. **50**, 1 (2000).

[9] E.O. Podsvirova *et al.*, Eur. Phys. J. A **21**, 1 (2004); A.A. Pasternak *et al.*, Eur. Phys. J. A **23**, 191 (2005); **37**, 279 (2008); A.A. Pasternak, E.O. Lieder, R.M. Lieder, Acta Phys. Pol. B **40**, 647 (2009); S. Rajbanshi *et al.*, Phy. Rev. C **89**, 014315 (2014).

[10] B.Das *et al.*, Phys. Rev. C **95**, 051301(R) (2017).

[11] B.Das *et al.*, Proceedings of the DAE-BRNS Symp. on Nucl. Phys. **61**, 102 (2016).

[12] S. Roy *et al.*, Phys. Lett. B **710**, 587 (2012).

[13] B.Das *et al.*, Phys. Rev. C **98**, 014326 (2018).

[14] P. Datta *et al.*, Phys. Rev. C**78**, 021306(R) (2008).

[15] S. H. Yao *et al.*, Phy. Rev. C **89**, 014327 (2014).

[16] B.Das *et al.*, Proceedings of the DAE-BRNS Symp. on Nucl. Phys. **60**, 82 (2015).

[17] F. Halzen and A. D. Martin, *Quarks and leptons: An introductory course in modern particle physics* (Wiley, New York, 1884).

[18] R. F. Casten, *Nuclear Structure from a Simple Perspective* (Oxford, New York, 2005).

[19] J. J. Sakurai, *Modern Quantum Mechanics* (Pearson, India, 2012).

[20] K. S. Krane, *Introductory Nuclear Physics* (Wiley, India, 2012).

[21] S. N. Ghosal, *Nuclear Physics* (S. Chand, India, 1997).

[22] L. D. Landau and Ya. Smorodinsky, *Lectures on Nuclear Theory* (Dover, New York, 1993).

[23] A. Bohr and B. R. Mottelson, *Nuclear Structure*, Vol. 2 (Benjamin, New York, 1969).

[24] P. Ring and P.Schuck, *The Nuclear Many-Body Problem* (Springer, Berlin, 2004).

[25] M. K. Pal, *Theory of Nuclear Structure* (EWP, New Delhi, 2009).

[26] Michel Baranger and Erich Vogt, *Advances in Nuclear Physics*, Vol. 10 (Springer Science+ Business Media, LLC, 1968).

[27] M. J. A de Voigt, J. Dudek, Z. Szyman′ski, Rev. Mod. Phys. **55**, 949 (1983).

[28] S. C. Pancholi, *Exotic Nuclear Excitations* (Springer, 2010).

[29] V. I. Dimitrov, S. Frauendorf and F. Dönau, Phys. Rev. Lett. **84**, 5732 (2000).

[30] G. Baldsiefen et al., Phys. Lett. B **275**, 252 (1992); A. Kuhnert et al., Phys. Rev. C **46**, 133 (1992); R. M. Clark et al., Phys. Lett. B **440**, 251 (1998).

[31] H. Hübel *et al.*, Progress in Particle and Nuclear Physics **54**, 1 (2005).

[32] R. M. Clark and A. O. Macchiavelli., Annu. Rev. Nucl. Part. Sci. **50**, 1 (2000).

[33] A.O. Macchiavelli *et al.*, Phys. Lett. B **450**, 1 (1999).

[34] Stefan Frauendorf., Rev. Mod. Phy. **73**, 463 (2001).

[35] Sven Gösta Nilsson, Dan. Mat. Fys. Medd. **29**, 16 (1955).

[36] A.Bohr and B. Mottelson, Dan . Mat . Fys . Medd . **30**, 1 (1955).

[37] W.A. Dar *et al.*, Nucl. Phys. A. **933**, 123 (2015).

[38] R. Palit, G.H. Bhat and J.A. Sheikh., Eur. Phys. J. A. **53**, 90 (2017).

[39] S. Chmel *et al.*, Phys. Rev. Lett. **79**, 2002 (1997).

[40] S . Frauendorf, Nucl. Phys. A **557**, 259 (1993).

[41] A. O. Macchiavelli *et al*, Phys. Rev. C **57**, 1073(R) (1998).

[42] P. Van Isacker and A. O. Macchiavelli, Phys. Rev. C **87**, 061301(R) (2013).

[43] R. M. Clark *et al.*, Phys. Rev. Lett. **82**, 3220 (1999).

[44] A. J. Simons *et al.*, Phys. Rev. Lett. **91**, 162501 (2003).

[45] P. Datta *et al.*, Phys. Rev. C **71**, 041305(R) (2005).

[46] Santosh Roy *et al.*, Phys. Lett. B **694**, 322 (2011); Santosh Roy and S. Chattopadhyay, Phy. Rev. C **83**, 024305 (2011).

[47] T. Koike, K. Starosta and I. Hamamoto, Phys. Rev. Lett. **93**, 172502 (2004).

[48] E. Grodner *et al.*, Phys. Lett. B. **703**, 46 (2011).

[49] Amita, A. K. Jain, and B. Singh, At. Data Nucl. Data Tables **74**, 283 (2000).

[50] M. Sugawara *et al.*, Phys. Rev. C **86**, 034326.

[51] J. Sethi *et al.*, Phys. Lett. B **725**, 85 (2013).

[52] J. Tima′r *et al.*, Phys. Lett. B **598**, 178 (2004).

[53] P. Joshi *et al.*, Phys. Lett. B **595**, 135 (2004).

[54] Paddy Regan, *Post Graduate Nuclear Experimental Techniques (4NET) Course Notes* (University of Surrey, UK, 2003).

[55] Jagdish Varma, *Nuclear Physics Experiments* (New Age International (P) Ltd., 2001).

[56] F. A. Beck *et al.*, *The Clover Detector.*

[57] S. Muralithar *et al.*, Nucl. Instrum. Methods Phys. Res. Sect. A **622**, 281 (2010).

[58] R. Palit *et al.*, Journal of Physics: Conference Series **420**, 012159 (2013).

[59] R. Palit *et al.*, Nucl. Instrum. Methods Phys. Res. Sect. A **680**, 90 (2012).

[60] R. K. Bhowmik, A. K. Jain and D. C. Biswas, Proceedings of the DAE Symposium on Nuclear Physics **44B**, 422 (2001).

[61] S. Das *et al.*, Proceedings of the DAE Symposium on Nuclear Physics **62**, 1066 (2017).

[62] Filippo Cappellaro, Joa Ljungvall and Johan Nyberg, *Laboratory exercise in nuclear physics* (Spring, 2012).

[63] D. C. Radford, Nucl. Instrum. Methods Phys. Res. Sect. A **361**, 297 (1995).

[64] K. S. Krane, R. M. Steffen and R. M. Wheeler, Nucl. Dat. Tabl. **11**, 351 (1973).

[65] E. S. Paul, *Angular Correlation Manual: Version 1.0* (September, 1995).

[66] K. Starosta *et al.*, Nucl. Instr. and Meth. in Phys. Res. A **423**, 16 (1999).

[67] F. James and M. Roos, Comput. Phys. Commun. **10**, 343 (1975).

[68] J. C. Wells and N. R. Johnson, Oak Ridge National Laboratory Report No. ORNL-6689, 1991 (unpublished).

[69] P. Joshi *et al.*, Phys. Rev. Lett. **98**, 102501 (2007).

[70] N. Rather et al., Phys. Rev. Lett. **112**, 202503 (2014).

[71] Dan Jerrestam *et al.*, Nucl. Phys. A **577**, 786 (1994).

[72] C. Y. He *et al.*, Phys. Rev. C **81**, 057301 (2010).

[73] A. Y. Deo *et al.*, Phys. Rev. C **73**, 034313 (2006).

[74] Santosh Roy *et al.*, Phy. Rev. C **81**, 054311 (2010)

[75] P. Datta *et al.*, Phys. Rev. C **69**, 044317 (2004).

[76] A. Krämer-Flecken *et al.*, Nucl. Instr. and Meth. in Phys. Res. A **275**, 333 (1989).

[77] G. Gürdal and F.G. Kondev, Nuclear Data Sheets **113**, 1315 (2012).

[78] M.-G. Porquet *et al.*, Eur. Phys. J. A **15**, 463 (2002).

[79] HAO Xin *et al.*, Chin. Phys. C. **32**, 143 (2008).

[80] I. Hamamoto, Phys. Lett. B **235**, 221 (1990).

[81] S. H. Yao *et al.*, Phys. Rev. C **89**, 014327 (2014).

[82] J. Tima′r *et al.*, Phys. Rev. C **76**, 024307 (2007).

[83] S. Chattopadhyay *et al.*, Phys. Rev. C **47**, 1(R) (1993).

[84] C. Liu *et al.*, Phys. Rev. Lett. **116**, 112501 (2016).